MONTE CARLO SIMULATION OF AEROSOL DYNAMICS IN TURBULENT FLOWS

LIU HONGMEI

PhD

The Hong Kong Polytechnic University

2019

The Hong Kong Polytechnic University

Department of Mechanical Engineering

MONTE CARLO SIMULATION OF AEROSOL DYNAMICS IN TURBULENT FLOWS

LIU HONGMEI

A thesis submitted in partial fulfillment of the requirements
for the Degree of Doctor of Philosophy

June 2018

Certificate of Originality

I hereby declare that this thesis is my own work and that, to the best of my knowledge and belief, it reproduces no material previously published or written, nor material that has been accepted for the award of any other degree or diploma, except where due acknowledgement has been made in the text.

_____ (Signed)

LIU Hongmei (Name of student)

Abstract

The study of aerosol dynamics is of great importance to a variety of scientific and engineering fields including atmospheric science, air pollution control, industrial production, and combustion and chemical engineering sciences. A new differentially weighted operator splitting Monte Carlo (DWOSMC) method is first proposed and developed in the present study in which weighted simulated particles and operator splitting technique are coupled to improve the computational accuracy and efficiency of traditional Monte Carlo methods in simulating complex aerosol dynamics.

This newly proposed and developed DWOSMC method is first verified in one-component aerosol systems by comparing its numerical simulation results with the corresponding analytical solutions for several typical cases and the sectional method for some complex cases in excellent agreement. The numerical simulation results demonstrate that this DWOSMC method has high computational efficiency and accuracy in solving complex aerosol dynamic problems where nucleation, coagulation and condensation processes simultaneously take place.

This DWOSMC method is further extended to simulate multi-component aerosol systems. The results obtained from DWOSMC method are compared with a sectional method for various regimes of simultaneous coagulation and condensation processes in two-component aerosol systems. It is proved that this DWOSMC method is more computationally efficient than the sectional method in simulating

two-component aerosol systems. Furthermore, the DWOSMC method is able to predict the particle number density, total particle volume, particle number distribution and component-related particle volume density distributions as well as the bivariate compositional distribution.

In order to solve multi-dimensional aerosol dynamics interacting with fluid phase, the Monte Carlo method for describing particle dynamics is coupled with computational fluid dynamics (CFD) under the Eulerian-Lagrangian reference frame. The formulated CFD-Monte Carlo method is firstly used to simulate a spatially inhomogeneous particle-laden turbulent flow. The effects of two-way coupling, turbulent dispersion model and Reynolds number based on a square rod obstacle on the particle dispersion pattern are fully studied for a wide range of particle Stokes number.

Finally, the formulated CFD-Monte Carlo method is used to study aerosol dynamics in turbulent flows. The DWOSMC method is coupled with large eddy simulation (LES) to examine the evolution and growth of aerosol particles in a turbulent planar jet. Firstly, the newly developed LES-DWOSMC method is verified by the results obtained from a direct numerical simulation-sectional method (DNS-SM) for coagulation occurring in a turbulent planar jet from available literature. The fluid velocity field and the time-averaged particle diameter distribution obtained from LES-DWOSMC show good agreement with those obtained from DNS-SM. The coherent vortex structures of fluid gas have a significant impact on the aerosol particle dispersion patterns. Then the effects of jet

temperature and jet Reynolds number on the evolution of time-averaged mean particle diameter, normalized particle number concentration and particle size distribution (PSD) are fully investigated. The jet temperature and jet Reynolds number prove to be two important parameters that can be used to control the evolution and pattern of PSD in aerosol reactors. This developed LES-DWOSMC method proves to be able to predict and render a better understanding of the evolution and growth of the particle size distribution (PSD) of the aerosols in turbulent flow.

In summary, this newly proposed and developed CFD-DWOSMC method in the present study has demonstrated high capability in the numerical simulation of complex aerosol dynamics in turbulent flows.

Acknowledgements

First, I would like to express my sincerest gratitude and respect to my Supervisor, Prof. Tat Leung Chan for his comprehensive support, encouragement, inspiring guidance, understanding and patience throughout my study at the Department of Mechanical Engineering, The Hong Kong Polytechnic University (PolyU). I appreciate his extensive knowledge, joy and enthusiasm for academic research as well as his kind and generous support to me. I would like also to extend my thanks to Dr. Shuyuan Liu for his kind guidance and selfless help.

I am grateful to the Scientific Officer, Mr. Raymond Chan for his invaluable technical support. My appreciations also go to Ms. Lily Tam and Ms. Michelle Lai who provided kind administrative support during my study. I would also like to express my thanks for the research studentship granted by The Hong Kong Polytechnic University (PolyU) and Department of Mechanical Engineering for accomplishing this research work.

I am also grateful to Miss Jing Bian and Mr. Guangyuan Huang in my office, and other friends in Hong Kong for their friendship and help during my three-year study at PolyU.

Finally, I wish to give my deep thanks to my family members for their love, support, understanding and encouragement during my study at PolyU.

Table of Contents

List of Figures

List of Tables

Nomenclature

A, B	component symbol
A_0(t)	analytical value
A(t)	numerical simulation value
C	particle number concentration (#/m^3)
C_0	initial particle number concentration (#/m^3)
C_D	drag coefficient
C_{ij}	collision kernel
C_i	coagulation rate of simulated particle, i
d	particle diameter (m)
d_{ave}	average particle diameter (m)
d_p	particle diameter (m)
D	diffusion coefficient (m^2/s)
f_p	particle-to-fluid force (m/s^2)
f_s	forces applied to the solid phase except for drag force (m/s^2)
g_f	collision restitution coefficient
ΔG^*	Gibbs free energy (J)
h	obstacle height (m)
i,j	particle label
I	condensation kernel (m^3/s)
J	nucleation kernel (/s)
K	coagulation kernel (m^3/s)
k	turbulent energy (J)

k_B	boltzmann constant (J/K)
K_{n}	Knudsen number
l_i	the length of grid, i (m)
L	length (m)
m_i,m_j	particle mass (kg)
m_k	moments of particles
$\boldsymbol{m}_r$	momentum vector (kg·m/s)
M	prescribed number of Monte Carlo loops
M_2	the second moment
n	number density of aerosol particles
N	particle number concentration during the simulation interval
N_0	initial particle number concentration
N_c	particle number concentration
$N_{c,0}$	particle number concentration in the jet inlet
N_{p}	number of simulated particles
N_{r}	number of real particles
N_{s}	number of simulated particles
p	pressure (Pa)
P^{∞}	vapor pressure far from the particle
p^{eq}	the equilibrium vapor pressure
P_{col}	collision probability
P_{i}	probability of coagulation event taking place on particle, i
$q_{0,0}$	particle number distribution
$q_{1,0}$, $q_{0,1}$	component-related particle volume density distribution

r_1,r_2	random number
Re_h	Reynolds number based on the square obstacle, uh/v_a
Re_D	Reynolds number based on the jet diameter, U_1D/v_a
St	Stokes number, τ_P/τ_f
t	time (s)
t_s	sampling time (s)
t^*	normalized sampling time, t/t_s
T_j	the temperature of the jet
T_K	temperature (K)
Δt	time-step (s)
δt	time-step (s)
$\vec{u}$	velocity of the gas (m/s)
$\overline{U}$	average velocity of the fluid flow (m/s)
u'	fluctuating velocity of the fluid flow (m/s)
u_e	main flow velocity (m/s)
$\boldsymbol{u}_i$,$\boldsymbol{u}_j$	velocity vector (m/s)
u_p	velocity of dispersed particle (m/s)
u^*	friction velocity (m/s)
v	particle volume (m^3)
v_0	initial volume of particles (m^3)
V	total particle volume during the simulation interval (m^3)
V_0	initial total volume of the aerosol particles (m^3)
V_{cell}	the volume of the computational cell
w_i	weight of the simulated particle

x,y	coordinate or position
X	the total process
X_1, X_2	sub-processes
X_d	deterministic process
X_s	stochastic process

Greek Symbols

α	correction factor
ε	relative error
ρ	density (kg/m^3)
ρ_f	density of continuous gas flow (kg/m^3)
ρ_p	density of dispersed particle (kg/m^3)
τ_f	flow response time (s)
τ_{ij}	subgrid scale stress tensor
τ_p	particle relaxation time (s)
σ	standard deviation of the normal distribution
λ	a random number
ζ	correction factor
δ	boundary layer thickness (m)
μ_a	dynamic viscosity of air (kg/m·s)
v_a	kinematic viscosity of air (m^2/s)

φ_v	volume fraction
ϕ	an arbitrary scalar
ξ	particle volume density (m^3/m^3)

Abbreviations

CFD	computational fluid dynamics
CPU	central processing unit
DNS	direct numerical simulation
DQMOM	direct quadrature method of moments
DSMC	direct simulation Monte Carlo method
DWMC	differentially weighted Monte Carlo method
DWOSMC	differentially weighted operator splitting Monte Carlo method
DWTDMC	differentially weighted time-driven MC method
E-E	Eulerian-Eulerian
E-L	Eulerian-Lagrangian
GDE	general dynamics equation
LES	large eddy simulation
LPT	Lagrangian particle tracking
MC	Monte Carlo
MMC	multi-Monte Carlo method
MOM	method of moment
MOMIC	method of moments with interpolative closure
N-S	Navier–Stokes
OS	operator splitting
OSMC	operator splitting Monte Carlo method

PBE	population balance equation
PDF	probability density function
PN	particle number concentration
PSD	particle size distribution
QMOM	quadrature method of moments
RANS	Reynolds averaged Navier-Stokes equation
RUD	repeated upwind difference method
SGS	subgrid scale
SI	sequential iterative
SM	sectional method
SNI	sequential non-iterative
SOA	secondary organic aerosols
SWPM	stochastically weighted particle method
SWOSMC	stochastically weighted operator splitting Monte Carlo method
TEMOM	Taylor-series expansion method of moments
TGFEM	Taylor-Galerkin method
TVOC	total volatile organic compound
VOC	volatile organic compound

Chapter 1 Introduction

1.1 Research Background and Scope

Aerosols are very fine and ultrafine liquid or solid particles suspended in the gas. The size of the aerosol particles varies from several nanometers (nm) to micrometers (μm) (Lu, 2005). For example, the fog, smoke, soot and the solid dust in the air are all related to aerosols. Thus, the dynamic behavior of aerosols is of great importance in our life, as well as in many different fields including atmospheric sciences, air pollution and control, industrial production, combustion and chemical science, etc. (Flagan and Seinfeld, 1988; Friedlander, 2000; Huang et al., 2014; Rodrigues et al., 2018). Atmospheric aerosols cause plenty of air pollution problems, and consequently impose influence badly on our lives, including contributing directly to our adverse health, visibility reduction that will cause traffic jams or traveling problems, and global climate change. Also, the source of nano- and fine particles of pollutants are related to human's behaviors, i.e., the vehicle exhaust, biomass burning and industrial emission (Aubagnac-Karkar et al., 2018; Laskin et al., 2015; Liu et al., 2011).

In order to understand the properties of the aerosols, more and more attention has been drawn to the fundamental study of the formation and evolution of aerosols in recent years. Distributed aerosol properties of interest include the number, volume and mass concentration, chemical composition, light scattering; the processes involved in the aerosol dynamics include nucleation, collision, coagulation, agglomeration, gas-to-particle conversion, sedimentation, condensation growth, evaporation, breakage, and deposition, etc. (Davari and Mukherjee, 2018;

Huang et al., 2014; Marchisio and Fox, 2005; Zhao et al., 2018). The typical formation and growth processes of aerosol particles are shown in Figure 1.1 (Raman and Fox, 2016), which demonstrates the flame synthesis of nanoparticles, where the aerosol particles are generated from individual/clustered precursor molecules through gas-phase chemical reactions as well as surface growth reactions. The formed and nucleated particles will then experience further surface growth and oxidation reaction, and coagulation processes.

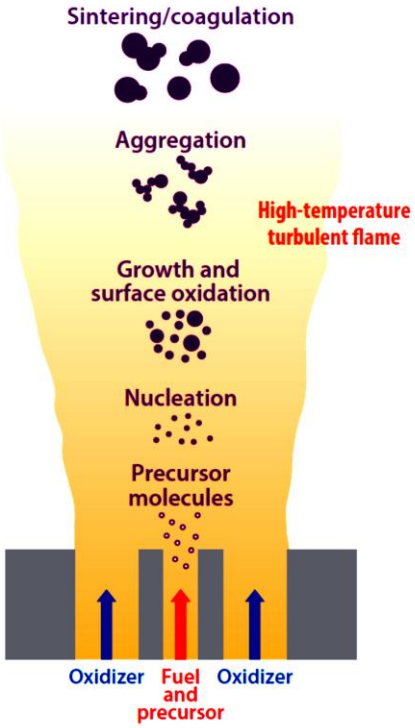

Figure 1.1 Aerosol particle formation and growth processes (Raman and Fox, 2016).

Due to the limitations of methods for measuring the full spectrum of aerosol inherent properties, it is almost impossible to identify and characterize all the atmospheric aerosols in a certain area (Almohammed, 2018; Balachandar and Eaton, 2010; Gelbard, 1979). Besides conducting experiments for describing the aerosol dynamics and chemical reactions (Aardahl and Davis, 1996; Hess et al., 2016;

Raes et al., 1990; Zhao et al., 2018), numerical modelling and simulations become a very useful method nowadays to predict and describe the properties of aerosols. Different numerical modelling methods have been developed and introduced for different scientific and engineering applications (Chen et al., 2014; Davari and Mukherjee, 2018; Gelbard, 1979). The main analyzing process and measuring techniques summarized by Pöschl (2005) are shown in Figure 1.2.

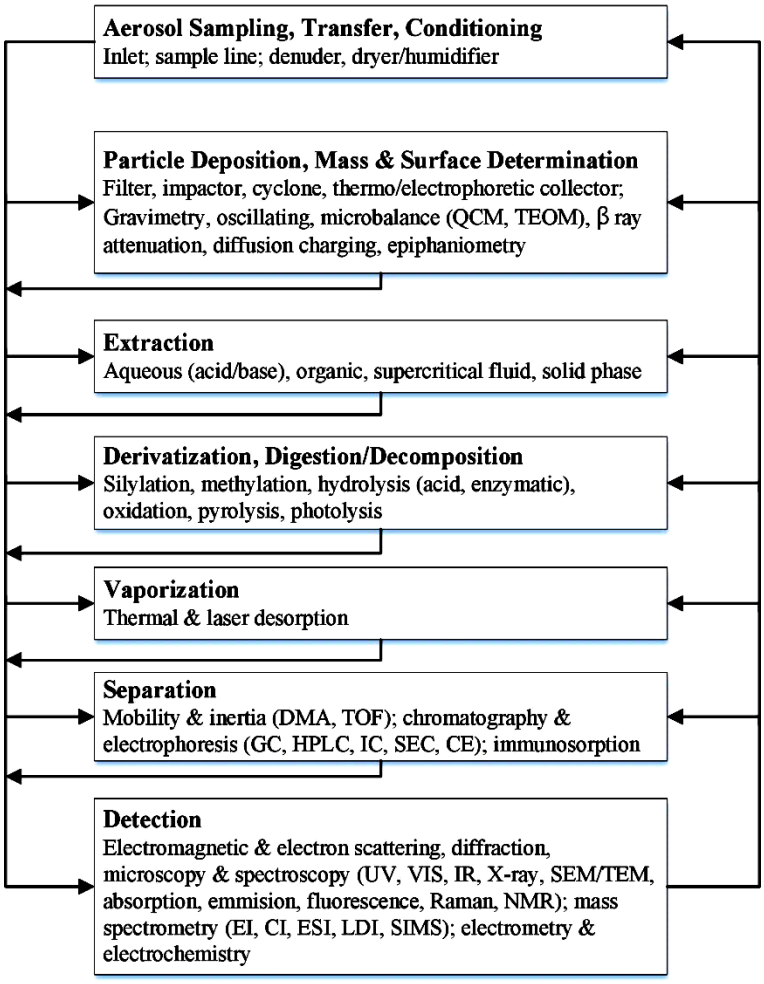

Figure 1.2 Main analyzing processes and measuring techniques for the characterization of aerosols (Pöschl, 2005).

Besides nanoparticle synthesis, aerosols exist in many multiphase flow phenomena in our daily life, such natural phenomenon as rain, snow, air and water

pollution, etc., as well as the industrial processes in power and manufacturing plants worldwide, vehicle and aircraft engines, oil and gas production, etc. All of these phenomena are related to multiphase flows. In the area of fluid mechanics, multiphase flow refers to those fluid flows having more than one phase or component (Brennen, 2005), including materials in different conditions or phases (i.e. solid, liquid or gas), materials with different chemical components but in the same phase (i.e. liquid-liquid systems: wine is alcohol in water). Typically, there are three main kinds of multiphase flows (i.e. gas-liquid, gas-solid, and liquid-liquid flows), and there are also multiphase flow systems including gas, liquid and solid simultaneously. A typical gas-liquid-particle multiphase flow system is shown in Figure 1.3.

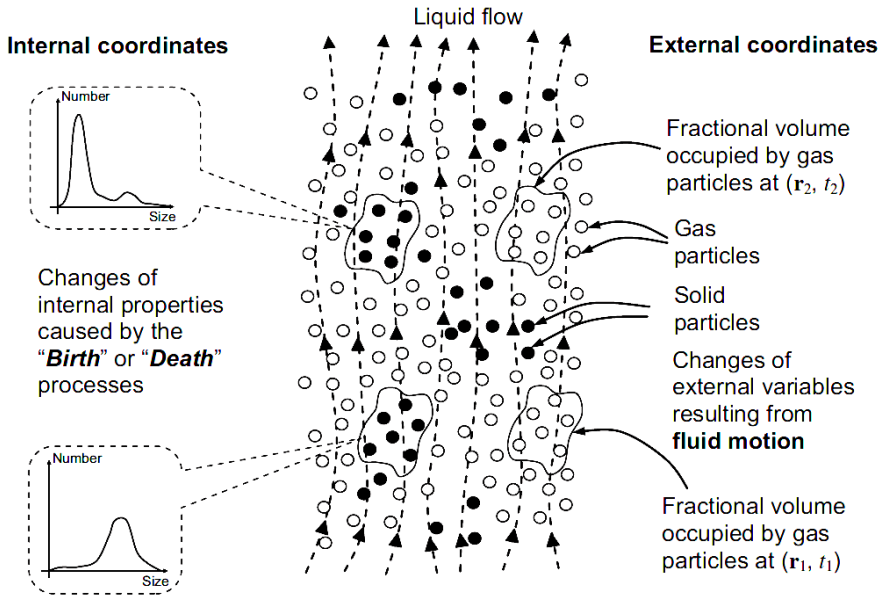

Figure 1.3 A schematic of gas-liquid-particle multiphase flow system (ANSYS, 2013).

In a multiphase flow system, the continuous phase is referred to as the 'carrier'. The dispersed phase is used to describe the solid or fluid particles that are dispersed in the continuous phase. Each of these components is considered to have

its own volume fraction and velocity field. The properties of each phase are very significant to determine the properties of particles (ANSYS, 2013).

In the research field of aerosol dynamic systems, the dynamic behaviors of the aerosol particles can be significantly influenced by the continuous phase. For example, in fuel combustion processes, a vehicle exhaust system or a chimney channel, the temperature gradients and the velocity fluctuations of the surrounding environment should be considered when studying the behaviors of particle formation, collision and surface growth etc. (Olin et al., 2015). Therefore, the solution of the general dynamic equation (GDE) usually involves complex fluid flows and computational fluid dynamics (CFD) which is needed to predict the flow field of aerosols (Mitrakos et al., 2007).

Among the numerical methods developed by researchers, the most popular ones are sectional method (Dergaoui et al., 2013; Gelbard et al., 1998; Rodrigues et al., 2018), the method of moment (Chan et al., 2018b, 2010; Falola et al., 2013; McGraw, 1997; Passalacqua et al., 2018; Yu et al., 2008a), and Monte Carlo method (Fede et al., 2015; Liu and Chan, 2018a, 2017a; Maisels et al., 2004; Wei, 2013). Both sectional method (SM) and the method of moment (MOM) are deterministic methods and exert some merits in solving the GDE. However, compared with Monte Carlo method, both SM and MOM have their disadvantages and limitations when more information and properties of the particles (i.e. particle size distribution, trajectories, or compositional components) are needed.

Nowadays, Monte Carlo (MC) method is widely used because of its advantages (Kruis et al., 2012; Lin et al., 2002; Sun et al., 2004). MC method is

a stochastic algorithm that is based on probabilities of different outcomes in a process that cannot be easily predicted because of its randomness. Instead of solving directly the general dynamic equation, MC method imitates the formation, movement and dynamic behaviors of simulated particles based on the probability of occurrence of these events (Bird, 1976; Efendiev, 2004; Liu and Chan, 2016, 2017a; Zhao et al., 2010). Figure 1.4 shows a typical flowchart of a traditional Monte Carlo method.

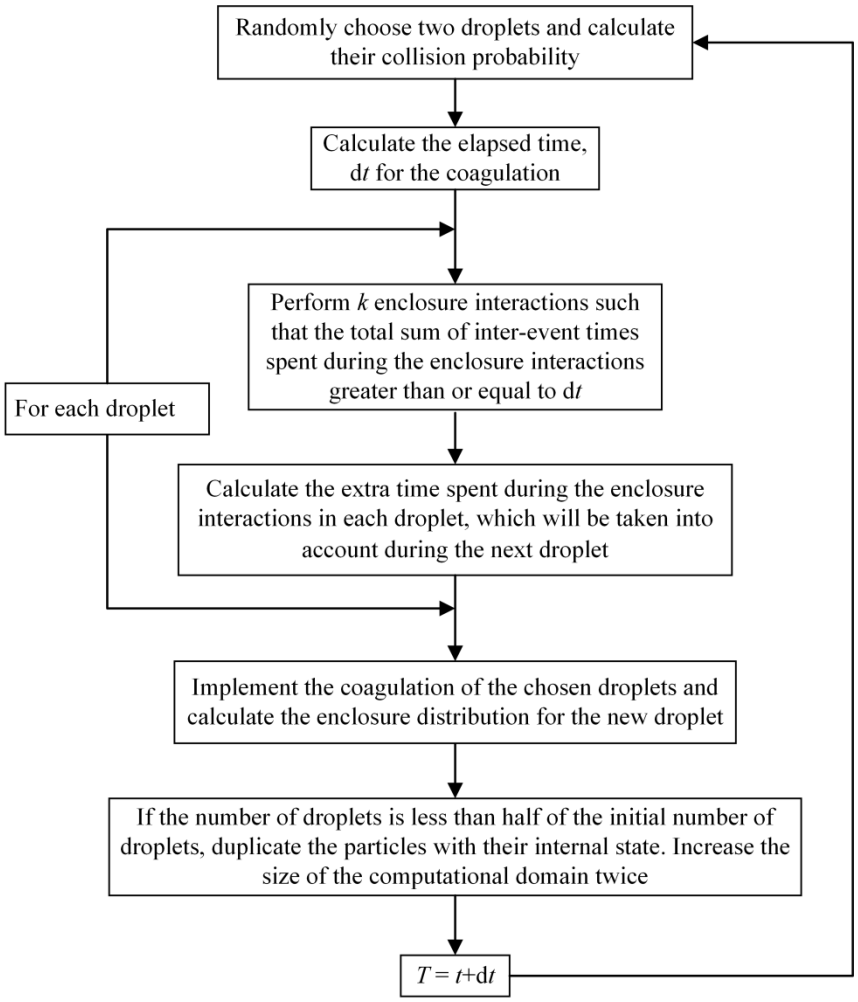

Figure 1.4 A typical flowchart of Monte Carlo method (Efendiev, 2004).

For traditional MC methods, the defects lie in the computational accuracy and efficiency because of its stochastic and statistical characteristics. Both of the computational accuracy and efficiency are related to the number of simulated particles used in MC methods, and increasing the accuracy would result in more computational time consumption (Maisels et al., 2004). However, with the rapid development of computer technology, computers tend to have larger computational memory and faster speed in more economical ways, and the computational memory and time consumption of MC methods is no longer a big problem nowadays. Furthermore, "weighted simulated particles" (Patterson et al., 2011; Rjasanow, 1996) are widely used by MC methods due to the large number of real particles in the actual systems being simulated.

In the previous studies, the same weight for different simulated particles was used (Fox, 2015; Liffman, 1992; Smith and Matsoukas, 1998). In order to reduce the statistical noise, Zhao et al. (2010) proposed a differentially weighted Monte Carlo (DWMC) method, which proved to be efficient and practical for simulating the coagulation process of aerosol particles. Since the deterministic method is more efficient for simulating the nucleation and condensation processes, Zhou et al. (2014) combined stochastic and deterministic methods by adopting the operator splitting (OS) technique in order to take advantage of both stochastic and deterministic methods. Recently, Liu and Chan (2017a) have also proposed and developed a stochastically weighted operator splitting Monte Carlo method.

In the present study, a new differentially weighted operator splitting Monte Carlo (DWOSMC) method based on the idea of operator splitting and different weights for different computational particles is proposed and verified through

complex aerosol dynamic processes. The purpose of this new method aims to solve complex aerosol dynamic problems with high computational accuracy and efficiency, which will provide a better knowledge and insight of the evolution of the aerosol system.

In many natural or engineering applications of aerosol particles, such as the natural phenomenon of acid rain formation and deposition (Fitzgerald et al., 1998; Kolb and Worsnop, 2012; Nah et al., 2018), combustion particulate emissions that can directly affect human health (Fino et al., 2016; Lu, 2005; Zhong et al., 2018), and silica and titania nanoparticles flame synthesis in pigments and catalysts (Fang et al., 2018; Jiang et al., 2007; Pratsinis and Spicer, 1998) and so on, particles often consist of multiple components where the particle size and compositional distributions affect the properties of particles. Many properties of the particles such as light scattering, radioactivity and capturing strategy are highly dependent on the particle size and compositional distributions. Therefore, the proposed DWOSMC method is further developed to study multi-component aerosol dynamics (Liu and Chan, 2018b).

In natural reality or industrial applications, aerosols are usually dispersed in fluid flows. Thus, a better understanding of the population balance of aerosol particles dispersed in a continuous phase requires the solution of the transport problem which is in both the external and internal coordinates. Solving the governing equations of aerosols involve all the terms that exhibit the coupling between turbulent fluid flow and population balance equation (PBE) (i.e., velocity field of the dispersed phase, turbulent viscosity and the aerosol dynamic behaviors). These terms require the solution of a turbulent flow problem and cause the particle-

fluid system to be coupled to the typical Navier-Stokes equations and a turbulence model. The complete numerical model with all external and internal couplings can be schematically given as in Figure 1.5.

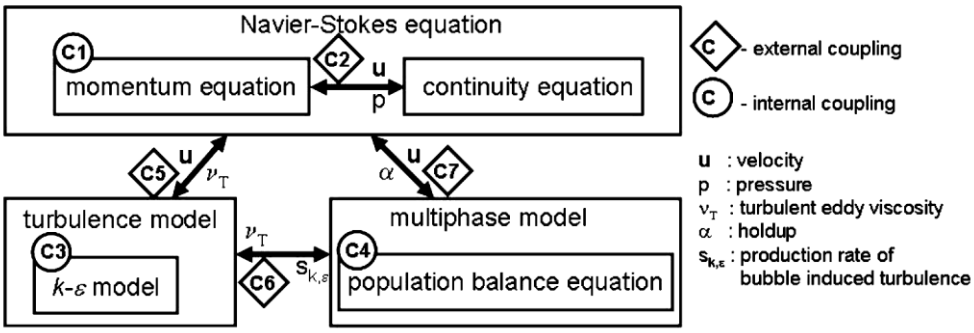

Figure 1.5 Sketch of the coupling effects inside the complete model (Bayraktar, 2014).

Different numerical modelling codes have been developed in computational fluid dynamics (CFD) for coupling the aerosols and the fluid flow. There are typically two numerical modelling approaches for aerosol dynamics coupling in CFD. They are Eulerian (i.e., solution in fixed positions) and Lagrangian (i.e., solution along the streamline) models, respectively (He and Zhao, 2016). The Eulerian method can provide the dimensional information of the flow fields, and is usually used to examine the spatial distributions of particles (Olin et al., 2015; Rodrigues et al., 2018; Tsantilis et al., 2002). The Lagrangian model tracks the motion of each individual particle and can provide specific information about the particulate flow (Hu et al., 2001; Sweet et al., 2017; Veroli and Rigopoulos, 2010). Both of these two models have been developed and reported (Kruis et al., 2012; Liu and Chan, 2017b; Olin et al., 2015; Pyykönen and Jokiniemi, 2000).

In the present study, the proposed DWOSMC method is also coupled into an Eulerian-Lagrangian model to investigate the dynamic behaviors and distributions

of nano- and ultrafine particles dispersed in turbulent flows. Firstly, solid particle-laden flow in spatially inhomogeneous turbulent flows is presented where particles are injected downstream of a square-rod obstacle, and the effects of several factors (i.e., Stokes number, two-way coupling, turbulent dispersion model, and Reynolds number) on the particle dispersion pattern are studied. Further research is also conducted on the coupling of the DWOSMC method with a computational fluid dynamics (CFD) method to study the evolution and distributions of aerosol particles in a turbulent jet. Suitable CFD methods (e.g., Reynolds-Averaged Navier-Stokes (RANS) or large eddy simulation (LES)) are considered to couple with Lagrangian particles to precisely describe the behavior of particles suspended in turbulent flows.

1.2 Research Motivation and Objectives

In the present study, a differentially weighted operator splitting Monte Carlo (DWOSMC) method is firstly proposed for simulating complex aerosol dynamics through coupling the stochastic Monte Carlo (MC) method and deterministic integration methods by the operator splitting (OS) technique. Then this Monte Carlo method is coupled into computational fluid dynamics (CFD) for describing particle-laden multiphase flows.

The objectives of the present study are as follows:

1. To gain a better understanding of the behavior of aerosol particles, the particle distribution characteristics, as well as its applications in engineering and environmental sciences;

2. To verify a newly proposed and developed differentially weighted operator splitting Monte Carlo (DWOSMC) method in both one component and multi-component aerosol systems;

3. To develop a computational fluid dynamics (CFD) based Monte Carlo method in the coupling of fluid flow and particle dynamics in turbulent flows, taking into consideration the interaction between continuous and discrete phases in inhomogeneous systems; and

4. To evaluate the computational efficiency and accuracy of this newly proposed CFD-Monte Carlo method for simulating complex aerosol dynamics in turbulent particle-laden flows and provide a better insight into the interaction between turbulence and aerosol particles.

1.3 Outline of the Thesis

Chapter 1 introduces an overview of the background and scope related to the present study, indicating the research gap of the numerical modelling and simulations of complex aerosol dynamics in turbulent flows. The objectives of the present study are intended to fill this research gap.

Chapter 2 provides a more detailed literature review of aerosol dynamics and multiphase flows including the knowledge and information obtained from previous studies, indicating the development and state-of-the-art that the researchers have acquired, and the shortcomings of these research areas and where the research gap lies.

Chapter 3 provides theoretical fundamentals of the present study, which contains the necessary mathematical and numerical models that will be used in Chapters 4 to 7.

Chapter 4 provides a newly proposed and developed DWOSMC method with its verification and applications to simultaneous complex aerosol dynamics.

Chapter 5 extends this newly developed DWOSMC method to simulate multi-component aerosol systems.

Chapter 6 presents an Eulerian-Lagrangian Monte Carlo method with applications to the study of the interaction between turbulence and particles in inhomogeneous particle-laden turbulent flows.

Chapter 7 provides the extension of this newly proposed and developed CFD-Monte Carlo method to predict the evolution of aerosol particles in turbulent flows.

Chapter 8 provides the conclusions and major scientific findings revealed by the present study and some recommendations for future work.

Chapter 2 Literature Review

2.1 Aerosol Dynamics in Particle-Fluid Systems

Aerosols are of great significance for atmospheric science, biosphere, climate change, public health, air pollution, etc. (Pöschl, 2005). There are multifarious phenomena concerning aerosol dynamics in nature as well as in human activities. The following sections review briefly some typical environmental and engineering aspects regarding aerosol dynamics in multi-phase systems.

2.1.1 Atmospheric aerosols and formation

Atmospheric aerosols refer to fine and ultrafine liquid or solid particles suspended in the atmosphere. Due to its optical properties, microphysical characteristics and absorbing or releasing radiation, atmospheric aerosols affect significantly on human health, the earth's energy budget and climate change, as well as the precipitation efficiency (Huang et al., 2014; Pöschl, 2005).

The atmosphere is inhomogeneous in different areas, so as the aerosols. Fig. 2.1 shows the one-day-time evolution of particle number concentrations (PN_s), ozone (O_3), sulfur dioxide (SO_2) and total volatile organic compounds ($TVOC_s$) in Hong Kong (Lyu et al., 2018). It can be observed that the particles and gases studied are distributed inhomogeneously even in two areas of the same city.

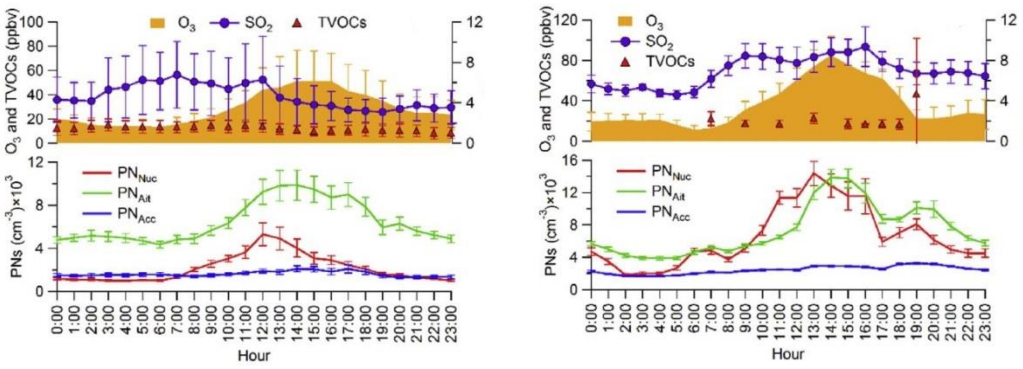

Figure 2.1 Average diurnal patterns of particle number concentrations (PN_s), ozone (O_3), sulfur dioxide (SO_2) and $TVOC_s$ (total volatile organic compounds) at (a) southeastern and (b) southwestern Hong Kong (Lyu et al., 2018).

The concentrations and sizes of aerosols can be highly variable from several nanometers (nm) to 100 micrometers (μm) (Boucher, 2015). The statistics of mass concentrations and the average particle diameter of aerosol particles in different areas is shown in Table 2.1 (Kommalapati and Valsaraj, 2009; Valsaraj and Kommalapati, 2009).

Table 2.1 Mass concentrations and average particle diameter of aerosols in different areas (Kommalapati and Valsaraj, 2009; Valsaraj and Kommalapati, 2009).

Area	Concentration (μg/m^3)	Diameter (μm)
Urban	>100	0.03
Rural	30-50	0.07
Marine	>10	0.16

The sources of atmospheric aerosols vary from a wide range of both natural and man-made behaviors. There are usually two kinds of ultrafine and fine particles in the atmosphere: primary and secondary particles. Primary particles are usually quite small in size and directly emitted as liquid droplets or solid particles from

natural sources such as spontaneous combustion, volcanic eruptions, and biomaterials (e.g., plant debris, microbial carcasses, pollen, etc.) or from anthropogenic sources such as vehicle exhaust systems, fuel combustion process, mineral dust, etc. On the other hand, the secondary particles mostly generate from certain gaseous precursors through chemical or physical processes (such as, nucleation, condensation) in the atmosphere (Sunol et al., 2018). Boucher (2015) has summarised the quantity of aerosols and corresponding precursors emitted from different sources for both the primary and secondary aerosols as shown in Table 2.2.

Table 2.2 Emission fluxes from different sources for primary aerosols and secondary aerosols (Boucher, 2015) where Tg = 10^{12} g = 1 million of tons and Gg = 10^{9} g = 1 thousand of tons.

Aerosol type	Emission flux (per year)
Natural primary aerosols	
Desert dust	1000–3000 Tg
Sea spray	1000–6000 Tg
Biomass burning aerosols	20–35 Tg
Terrestrial primary biogenic aerosols	Order of 1000 Tg
Including bacteria	40–1800 Gg
Including spores	30 Tg
Precursors of natural secondary aerosols	
Dimethylsulphide (DMS)	20–40 Tg Sulfur
Volcanic sulfur dioxide (SO_2)	6–20 Tg Sulfur
Terpenes	40–400 Tg
Anthropogenic primary aerosols	
Industrial dust	40–130 Tg
Biomass burning aerosols	50–90 Tg
Black carbon (from fossil fuel)	6–10 Tg
Organic carbon (from fossil fuel)	20–30 Tg

Anthropogenic secondary aerosols	
Sulfur dioxide (SO_2)	70–90 Tg Sulfur
Volatile organic compounds (VOCs)	100–560 Tg Carbon
Ammonia (NH_3)	20–50 Tg Nitrogen
nitrogen oxide (NO_X)	30–40 Tg Nitrogen

As the aerosol particles are exposed to an open atmosphere, they would undergo all kinds of chemical reactions and physical transformations. Therefore, the particles size distribution, chemical composition and structure will experience considerable variation over time. The main atmospheric cycling of aerosols including the whole process from being emitted to deposition is shown in Figure 2.2.

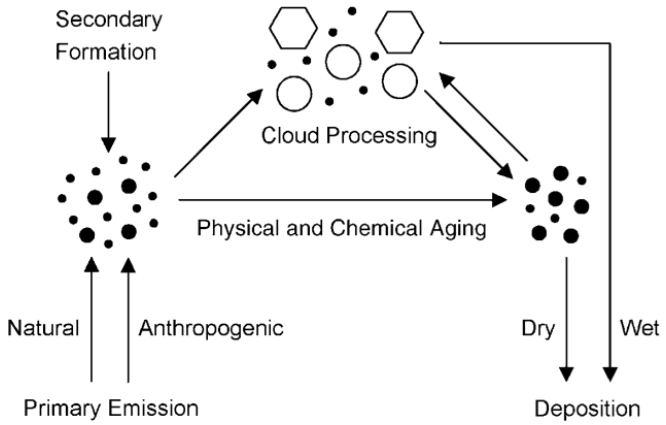

Figure 2.2 Atmospheric cycling of aerosols (Pöschl, 2005)

The growth of particle surface or volume of aerosols can be considered as a two-stage process. In the first stage, monomers or molecules of the condensable species are produced through gas-phase chemical reactions. In the second stage, these monomers or molecules collide and combine to clusters, which will grow further by condensation. Then these clusters nucleate into more stable aerosol particles, and aerosol particles subsequently grow by the processes of coagulation and condensation (Kalani and Christofides, 2002).

One main source that contributes to the considerable quantity of aerosol particles is the burn of biomass and fossil fuels, not only producing black carbon and organic carbon, but also sulphur dioxide that can convert into sulphate aerosols. The emission quantity from the combustion for a given species (Boucher, 2015):

$$E=\sum_{i} A_i EF_i(1-\alpha_i) \tag{2-1}$$

where A_i refers to the fuel consumption for activity i, EF_i refers to the emission factor for activity i, and α_i is the efficiency for emission reduction of the mitigation technology.

In order to study the chemical structures of aerosols, besides the reactants and the products of the entire chemical reactions, the specific chemical mechanisms of the reactions are also needed. For example, the existence of nitrogen oxides (NO_x) in the atmosphere has a negative effect on the conditions of human health and the climate change because of its influence on the concentration of ozone (O_3) in the atmosphere. The formation and removal of tropospheric NOx are listed in Equations (2-2) to (2-11) (Dentener and Crutzen, 1993):

(R1)	$NO_2+OH+M\rightarrow HNO_3+M$	(2-2)
(R2)	$HNO_3+h\nu\rightarrow NO_2+OH$	(2-3)
(R3)	$NO_2+ O_3\rightarrow O_2 +NO_3$	(2-4)
(R4)	$NO_3+NO_2 +M\rightarrow N_2O_5+M$	(2-5)
(R5)	$N_2O_5+M\rightarrow NO_3+NO_2 +M$	(2-6)
(R6a)	$NO_3+h\nu\rightarrow NO+ O_2$	(2-7)

(R6b) $NO_3 + h\nu \rightarrow NO_2 + O$ (2-8)

(R7) $N_2O_5 + h\nu \rightarrow NO_3 + NO_2$ (2-9)

(R8) $N_2O_5 + H_2O \xrightarrow{\text{aerosol}} 2HNO_3$ (2-10)

(R9) $NO_3 \xrightarrow{\text{aerosol}} \text{products}$ (2-11)

In the past several decades, physical chemists have focused their attention on understanding the generation processes, chemical components, and dynamic behaviors of atmospheric aerosol particles and droplets. They have developed a foundation of experimental and theoretical investigation of the physical and chemical characteristics, mass and energy transport, and dynamics of processes occurring at nanoscale gas-liquid and gas-solid flows (Kolb and Worsnop, 2012). Ziemann et al. (2012) conducted the study of mechanisms, products, and dynamics of secondary organic aerosols (SOA) formation. Bzdek et al. (2012) summarized the methods that existed for particle chemical analysis of ambient ultrafine. Laskin et al. (2015) reported an overview of the chemical composition of SOA and the physicochemical characterization of the atmospheric brown carbon. Bressi et al. (2016) investigated the chemical composition of non-refractory PM using an aerosol chemical speciation monitor. Sunol et al. (2018) numerically studied the oxidation of volatile organic compounds (VOCs) to form secondary organic aerosols in a laboratory chamber over a range of physicochemical conditions.

2.1.2 Multi-component properties of aerosols

In the research field of air pollution and global climate change, the understanding of the atmospheric aerosol particles looping is significantly important. Figure 2.3 shows the interaction effect of aerosol chemical composition, particle

properties, climate and human health effects, and aerosol sources. The chemical structure and reactions of the particles are involved in almost all this atmospheric loop, and the particle size and compositional distributions of the aerosol particles can significantly affect the physical and chemical reactivity, capturing properties, and their effects on human's health. Therefore, a complete and scientific understanding of particle component compositional transformation and distribution is essentially required for the effective control of aerosol effects on global climatic change and human health.

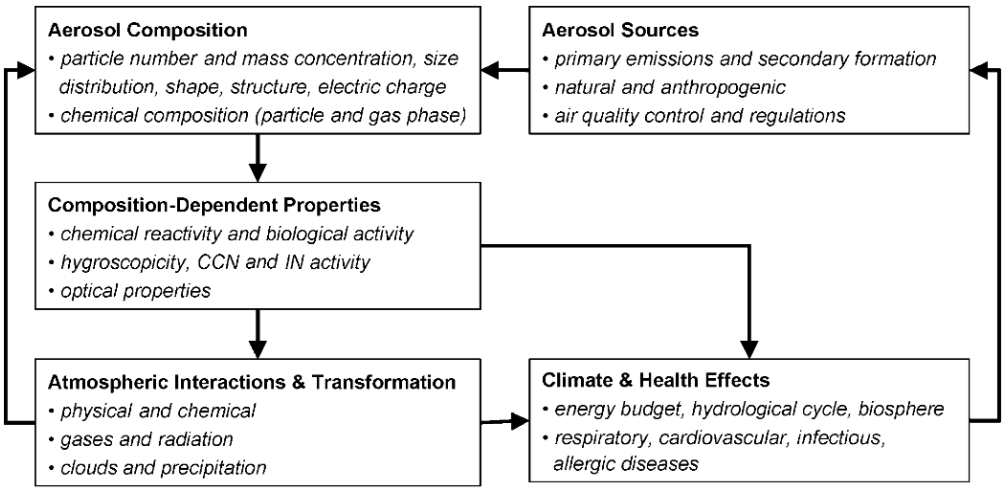

Figure 2.3 Interaction effect between atmospheric aerosol compositions, properties, climate and health, and sources (Pöschl, 2005).

Aerosols are essentially multivariate fine particulates with complicated chemical reactions and compositions. The dynamic behaviors of aerosol particles are related to many engineering and scientific applications and problems, such as acid rain formation and deposition (Fitzgerald et al., 1998; Kolb and Worsnop, 2012; Nah et al., 2018), combustion particulate emissions (Fino et al., 2016; Lu, 2005; Zhong et al., 2018), and silica and titania nanoparticles flame synthesis in pigments and catalysts (Fang et al., 2018; Jiang et al., 2007; Pratsinis and Spicer, 1998) and

so on. In these areas, particles often consist of multiple components and compositional inhomogeneity, and the particle size and compositional distributions affect the properties of particles. Figure 2.4 shows the particle number distribution of aerosol particles in a two-component system, from which it can be observed that the bivariate population balance modeling contains both particle size and composition information (Zhao et al., 2010).

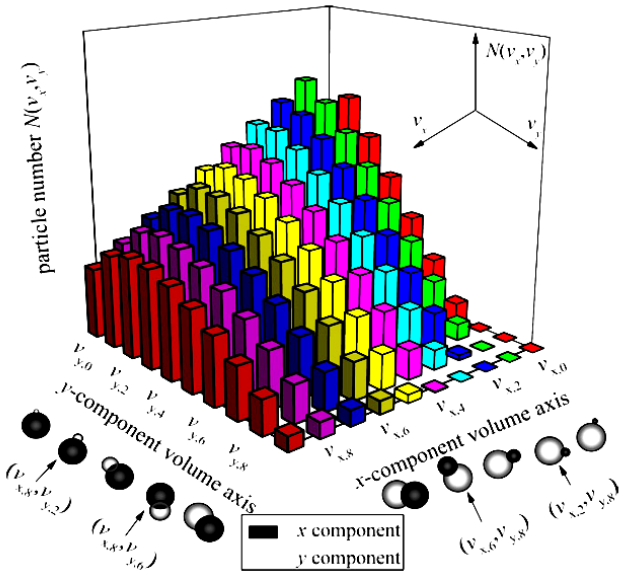

Figure 2.4 Schematic illustration of the particle number distribution in a two-component system (Zhao et al., 2010).

Over the past several decades, considerable efforts have been taken to numerically solve the general dynamic equation (GDE), most of these efforts are devoted to solving one-component aerosol processes (Liu and Chan, 2018a, 2017a; Maisels et al., 2004; Zhao et al., 2005a; Zhou et al., 2014). Other researchers have also focused on multi-component aerosol processes. Gelbard and Seinfeld (1980) developed a sectional method for simulating variations in aerosol particle size and compositional distributions for coagulation, chemical reaction and growth processes. Later on, Gelbard (1990) further presented a moving-sectional method for modeling

multi-component condensation. Kim and Seinfeld successively proposed a moving sectional method (Kim and Seinfeld, 1990), a numerical technique coupling repeated upwind difference method (RUD) and the Taylor-Galerkin method (TGFEM) (Kim, 1992) to obtain the multivariable size-composition distributions of aerosol systems based on simultaneously occurring coagulation and condensation processes. Katoshevski and Seinfeld (1997a) first developed an analytical solution for multi-component aerosol dynamics based on particle condensation/evaporation. Based on this developed method, Katoshevski and Seinfeld (1997b) further proposed an analytical-numerical method for the solution of multi-component aerosol GDE accounting for growth, removal, particle sources, and coagulation. Sun et al. (2002; 2004) sequentially used the sectional method and Monte Carlo method to simulate two-component aerosol dynamics including coagulation and condensation processes, respectively. Korhonen et al. (2004) introduced a size-segregated multi-component aerosol dynamics model for investigation of the tropospheric layer aerosol particles. Matsoukas et al. (2009), Efendiev (2004) and Zhao and Zheng (2011) simulated the two-component coagulation of different kernels using Monte Carlo method. Matsoukas et al. (2006) introduced the aggregative mixing degree, which can influence particle size and compositional distributions. Later, Lee et al. (2008) demonstrated that the steady-state mixing degree is the single parameter to determine the width of the compositional distribution in bicomponent aggregation systems. Zhao et al. (Zhao and Kruis, 2014; Zhao et al., 2011; Zhao et al., 2016) further studied the evolution of the aggregative mixing degree for different aggregation regimes and initial conditions for two-component aggregation. Palaniswaamy (2007) used the direct simulation Monte Carlo (DSMC) method to investigate multi-component aerosol dynamics of coagulation, deposition, growth,

and source reinforcement. Fu et al. (2015) developed a finite element method for solving multi-component aerosol dynamic equations based on processes of coagulation and condensation. Kaur et al. (2017) developed two discretization methods respectively based on number and mass forms to solve multivariate aggregation population balance equation**,** and particle moments and number distributions are observed and verified through analytical solutions for different aggregation kernels. Kaur et al. (2009) and Singh et al. (2018) compared two numerical methods (i.e., the cell average technique and the finite volume scheme) for solving aggregation and breakage processes, and bivariate aggregation process, respectively. They both found that the finite volume scheme is computationally more accurate and efficient.

2.1.3 Aerosol dynamic processes

When exposed to an open atmosphere or environment, aerosol particles experience a series of processes that can affect the particle number concentration, particle size distribution, mass loading and other properties of aerosols. Typically, the main processes are shown in Figure 2.5 (Lu, 2005), including advection, nucleation, coagulation, condensation, evaporation, emission and deposition.

Advection refers to the spatial movement and dispersions of the particles due to the influence of the carrier flows. Aerosols can be carried from place to place because of the advection and diffusion effects of continuous gas phase.

Nucleation refers to the formation of aerosol particles from the agglomeration of finer particles in gases; it is a process of conversion of gases to particles.

Coagulation refers to the process that particles collide with one another and stick together to form a new bigger particle (Lin et al., 2015). Coagulation process does not alter the mass loading of aerosol particles in gas but will result in the variation of particle number concentration and particle size distribution of aerosols.

Condensation refers to the process that gas phase components condense onto the existing aerosol particles, and it is the reverse process of evaporation, which is the particle-to-gas mass transfer process and particle component will evaporate to gases.

Emission refers to the process of particles released from different sources are added into the existing aerosol system.

Deposition refers to the process of particles being captured by face and removed from the existing aerosol system, and it can be classified into dry or wet deposition.

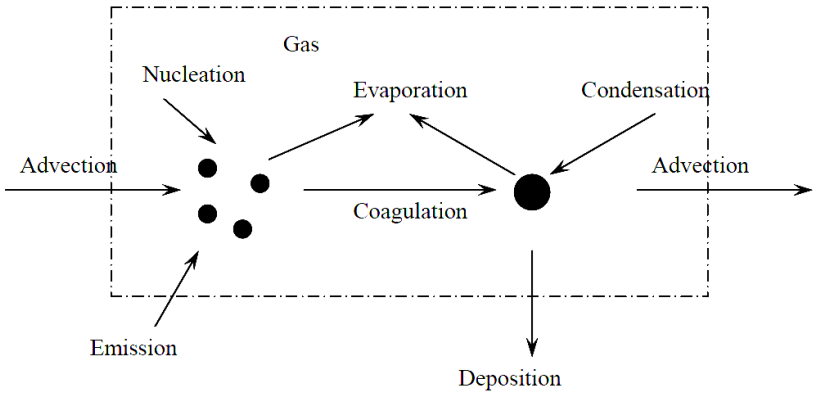

Figure 2.5 Typical aerosol dynamics processes in an aerosol system (Lu, 2005).

2.2 Numerical methods for the simulation of aerosol dynamics

Firstly, aerosol transport theory is based on Stokes' law including semi-empirical corrections made by Millikan in his measurements of the electronic charge.

Einstein's theory of the Brownian motion plays a central role in aerosol diffusion (Friedlander, 2000). The Brownian motion resulting in coagulation was firstly explained theoretically by Smoluchowski (Liffman, 1992). Later, more and more researchers in aerosol science introduced all kinds of new ideas and concepts based on these theories to further describe the behavior of aerosol particles. The dynamic behaviors and number density evolution of aerosol particles are described by a population balance equation (PBE) or general dynamic equation (GDE) (Friedlander, 2000), which are described in Chapter 3.

Since the GDE is a nonlinear and partial integro-differential equation (Prakash et al., 2003), only simple analytical and some approximate solutions are given for several cases in which two or more processes that modify the particle size distribution are occurring simultaneously. To get the solution for those cases in which several processes are occurring simultaneously, especially in the multi-component and heterogeneous cases, numerical solutions are usually required. There are already a number of studies about the different numerical methods used to solve the GDE reported, and the most popular ones are the sectional method, the method of moment, and the Monte Carlo method.

2.2.1 Sectional method

Sectional method (SM) is a kind of discrete aerosol size distribution approach. In a sectional representation, the size of the particles is divided into a certain number of sections and all the particles in one section have the same component composition. The particle number distribution function is integrated in every section, and connections among sections are accomplished by the coagulation kernel. By classifying particles into different size bins, different compositions of

particles are allowed for different sizes of particles (Lu, 2005). Because the precision of the sectional method is mainly related to the number of sections, and more sections means requirements for higher computer configuration, computational constraints rely on the maximum number of sections.

There are two kinds of sectional method. The first one is the fixed sectional method, the sectional size boundaries are fixed and particles in the same section have a uniform composition. The middle size of a bin is usually used to represent the size of all particles. The fixed sectional method has a very simple size structure, and it can cover a wide range of particle sizes if the sectional boundaries are set big enough. The second one is the moving sectional method where the boundaries of sections are no longer fixed. With the growth of particles, instead of moving particles from one section to another, the section itself moves.

Based on the sectional method, Prakash et al. (2003) developed a model that described particles in discrete nodal form. Figure 2.6 shows a typical illustration of the nodes used in the sectional method and its algorithm (Prakash et al., 2003). It can be seen that the volume range of the aerosol system is divided into multiple nodes and particles only exist at these nodes. Nucleation occurs at a critical size of v^* and coagulation can occur between different nodes. Kumar et al. (2006; 2008) investigated the particle size distributions related to aggregation, breakage, growth and nucleation problems using sectional method. Later on, Kumar et al. (2009) compared their proposed sectional method to a finite volume scheme (Filbet and Laurençot, 2004) for aerosol aggregation and breakage, and concluded that the sectional method is superior to the finite volume scheme in computational accuracy. Kochenburger et al. (2017) focused on a semi-implicit size-discrete method for

polydisperse aerosol coagulation and pointed out some modifications to reduce the errors of discretization. Recently, Aubagnac-Karkar et al. (2018) and Rodrigues et al. (2018) have applied the sectional method to predict the formation and growth of soot particles in laminar and turbulent flames, respectively, considering the processes of nucleation, condensation, surface growth and oxidation, and coagulation.

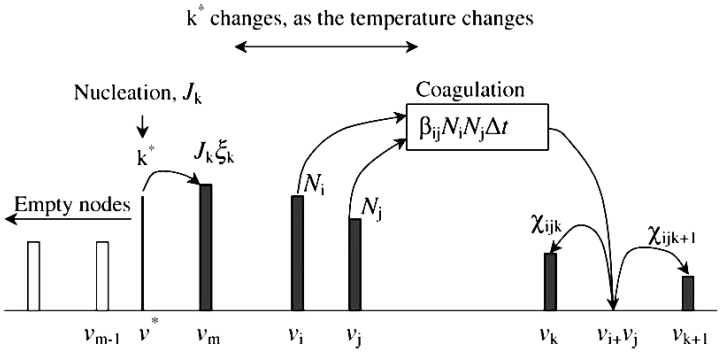

Figure 2.6 Illustration of the algorithm of sectional method (Prakash et al., 2003).

The sectional method usually can give a relatively accurate prediction of the particle size distribution, and takes moderate computational time (Chen et al., 2014). But it has its own disadvantage, its sectional representations often result in numerical diffusion or fairly complicated algorithms (Wei, 2013).

2.2.2 Method of moments

The moment method (MOM) is a quite different disposition of the GDE when compared with the sectional method. The coagulation process is expressed by the well-known Smoluchowski's equation (Equation (2-12)), in MOM, it is transformed into a set of ordinary differential equations regarding the moments, which can be obtained by multiplying Equation (2-12) by v^k and integrating it over

the whole particle size regime (Chen et al., 2014). Equation (2-12) can be further expressed as Equation (2-13),

$$\left[\frac{\partial n}{\partial t}\right]_{\text{coag}} = \frac{1}{2}\int_0^v K(v-\tilde{v},\tilde{v})n(\tilde{v})n(v-\tilde{v})\mathrm{d}\tilde{v} - \int_0^\infty K(v,\tilde{v})n(v)n(\tilde{v})d\tilde{v} \tag{2-12}$$

$$\frac{dm_{\text{k}}}{dt} = \int_0^\infty \int_0^\infty [(v_1+v_2)^{\text{k}} - v_1^{\text{k}} - v_2^{\text{k}}] K(v_1,v_2)n(v_1)n(v_2)dv_1 dv_2 \tag{2-13}$$

The moment of m_{k} is defined by,

$$m_{\text{k}} = \int_0^\infty v^{\text{k}} n(v)dv \tag{2-14}$$

The moments set (often refer to the low order moments) represents the most significant and basic quantities about the particle size distribution, such as the particle number concentration, average diameter, average surface, volume fraction, and the mass flux, etc. Solving the moments set is far more computational time saving and simple in programming than directly solving the GDE.

So the MOM has been widely used in aerosol dynamic simulations. Its primary advantage is that it needs low computational cost, because only several additional moments equations of the particle size distribution (PSD) need to be solved. But unfortunately, the MOM generally requires some kind of closure, which means that the initial form of the PSD should be assumed to obtain the closure of the moment's equations. Moreover, in order to deal with the problem of closure, several moment methods have been developed. The quadrature method of moments (QMOM) proposed by McGraw (1997) has been widely used in many studies (Chan et al., 2010; Chen et al., 2014; Passalacqua et al., 2018; Yu et al., 2008a). Chan et al. (2010) used the direct quadrature method of moments (DQMOM) for

studying the exhaust particle formation and evolution in the wake of the studied ground vehicle. A method named MOMIC (the method of moments with interpolative closure) had been coupled with detailed chemistry to investigate the nanoparticle synthesis in turbulent reactive flows by Akroyd et al. (2011). Yu et al. (2008) developed a new method of moment (i.e., Taylor-series expansion method of moments (TEMOM)) for solving the GDE undergoing Brownian coagulation. In order to accomplish the closure of the moment equations, they adopted the Taylor-series expansion technique through a set of three first-order ordinary differential equations, from which the information for describing aerosol dynamics is easily obtained. Based on MOMIC and TEMOM, Yu and Lin (2017) further proposed a hybrid method of moments with interpolation closure–Taylor-series expansion method of moments (MOMIC–TEMOM) method to solve the Smoluchowski coagulation equation. Recently, Chan et al. (2018) have coupled a developed bimodal TEMOM with large eddy simulation (LES) to study the formation and growth of aerosol particles in turbulent flows. Xie and Yu (2018) have proposed the thermodynamic constraints of Brownian coagulation based on TEMOM which proved to be useful for reducing atmospheric pollutants by changing the specific surface energy of aerosol particles.

Deterministic methods (i.e., SM and MOM) are effective tools to describe or predict the evolution of aerosol particle size distribution, and technically easy to be coupled with Eulerian-Eulerian models of multiphase flows (Zhang and You, 2015). However, these two methods both possess their own advantages and disadvantages in computational accuracy and efficiency (Chen et al., 2014; Kotalczyk and Kruis, 2018; Wei, 2013). For example, SM tends to be more accurate, however, the

sectional representations may lead to complicated algorithms; MOM is relatively computational time saving and simple, nevertheless, the initial form of the particle size distribution should be assumed to obtain the closure of the moment equations. Moreover, although the moment methods mentioned above tend to be quite efficient for computation, the problem of closure makes it rather difficult to deal with complicated aerosol-related problems or models in reality and it also lacks flexibility to some extent.

In conclusion, although deterministic methods have their own advantages in solving the GDE, they both have the drawbacks as follows:

1. The trajectories, history and internal structure of particles cannot be captured;

2. When applying to multivariate aerosol systems, these methods will lose their simplicity and efficiency.

2.2.3 Monte Carlo method

Monte Carlo (MC) method is an excellent candidate for dealing with the complex aerosol system. The stochastic and discrete nature of MC method is the same with the Brownian motion of the particles. By using the stochastic process, large quantities of particles are used in the numerical calculations, and the coagulation behavior of the particles is the result of random Brownian motions (Maisels et al., 2004). In addition, the trajectory, evolution history and the composition of the particles can be obtained in MC method. It is especially preferred for solving polydispersed and multi-variant GDE even in cases that consider fractal coagulation, restructuring and chemical reactions (Zhao et al., 2005c).

Metropolis and Ulam (1949) first proposed MC method applying the laws of probability and statistics to the natural sciences. Bird (1994, 1976, 1963) developed the direct simulation Monte Carlo (DSMC) method for modeling rarefied gas flows. Later on, many types of MC methods have been proposed to study the aerosol dynamics, which can be generally classified into time-driven MC method (Liffman, 1992; Liu and Chan, 2017b) and event-driven MC method (Mendoza-Coto, et al., 2016; Zhao and Zheng, 2009) with respect to the advancement method of the algorithm; or constant-number MC method (Lin et al., 2002; Liu and Chan, 2018a; Zhao and Zheng, 2013) and constant-volume MC method (Yamakov, 2016; Zhao and Zheng, 2009) with respect to the variation of computational domain. Kostoglou and Konstandopoulos (2001) identified the characteristics of different MC approaches and classifications. Weighted MC methods (Boyd, 1996; Kotalczyk and Kruis, 2018; Liu and Chan, 2017b; Zhao et al., 2010) have also been proposed to increase their computational resolution and efficiency. Researchers have also tried to increase the computational efficiency of MC methods by using parallel processing technology (Kotalczyk and Kruis, 2018; Wei and Kruis, 2013; Zhou et al., 2014).

Among the MC methods developed in recent years, the stochastic weighted particle method (SWPM) (Deville et al., 2011; Patterson et al., 2011), multi-Monte Carlo (MMC) method (Haibo et al., 2005; Zhao et al., 2005c), differentially weighted time-driven MC (DWTDMC) method (Zhao et al., 2009; Zhao et al., 2010) and the Operator Splitting Monte Carlo (OSMC) (Liu and Chan, 2017; Zhou et al., 2014) method are relatively more computationally efficient.

DWTDMC method proposed by Zhao et al. (2009) could overcome the

drawbacks of the traditional MC methods. It can weaken the contradiction between the large number of real particles and the limitation of the central processing unit (CPU) speed and computer memory capacity by using different weights for different simulated particles. In the operator splitting Monte Carlo method (OSMC) proposed by Zhou et al. (2014), the operator splitting method is utilized to split the whole aerosol dynamic process into two types. One is the coagulation process which is stochastic and is simulated by the direct simulation MC algorithm. The other is the type of deterministic processes that include nucleation and condensation processes, which are solved by deterministic integration method. This is because, stochastic simulation of the coagulation process is computationally more efficient than directly solving the Smoluchowski equation; nevertheless, the deterministic method is more computationally efficient for simulating nucleation and surface growth (Zhou and Chan, 2016). The OSMC method proves to be rather flexible and efficient for simulating aerosol dynamics through the combination of stochastic and deterministic methods. Figure 2.7 shows the simplified flowchart of the implementation of OSMC method (Zhou et al., 2014b).

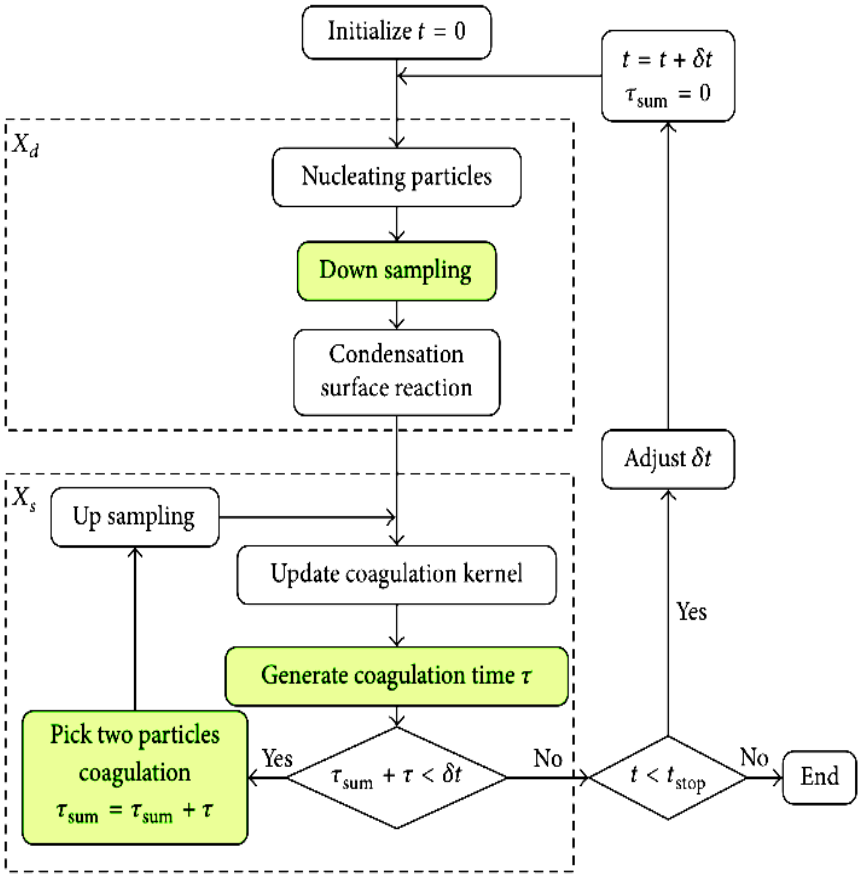

Figure 2.7 Flowchart of the OSMC (Zhou et al., 2014b).

Recently, Liu and Chan (2017) have developed a new method named stochastically weighted operator splitting Monte Carlo (SWOSMC) which is based on the OSMC (Zhou et al., 2014b), and SWPM (stochastically weighted particle method) (Rjasanow, 1996). This new method has been proved to have good computational efficiency and accuracy in dealing with the problems of complex aerosol systems, especially for simultaneous aerosol dynamic processes.

Among these methods (SM, MOM and MC) mentioned above, MC methods are becoming more and more preferred by researchers because of the following advantages (Wei and Kruis, 2013),

(a) The stochastic nature of MC makes it ideally suitable to deal with the stochastic event;

(b) MC method can solve the closure problem of general dynamic equation (GDE);

(c) Each simulated particle can have its unique size, composition and morphology, i.e., any information about the particles can be obtained; and

(d) It is simple and robust to code numerically.

2.3 Direct Simulation Monte Carlo method

2.3.1 Overview

Direct simulation Monte Carlo (DSMC) method utilizes the probabilistic simulation to solve the Boltzmann equation for fluid flows. It was firstly proposed by Bird (1976) for simulating rarefied gas flows where the Knudsen number, *K*n is very large, as in such atmospheric environment, the assumption of continuous fluid is no longer appropriate, the stochastic method should be used.

A remarkable advantage of DSMC method in simulating aerosol particles is that its statistical and stochastic nature is the same with the Brownian motion of the particles. It is a stochastic algorithm which is based on probabilities of different outcomes in a process which could not be easily predicted because of its randomness. By tracking representative particles through space and considering collisions between particles, the DSMC method can directly simulate the physics of aerosol dynamics.

2.3.2 Particle representation and the concept of "weight"

In the numerical simulation process of DSMC, simulated particles are used to represent a certain amount of real physical particles in order to overcome the conflicts between the large number of real particles and the limitation of computer capabilities. Every simulated particle can be considered as a representative sample of real particles with the same associated properties (i.e., density, species, velocity, size, etc.). Each simulated particle is weighted by a proper number (Boyd, 1996).

Figure 2.8 shows a schematic representation of the real particle and simulation (fictitious) particle systems (Zhao et al., 2005a). It vividly presents that particles with the same size and properties are simulated by smaller number of simulated particles that possess the same size and properties.

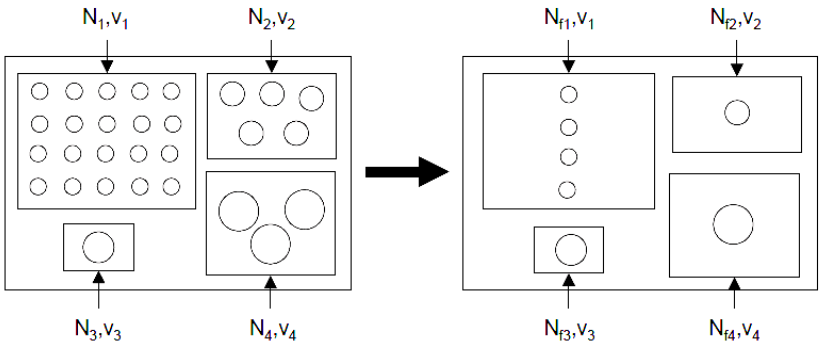

Figure 2.8 Graphic illustration of the relation between real particle and simulated particle systems (Zhao et al., 2005a).

Several different concepts exist on how to choose the weighting scheme and how to carry out the effect of weighting. Rjasanow (1996) and Liu and Chan (2017a) used simulated particles with varying mass weights, simulated particles are assigned with a certain mass of real particles. Deville et al. (2011) conducted the action on the simulated particles according to the probability, which scales inversely to the

weight of the simulated particles. While Zhao et al. (2010) used the concept of subsystem, every simulated particle represents a number of real particles (He and Zhao, 2016), i.e., every simulated particle has a number-"weight". In the present study, weight w_i is defined as the ratio of the number of real particles over the number of simulated particles, as shown in Equation (2-15) (Zhao et al., 2010):

$$w_i = \frac{N_r(v)}{N_s(v)} \tag{2-15}$$

where $N_r(v)$ is the number of real particles of volume size v and $N_s(v)$ is the number of simulated particles representing these real particles $N_r(v)$.

2.3.3 DSMC simulation procedure

Due to its characteristics of probabilistic and discrete, DSMC method tends to acquire fluctuations and statistical errors. In order to reduce the noise of the simulation results, DSMC simulation is usually based on averaging on several MC loops.

Typically, the simulation procedures of DSMC methods are as follows:

Step 1: Initialization;

Step 2: Assign a MC simulation loop number and a stop time period;

Step 3: Choose a time-step that is suitable for the simulation;

Step 4: Perform calculation on the possible events that may occur;

Step 5: Repeat Steps 3 and 4 until the simulation time reaches the stop time;

Step 6: Start a new MC loop until the loop number reaches the predetermined MC loop number;

Step 7: Obtain the averaged results of several MC simulations;

Figure 2.9 shows the flowchart of a MC simulation that is based on the fast DWMC method developed by Xu et al. (2014).

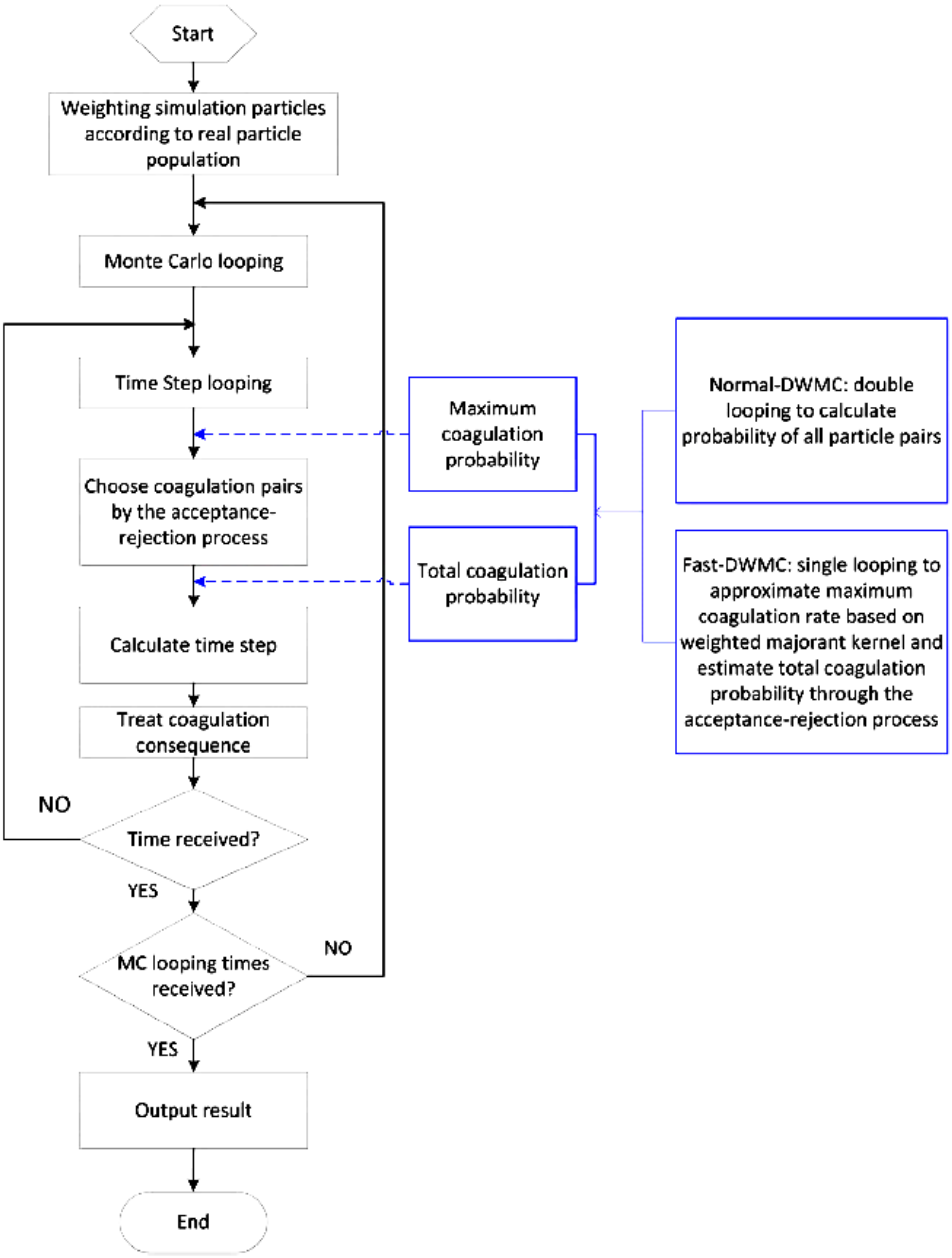

Figure 2.9 Flowchart of the fast DWMC method (Xu et al., 2014).

2.4 Operator Splitting Method

Partial differential equations (PDE) have gained wide applications in various physical phenomena. As the physical phenomena become increasingly complicated,

it becomes more and more difficult to solve these equations. It is common that a model contains different terms (operators) reflecting different physical or chemical processes. A typical example of such PDEs is the reactive species transport equation in the following form (Carrayrou et al., 2004),

$$\frac{\partial c_i}{\partial t} = L(c_i,x,t) + f_i(c_1,\ldots c_i,\ldots c_{N_c}) \quad i=1,\ldots,N_c \tag{2-16}$$

where L refers to the transport operator including advection and diffusion processes, and f_i refers to chemical reactions on the species.

An applicable strategy to deal with such complicated problems is to "divide and conquer". A rather successful approach in this spirit is an operator splitting technique. Operator splitting technique can separate the total process into multiple steps. It firstly solves different sub-processes and then combines the results (Carrayrou et al., 2004; Mclachlan and Quispel, 2002), respectively.

Karlsen and Risebro (1997) used the operator splitting method to decouple the convective and diffusion parts of nonlinear convective-diffusion equations, and to reduce the *m*-dimensional convection problem to several one-dimensional problems. Carrayrou et al. (2004) compared the accuracy of several operator splitting methods (i.e., standard sequential non-iterative (SNI), Strang splitting SNI, standard sequential iterative (SI), extrapolating SI, and symmetric SI approaches) for solving the reactive species transport equations. They found that the symmetric SI scheme is the most computationally accurate and Strang splitting SNI is the second, other schemes have similar accuracy level. Celnik et al. (2007) and Menz et al. (2014) accomplished the full-coupling of soot particles with the gas phase using the operator splitting technique where the soot particles are simulated

using the Monte Carlo method and the gas phase is solved using an implicit ordinary differential equation (ODE) solution accordingly. Ganesan and Tobiska (2012) used an operator splitting finite element method to split the multidimensional population balance equations of crystals into spatial and internal coordinates. The splitting technique is also applied to the coupling of scalar energy and mass balance equations. Schiller (2014) adopted a unified operator splitting method in multi-scale particle-fluid flows to couple the discrete solid or elastic objects to a lattice Boltzmann fluid. The transport of fluids is solved by the lattice Boltzmann method (LBM) and immersed objects are coupled to the flow field by interaction force. Zhou et al. (2014) and Liu and Chan (2017) also recently used the operator splitting technique to couple the stochastic Monte Carlo method with deterministic methods for aerosol dynamics.

2.5 Coupled CFD-PBE Computation of Aerosol Dynamics

2.5.1 Overview

In many aerosol dynamic systems, the behavior of the bulk fluid may have a strong influence on the suspended particles owing to mass, momentum and energy transfer between the aerosols and the fluids. More knowledge of the complicated multi-phase fluid needs to be known if a deeper understanding is needed about the properties of the aerosol particles in the complex particle-fluid systems. The local velocity, temperature and pressure as well as the viscosity of the fluid, the chemical reaction and the mixing status between the particle and the fluid both can contribute to the mass, momentum and energy transfer, as well as the properties of the aerosol particles. These coupling phenomena which are shown in Figure 2.10 will have a significant influence on both the gas and particle phases, and ignoring these factors

and the coupling of fluids and aerosols can give rise to significant errors (Brown et al., 2006).

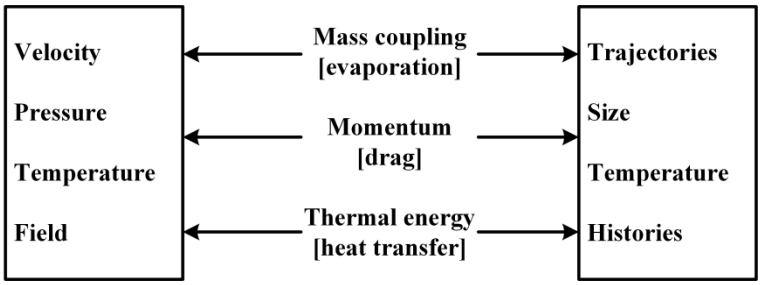

Figure 2.10 Gas-particle coupling phenomena (Crowe et al., 1977).

2.5.2 Particle-fluid coupling strategies

With regard to the coupling of the fluids and particles, computational fluid dynamics (CFD) offers a framework for simulating aerosol dynamics. The use of CFD for predicting gaseous and particulate emissions is becoming a powerful tool for the design, optimization and testing of low-emission and high-performance burners (Zucca et al., 2006).

Different modelling codes have been developed in CFD for coupling the aerosols and the fluid flow. There are typically two modelling approaches for CFD. They are Eulerian (i.e., solution in fixed positions) and Lagrangian (i.e., solution along the streamline) models, respectively (He and Zhao, 2016). Correspondingly, with regard to the coupling of the fluids and particles, computational fluid dynamics (CFD) provides two kinds of framework: Eulerian-Eulerian (E-E) models (Chan et al., 2018; Patel et al., 2017) and Eulerian-Lagrangian (E-L) models (Sommerfeld, 2001; Vié et al., 2016; Zhao et al., 2018), referring to whether the dispersed phase is solved by Eulerian method or Lagrangian method. In Eulerian-Eulerian (E-E) framework, the dispersed phase is considered to be continuous and

solved by transport equation (Hu and Celik, 2008). In Eulerian-Lagrangian (E-L) framework, the dispersed particle phase is simulated by large numbers of discrete particles and the motion and dynamic behaviors are governed by the forces exerted by the continuous phase. A simple illustration of E-L solution for gas-droplet flow system is shown in Figure 2.11.

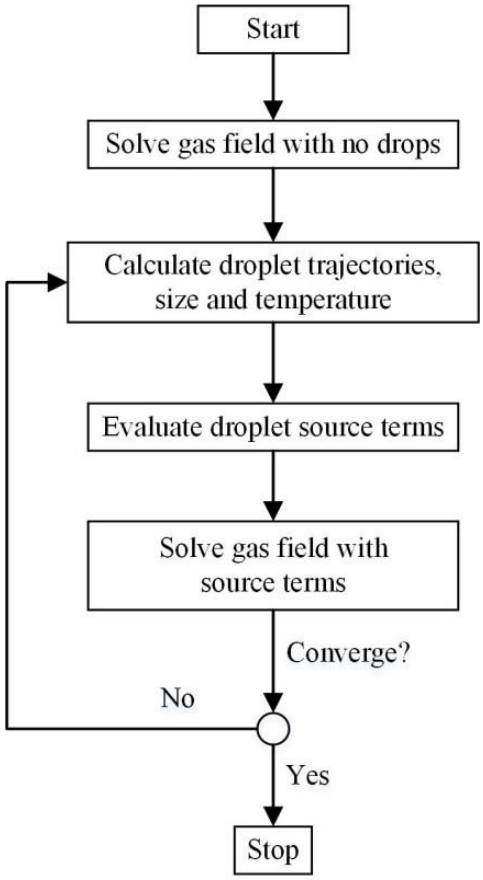

Figure 2.11 An Eulerian-Lagrangian solution of gas-droplet flow (Crowe et al., 1977).

Chiesa et al. (2005) applied both E-E and E-L methods in the study of fluidized bed to predict the formation of bubbles in the bed and the numerical results were validated through experimental data. Zhang and Chen (2007) used both E-E and E-L methods in predicting the particle number density distributions in a ventilated chamber, both steady-state and transient flows are observed and compared.

It is found that the Lagrangian method is more computationally demanding, on the other hand, it performed better in unsteady state condition. Vie et al. (2016) assessed the ability of Eulerian moment methods in addressing two sources of errors (i.e., the statistical convergence and the numerical resolution) in E-E methods, and compared the results to the corresponding Lagrangian method in thermal particle-fluid turbulent flows. Patel et al. (2017) presented and compared three numerical methods in the simulation of two different particle-fluid flows, including a traditional two-fluid model, a quadrature-based moment method and an E-L method. Kazemi et al. (2018) used E-L to study the effect of four dispersion models (i.e., ELT, Sommerfeld's, MOB and PDF) on particle distributions and found that dispersion is the most important mechanism for particles migrating to the corner recirculation zone of the computational domain.

Furthermore, the volume fraction of the dispersed particles and the coupling strategy between the carrier flows and the particles also have large effects on the particle concentration distribution (Yang and Shy, 2005). The particle volume fraction, φ_v is defined as the total volume of particles in unit volume (Almohammed, 2018). When φ_v is relatively small (i.e., $\varphi_v < 10^{-6}$), the particles do not affect the flow field structure of carrier gas remarkably and the effect of particles on the continuous phase can be ignored. Thus one-way coupling method is preferred, which means the continuous phase affects the motion of particles, while not the other way around. With the increasing of particle loading (i.e., $10^{-6} < \varphi_v < 10^{-3}$), the two-way coupling method is recommended where the gas phase affects the motion and behavior of particles, and the particles also affect the structure of the fluid flow. When φ_v continues to increase, the four-way coupling method should be

considered and the interaction effect between particles (e.g., particle-particle collision) should also be calculated (Battista et al., 2018; Elghobashi, 1994; He et al., 2015; Samuel et al., 2016).

Strömgren et al. (2012) developed an Eulerian two-phase model to investigate the two-way coupling effects on particle preferential concentration in particle-gas turbulent flow, and concluded that two-way coupling effects should be considered at a volume fraction of 10^{-4}. Horwitz and Mani (2016) developed a correction method to predict the undisturbed fluid flow velocity by adding an estimation of the velocity disturbance induced by particles in particle-fluid flows considering two-way coupling. Recently, Ireland and Desjardins (2017) have introduced a simple approach to predict the particle drags for two-way and four-way coupled particle-laden fluid flows, and first proposed the grid-independent predictions of the particle drag force in low Reynolds number flows. Li et al. (2018; 2017) have used two-way coupled E-L method to study the solid particle statistics in a developing turbulent boundary layer of the particle-laden flow over a flat plate, and found that the levels of velocity fluctuations of particles in different directions (wall-normal, spanwise and streamwise directions) vary. Dizaji and Marshall (2017) have examined the two-way coupling effects on turbulent particle agglomeration and the attenuation effect of particles on the turbulent kinetic energy in a range of particle Stokes numbers. Battista et al. (2018) have studied the influence of particle Stokes number on the turbulence modulation induced by particles in two-way coupling regime.

2.5.3 Multiphase flow studies

The phenomenon of particles dispersed in turbulent flows is quite common in a broad range of applications, including atmospheric dispersion of pollutants (Chan et al., 2010; Zhong et al., 2018), fluidized beds (Ayeni et al., 2016; Clarke et al., 2018; Xu et al., 2000), soot particles in combustion chambers (Lucchesi et al., 2017; Zhao et al., 2018; Zucca et al., 2006), indoor airborne particles emitted in cooking process (Lai and Chen, 2015; Wang et al., 2018) and so on. Because particles released from all kinds of sources (automobiles, chimneys, factories, etc.) will disperse in the air and severely affect the atmospheric environment and human health, particle-laden turbulent flow is a popular topic of interest. Figure 2.12 shows a contour plot of the time evolution of solid phase volume fraction in a two-dimensional gas-solid fluidized bed reactor (Taghipour et al., 2005).

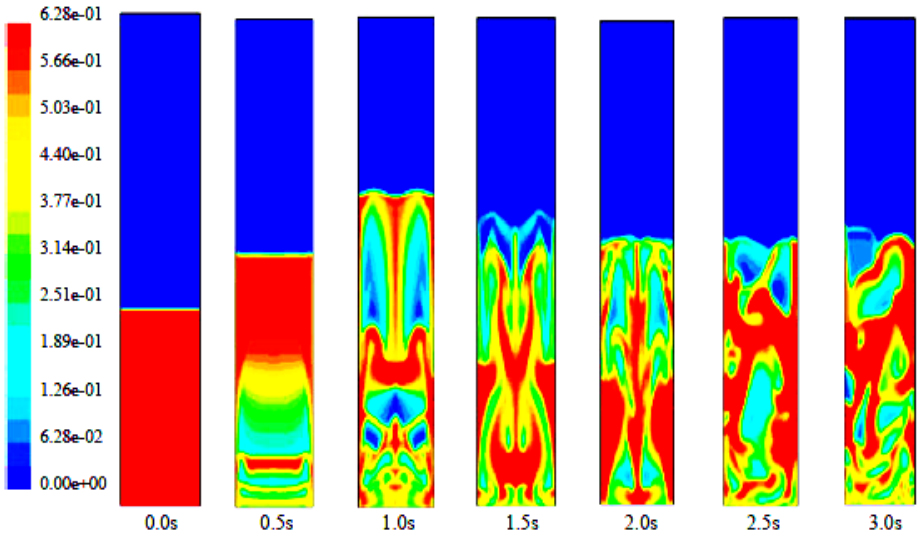

Figure 2.12 Solid phase volume fraction profiles of a 2D bed (U =0.38 m/s, i.e., ~ $6U_{mf}$, drag function: Syamlal–O'Brien, e_{ss} =0.9) (Taghipour et al., 2005).

Many investigators have attempted to identify the factors influencing the dispersion patterns, dynamic behaviors and interaction effects of dispersed particles

in gas flows. Previous studies show that many factors may affect the dispersion pattern of particles in turbulent flows (Zhou et al., 2015), for example, the Reynolds number, Stokes number, the particle density and particle size, etc. especially the particle Stokes number, which describes the response of particles dispersed in fluid flows. Figure 2.13 shows the dynamic behavior of particles suspended in turbulent flows with different Stokes number (Almohammed, 2018; Crowe et al., 1988). Recently, Wang et al. (2017) have studied the influences of Stokes number on the distribution of solid particles in a plane turbulent wall jet using direct numerical simulation. Lau and Nathan (2014) experimentally examined the influence of Stokes number on the particle number density distribution and on the fluid flow velocity field at the exit of a pipe. Samuel et al. (2016) used the lattice-Boltzmann method to conduct simulations on particle-laden flows in a channel and found that particles with different Stokes numbers exhibit quite different behaviors. Lee and Lee (2015) investigated the influences of particle Stokes number on continuous flow field and the turbulence intensity. Hogan et al. (2010) and Yang and Shy (2005) investigated the dependence of particle preferential concentration on Stokes number and Taylor microscale Reynolds number in turbulent flows. Ouchene et al. (2015) explored the influence of particle Reynolds number on the drag coefficient of ellipsoidal solid particles. Mando and Rosendahl (2010) summarized the particle motion regimes in different particle Reynolds numbers. Ireland et al. (2016a and 2016b) studied the influences of both Stokes number and Taylor microscale Reynolds number on the statistical behaviors of inertial solid particles in isotropic and homogeneous turbulent flows for the conditions with or without gravitational effects. Recently, Li et al. (2017) have studied the Stokes number effect on the particle velocity fluctuations and found that the fluctuations decrease with particle Stokes number.

Li et al. (2018) have further studied the interactions between particles and fluid by solving the disturbance flow of particles using Stokes approximation or Oseen correction based on the particle Reynolds number. Dou et al. (2018, 2016) have experimentally studied the effect of Reynolds number and Stokes number on particle-pair relative velocity in homogeneous and isotropic turbulent flows for the first time. Zhao et al. (2018) have studied the influence of Reynolds number and Stokes number on particle resuspension in turbulent duct flow using a LES-Lagrangian method. They have found that particle resuspension tends to occur nearby the centre or the sidewalls of the duct, and the particle resuspension rate and resuspension velocity increase with the Reynolds number.

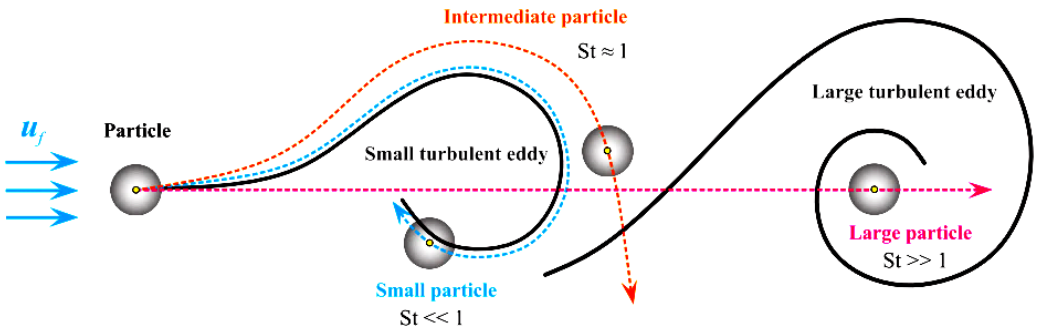

Figure 2.13 Effect of particle Stokes number on the dynamic behavior of particles suspended in turbulent flows (Crowe et al., 1988).

Most of the previous studies focused on particle-laden flows in simplified configurations, such as channels (Klinkenberg et al., 2013; Kuerten, 2006), pipe jets (Lau and Nathan, 2014; Liu and Chan, 2017), or cubic ducts (He and Zhao, 2016; Winkler et al., 2004). However, in some realistic geometry, the irregular structure of the fluid flow channel may induce large inhomogeneity in the flow field, which will further affect the concentration distribution of the dispersed particles. Focusing on inhomogeneous flows, Vincont et al. (2000) conducted experiments in both water

channel and wind tunnel where particles are released from the line source slot into the near-wake flow behind a square rod obstacle, in order to observe the properties of the preferential concentration fields of particles. Based on their experimental study, Rossi and Iaccarino (2009) further studied the capabilities and limitations of standard gradient–diffusion hypothesis (SGDH) in predicting the atmospheric dispersion of the scalar flux for both air and water setup. Grigoriadis and Kassinos (2009) studied the effects of Stokes number on the dispersion characteristics and the preferential concentration effects of the particles in water flows with Stokes number in the range of 0~25 where one-way coupling is considered for the particle-fluid interactions. Huang and Chan (2012) and Huang et al. (2009) experimentally studied the exhaust scalar dispersion and distribution fields in the wake region of a vehicle. Njobuenwu et al. (2013) studied dilute particle-laden flow in square duct with a 90° bend in high Reynolds flows using Eulerian-Lagrangian method. Akbarzadeh and Hrymak (2016) studied the particle-laden flows in rectangular duct bend geometry with a moving wall in very low Reynolds flows using computational fluid dynamics based discrete element method (CFD-DEM). Liu et al. (2016) studied the hemispherical roughness elements on the wall in a developing turbulent boundary layer flow to observe the influence of wall roughness on the particle-induced turbulence modulation.

2.5.4 Aerosol dynamic studies in turbulent flows

Many aerosol simulation codes embedded in CFD have been reported by previous publications. Correspondingly, the mentioned sectional method, the moment method and the Monte Carlo method have been coupled with the kinetics and fluid dynamics computations through different methods, respectively

(Akroyd et al., 2011; Brown et al., 2006; Chan et al., 2018a; Gao et al., 2016; Pyykönen and Jokiniemi, 2000; Zhang and You, 2015).

Since the modelling of the aerosol dynamics in the deterministic methods is to effectively and efficiently solve the differential equations describing the particle population balance, the aerosol dynamics can be included in the CFD as source terms, so both of the fluid flow and aerosol dynamics can be solved in an Eulerian approach. Miller and Garrick (2004) studied the coagulation behaviors of nanoparticles in a turbulent planar jet by coupling direct numerical simulation and a sectional method, and the effects of large vortices are considered. Marchisio et al. (2003) implemented the quadrature method of moments (QMOM) into commercial software FLUENT for studying particle aggregation and breakage processes. Nere and Ramkrishna (2006) investigated pure aggregation process in turbulent pipe flows and examined the particle size distribution in both axial and radial directions. Zou et al. (2010) developed a computational technique linking QMOM with Monte-Carlo for aerosol coagulation and sintering processes. Lin et al. (2016) used their proposed Taylor expansion method of moments (TEMOM) to study the nanoparticle coagulation in turbulent flows by considering the effects of convection, Brownian and turbulent diffusion, turbulent and fluctuating coagulation, and the numerical results proved to agree with the experimental results. Vlieghe et al. (2016) experimentally and numerically studied the agglomeration and breakage of particles in turbulent flows using a QMOM to predict the moments of particles by including the fractal dimension. Recently, Dizaji and Marshall (2017) have coupled the direct numerical computation and the discrete-element method to study the effect of particle agglomeration on the fluid turbulence and the structure of the flow field, and have

compared the difference between one-way and two-way couplings. Frederix et al. (2017) have developed a characteristics-based sectional method for describing aerosol formation and transportation in spatially varying flows. Zheng et al. (2018) have studied the impacts of different particle aggregation kernels on ash particle aggregation processes in turbulent flows based on a CFD-QMOM method and have also proposed a corrected turbulent aggregation model.

However, as for the MC method, because the aerosol dynamics is modelled by Lagrangian method, which is different from the Eulerian method of fluid flow solution, so the coupling of MC method with CFD is relatively more complicated and difficult. Moreover, due to the large number of particles that is needed by MC method to provide the statistical information of the aerosols (Zhao and Zheng, 2013), the computational cost is too much. However, with the rapid development of computer technologies, computers with more memory space and that operate at faster speeds are being developed, and the computational costs (i.e., memory and time consumption) of MC methods are thus no longer a major issue.

Rigopoulos (2007) solved the closure problem of the source term of population balance equation (PBE) by a Lagrangian particle method-based probability density function (PDF) approach. He applied this method in a partially stirred aerosol reactor to study the significance of the interactions of turbulence with chemistry-particle formation mechanisms. Garmory and Mastorakos (2008) used the stochastic fields method to study the aerosol nucleation and growth phenomenon in turbulent jets. Zhou et al. (2014) and (2016) investigated the formation and evolution of aerosol in turbulent mixing layer using both DNS and Monte Carlo method. Hao et al. (2013) simulated the process of titania nanoparticle synthesis by

considering the effects of nucleation, agglomeration, and sintering by a fast PBE-Monte Carlo method. Recently, Pesmazoglou and Kempf (2017) and Pesmazoglou et al. (2016) have proposed a multi-collision Monte Carlo method in which one simulated particle may collide with several simulated particles simultaneously and successfully coupled this algorithm into gas flows, and have investigated the particle aggregation in turbulent jets by using large eddy simulation. Zhao and Zheng (2013) investigated the spatiotemporal evolution of particle size distribution using a coupled CFD and Monte Carlo method, which presented the advantages of Monte Carlo methods. The differentially weighted Monte Carlo was coupled into CFD to study the interactions of aerosol particles and hydrodynamics. However, only a limiting case had been studied for very high-inertia particles whose behaviors are not affected by surrounding fluids. Thus, this method needs further development for wider application.

2.6 Summary of Literature Review

As in many of industrial and engineering applications, the study of complex aerosol dynamics is essentially required and the development of numerical methods for complex particle-fluid systems is of importance.

Among different numerical methods of simulating complex aerosol dynamics, the Monte Carlo method is more preferred by researchers. However, one disadvantage of traditional MC methods is related to the conflicts between the computational accuracy and efficiency due to their stochastic and statistical characteristics. Hence, the accuracy and efficiency of MC methods are needed to be improved significantly. The coupling between Monte Carlo method and turbulent

flow still encounters many technical difficulties. In addition, the relationship between turbulence, particle properties and collision kernels of aerosol dynamics is not yet well understood due to the theoretical limitations and experimental difficulties. Therefore, the present study is based on Monte Carlo method to improve its computational accuracy and efficiency in simulating complex aerosol dynamics.

The fundamental concepts, knowledge and methods of aerosol dynamics in multiphase flows are reviewed in this chapter to shed light on the development and state-of-the-art that the researchers have acquired as well as the knowledge gap for this important research area.

The literature review is summarized as follows:

1. Aerosol dynamics are very important processes for atmospheric aerosols and aerosol-related reactors that are related to several natural and engineering applications, such as those of acid rain formation and precipitation, soot formation and growth in combustion chambers, nanoparticle synthesis in applications of drug delivery and ceramics, among others. It is of great importance to gain a better insight and more intrinsic understanding on aerosol particles including the generating and evolution mechanisms and other physiochemical properties.

2. In many areas, particles often consist of multiple components, and the particle size and compositional distributions affect the properties of particles. Many properties of particles, such as light scattering, radioactivity and capturing strategies are highly dependent on the particle size and

compositional distributions. Therefore, it is very important to study the multi-component properties of aerosols.

3. Numerical methods for aerosol dynamics can be divided into two categories (i.e., deterministic and stochastic methods). Deterministic methods provide an efficient and accurate approach for the numerical simulation of aerosol dynamics. However, the inherent limitations of deterministic methods are also very obvious and difficult to overcome, among which the inability to provide historical information of particles and difficulty to apply to multi-component problems are fatal in the study of complex aerosol dynamics. Stochastic Monte Carlo methods have unique advantages in dealing with multi-component and multi-dimensional problems concerning aerosol dynamics and can provide the historical information and arbitrary number of variables.

4. Various modifications have been made to increase the computational efficiency and guarantee the computational accuracy of Monte Carlo methods, such as weighted Monte Carlo methods and operator splitting Monte Carlo methods.

5. Eulerian-Lagrangian simulation is also quite an efficient tool to study fluid-particle multiphase flows. Factors influencing the dispersion patterns, dynamic behaviors and interaction effects of particles dispersed in turbulent flows include the Stokes number, Reynolds number, particle volume fraction, etc.

6. In order to solve multi-dimensional problems involving aerosol dynamic processes, Monte Carlo method can be coupled to CFD involving aerosol dynamic processes.

Chapter 3 Theoretical Fundamentals of the Present Study

3.1 Introduction

This chapter briefly presents the theoretical fundamentals related to the present study including the population balance equation, Monte Carlo methods, and Navier–Stokes (N-S) equations for turbulent flows.

3.2 Population Balance Equation

3.2.1 Single-component general dynamic equation

In the past several decades, many researchers in aerosol science have introduced all kinds of ideas and concepts to describe the behavior of aerosol particles. The dynamic behaviors and the properties of the aerosol particles are usually depicted by a population balance equation (PBE) (Housiadas and Drossinos, 2005b), which is also known as the general dynamic equation (GDE) (Friedlander, 2000), as expressed in Equation (3-1),

$$\frac{\partial n}{\partial t}+\nabla\cdot n\vec{u}=\nabla\cdot D\nabla n+\left[\frac{\partial n}{\partial t}\right]_{\mathrm{nucl}}+\left[\frac{\partial n}{\partial t}\right]_{\mathrm{coag}}+\left[\frac{\partial n}{\partial t}\right]_{\mathrm{cond}} \tag{3-1}$$

where n is the particle number density function, $\vec{u}$ is the velocity of the gas, and D is the diffusion coefficient.

The second term on the left side and the first term on the right side of Equation (3-1) describe the convection of aerosol in the flow field and the diffusion of the aerosol particles, respectively. The aerosol dynamic processes on the right side of Equation (3-1) refer to the interactions among molecules and particles, including nucleation, surface growth, and coagulation (Zhou et al., 2014b).

Nucleation is a new aerosol formation process, more specifically, means tens or hundreds of molecules forming a stable critical-size nucleus (Zhou and Chan, 2016). Surface growth usually means condensation that describes interactions between gas phase molecules and aerosol particles, is the reverse of evaporation. Coagulation is the process that two particles collide with one another and combine together to form a larger particle (Wexler et al., 1994; Zhou et al., 2014b).

If the effects of convection and diffusion of the aerosols are not considered, Equation (3-1) becomes,

$$\frac{\partial n}{\partial t}=\frac{1}{2}\int_0^v K(v\text{-}\tilde{v},\tilde{v})n(\tilde{v})n(v-\tilde{v})\mathrm{d}\tilde{v}-\int_0^\infty K(v,\tilde{v})n(v)n(\tilde{v})d\tilde{v}+\frac{\partial(I_0 n)}{\partial v}(v,t)+\delta(v_0,v)J_0(t) \tag{3-2}$$

where $J_0(t)$, $K(v,\tilde{v})$, and $I_0(v,t)$ are the nucleation, coagulation and condensation kernels, respectively (Debry et al., 2003), and $\delta(v_0,v)$ is the standard Dirac function, $\delta(v_0,v)=0,\ (v\neq v_0)$.

3.2.2 Two-component general dynamic equation

In many areas of natural science and engineering applications, particles often consist of multiple components, and the particle size and compositional distributions affect the properties of particles. For atmospheric aerosols, coagulation and condensation are the most important processes. Many of the properties of aerosols (e.g., light scattering, radioactivity and capturing strategies) are dependent on the size and compositional distributions of particles. Furthermore, coagulation and condensation processes are very important phenomena to the evolution of particle sizes and compositional distributions (Fu et al., 2015; Ramabhadran et al., 1976; Singh et al., 2018; Zhao et al., 2005b). Therefore, these two processes have been

widely studied for the evolution of the particle size and compositional distributions.

For a two-component aerosol system that only considers coagulation and condensation processes, the governing equation becomes (Gelbard and Seinfeld, 1978; Zhao and Zheng, 2011),

$$\begin{aligned}\frac{\partial n(v_{\mathrm{A}},v_{\mathrm{B}},t)}{\partial t}=&\\ \frac{1}{2}\int_0^{v_{\mathrm{A}}}\int_0^{v_{\mathrm{B}}} K(v_{\mathrm{A}}-v_{\mathrm{A}}^{'},v_{\mathrm{B}}-v_{\mathrm{B}}^{'},v_{\mathrm{A}}^{'},v_{\mathrm{B}}^{'},t)\,n(v_{\mathrm{A}}-v_{\mathrm{A}}^{'},v_{\mathrm{B}}-v_{\mathrm{B}}^{'},t)n(v_{\mathrm{A}}^{'},v_{\mathrm{B}}^{'},t)\mathrm{d}v_{\mathrm{A}}^{'}\mathrm{d}v_{\mathrm{B}}^{'}&\\ -n(v_{\mathrm{A}},v_{\mathrm{B}},t)\int_0^{\infty}\int_0^{\infty} K(v_{\mathrm{A}},v_{\mathrm{B}},v_{\mathrm{A}}^{'},v_{\mathrm{B}}^{'},t)n(v_{\mathrm{A}}^{'},v_{\mathrm{B}}^{'},t)\mathrm{d}v_{\mathrm{A}}^{'}\mathrm{d}v_{\mathrm{B}}^{'}&\\ -\frac{\partial(I_{\mathrm{A}}n)}{\partial v_{\mathrm{A}}}(v_{\mathrm{A}},v_{\mathrm{B}},t)-\frac{\partial(I_{\mathrm{B}}n)}{\partial v_{\mathrm{B}}}(v_{\mathrm{A}},v_{\mathrm{B}},t)&\end{aligned} \tag{3-3}$$

where v_{A} and v_{B} are the volume of A-component and B-component within a particle with a total volume of $v_{\mathrm{A}}+v_{\mathrm{B}}$, respectively; $n(v_{\mathrm{A}},v_{\mathrm{B}},t)$ is the number density function of particles with a volume of $v_{\mathrm{A}}+v_{\mathrm{B}}$ at time t such that $n(v_{\mathrm{A}},v_{\mathrm{B}},t)\mathrm{d}v_{\mathrm{A}}\mathrm{d}v_{\mathrm{B}}$ denotes the number density of particles in the size range of A-component v_{A} to $v_{\mathrm{A}}+\mathrm{d}v_{\mathrm{A}}$, and the size range of B-component v_{B} to $v_{\mathrm{B}}+\mathrm{d}v_{\mathrm{B}}$; $K(v_{\mathrm{A}},v_{\mathrm{B}},v_{\mathrm{A}}^{'},v_{\mathrm{B}}^{'},t)$ is the coagulation kernel between one particle of volume $(v_{\mathrm{A}},v_{\mathrm{B}})$ and another particle of volume $(v_{\mathrm{A}}^{'},v_{\mathrm{B}}^{'})$. The coagulation of two particles results in the production of a new two-component particle with a volume of $(v_{\mathrm{A}}+v_{\mathrm{A}}^{'}, v_{\mathrm{B}}+v_{\mathrm{B}}^{'})$ and the destruction of two previous particles. I_{A} and I_{B} are the condensation rate coefficients of the A-component and B-component, respectively. The occurrence of a condensation event either in the A-component or the B-component would vary (either increase or decrease depending on the derivative of the condensation rate with particle volume) the number density of particles of state $(v_{\mathrm{A}}, v_{\mathrm{B}})$ as expressed in Equation (3-3).

3.2.3 Aerosol dynamics kernels

Nucleation process refers to the process that the saturated vapours convert into particles of a critical size, v_0. The nucleation kernel, $J_0(t)$ describes the rate of formation of particles with volume, v_0. Thus the number density of other particles (volume larger than v_0) does not change due to the nucleation process.

The homogeneous nucleation rate is typically written as (Seinfeld, 1998):

$$J_0(t)=C\exp(-\Delta G^*/k_B T) \tag{3-4}$$

where C is a normalized constant that is connected with the vapor pressure, ΔG^* is the Gibbs free energy in the equilibrium state that is needed to form a stable nucleus.

Coagulation process refers to two particles collide and combine with each other to form a new larger particle, it is described by the famous Smoluchowski's equation (Liffman, 1992), which includes the first two terms in right-hand side of Equation (3-2). The coagulation kernel, $K(v,\tilde{v})$ describes the rate of particles with volume, v coagulating with particles with volume, $\tilde{v}$. In different aerosol regimes, $K(v,\tilde{v})$ can be a constant value or a value that is dependent on the volume of particles.

For the free molecule regime (where the diameter of particles is smaller than the mean free path of air), $K(v,\tilde{v})$ is expressed as Equation (3-5),

$$K(v,\tilde{v}) = \left(\frac{6}{\pi}\right)^{2/3}\left(\frac{\pi k_B T}{2\rho_p}\right)^{1/2}\left(\frac{1}{v}+\frac{1}{\tilde{v}}\right)^{1/2}\left(v^{1/3}+\tilde{v}^{1/3}\right)^2 \tag{3-5}$$

In continuous regime, $K(v,\tilde{v})$ can be expressed as,

$$K(v,\tilde{v}) = \left(\frac{2k_B T}{3\mu}\right)\left(2+\left(\frac{v}{\tilde{v}}\right)^{1/3} + \left(\frac{\tilde{v}}{v}\right)^{1/3}\right) \tag{3-6}$$

where k_B is the Boltzmann's constant, ρ_p is the density of particles and μ is the viscosity of air (Grant et al., 2001).

Condensation process is the reverse process of evaporation, and the condensation rate, $I_0(v,t)$ is usually related to the surface area of the particles. Theoretically, the size of all of the particles will change due to condensation process.

The occurrence of condensation or evaporation event depends on the vapor pressure far from the particle, p^{∞} and the equilibrium vapor pressure, p^{eq}. When Equation (3-7) is satisfied, an effective condensation event will occur and the condensation kernel in continuous regime can be described as Equation (3-8) (Debry et al., 2003).

$$p^{\infty} \geq p^{eq} \tag{3-7}$$

$$I_0(v,t) = C_I \exp(p^{\infty} - p^{eq}) v^{1/3} \tag{3-8}$$

where C_I is a constant that is connected with the diffusion process and material properties of species and temperature.

3.3 Differentially Weighted Monte Carlo Methods

The differentially weighted Monte Carlo (DWMC) method developed by Zhao et al. (2010) is used herein. In this method, every simulated particle for calculation is weighted differentially with a number of real particles, which is the weight of the simulated particle, w_i (i = 0, 1, 2, 3 ... n), where n is the simulated particle number.

This DWMC method is prominent for managing the coagulation process. The occurrence probability of coagulation, P_i on simulated particle, i within δt and V_s is,

$$P_{\mathrm{i}} = 1\text{-}\exp(-V_s C_i \delta t/2) \tag{3-9}$$

where V_s is the volume of the simulation system, δt is one time-step, and C_i is the coagulation rate of simulated particle, i based on the probabilistic coagulation rule, and is described as,

$$C_i = \frac{1}{V_s{}^2} \sum_{j=1, j\neq \mathrm{i}}^{N} K_{ij}^{'} \tag{3-10}$$

where N is the total number of the simulated particles, and $K_{ij}^{'}$ is the normalized coagulation kernel for particle, i and particle, j ,

$$K_{ij}^{'} = 2K_{ij} w_j \max(w_i, w_j)/(w_i + w_j) \tag{3-11}$$

Coagulation event will take place on simulated particle, i if a generated random number from a uniform distribution between 0 and 1, r_1 is less than P_i; the choice of its coagulation pair particle, j is based on the acceptance-rejection method. The coagulation partner particle, j is determined if the following condition is satisfied,

$$r_2 \leq K_{ij}^{'} / \max(K_{mn}^{'})|_{\forall m, \forall n} \tag{3-12}$$

where r_2 is a generated random number. Equation (3-12) is checked until a particle j is chosen.

When two simulated particles, i and j, are selected to coagulate with each other, the previous particles are substituted by two new weighted simulated particles,

which are also denoted as *i* and *j*, while the properties of these particles are changed. The calculations are formulated as the following equations (Zhao et al., 2010; Zhao and Kruis, 2014):

$$\text{if } w_i = w_j, \begin{cases} w_i^{'} = w_i/2 \; ; \; v_i^{'} = v_i + v_j \; ; \\ w_j^{'} = w_j/2 \; ; \; v_j^{'} = v_i + v_j \; ; \end{cases} \tag{3-13a}$$

if

$$w_i \neq w_j, \begin{cases} w_i^{'} = \max(w_i, w_j) - \min(w_i, w_j) \; ; \; v_i^{'} = v_m|_{w_m = \max(w_i, w_j)} \; ; \\ w_j^{'} = \min(w_i, w_j) \; ; \; v_j^{'} = v_i + v_j \; ; \end{cases} \tag{3-13b}$$

where $w_i^{'}$, $w_j^{'}$, $v_i^{'}$ and $v_j^{'}$ represent the weight or the volume of the newly created simulated particles, *i* and *j* after the coagulation event.

3.4 Operator Splitting Technique

3.4.1 Overview

Considering the general dynamic equation (GDE) in Equation (3-1), this equation contains convective, diffusion, nucleation, growth and coagulation terms. These different terms reflect different physical and chemical aspects of the model which appear in the same equation, and make it rather difficult to analyze and solve both analytically and numerically.

An applicable strategy to deal with such complicated problems is to “divide and conquer”. A rather successful approach in this spirit is an operator splitting technique. Operator splitting technique can separate the total process into multiple steps. It firstly solves different sub-processes and then combines the results (Carichino et al., 2018; Carrayrou et al., 2004; McLachlan and Quispel, 2002), respectively.

3.4.2 Implementation of operator splitting technique

Splitting methods generally stand out when an operator or equation can be split into several parts that are much easier to solve, and then composed to form the integrator. Consider a simple time-dependent differential equation, $\mathrm{d}x/\mathrm{d}t = X(x)$, within phase space, *M* and *X* is a vector field on *M*. Three steps are involved to implement the splitting methods (Mclachlan and Quispel, 2002):

(a) Selecting a set of vector fields X_i such that $X = \sum(X_i)$;

(b) Integrating each X_i ; and

(c) Combining these solutions to yield an integrator for *X*.

Then the operator splitting method can be described as,

$$\exp(\triangle tX) = \exp(\triangle tX_\mathrm{d})\exp(\triangle tX_\mathrm{s}) + \mathcal{O}(\triangle t^2) \quad (3\text{-}14a)$$

$$= \exp(1/2\triangle tX_\mathrm{d})\exp(\triangle tX_\mathrm{s})\exp(1/2\triangle tX_\mathrm{d}) + \mathcal{O}(\triangle t^3) \quad (3\text{-}14b)$$

$$= \exp(1/2\triangle tX_\mathrm{s})\exp(\triangle tX_\mathrm{d})\exp(1/2\triangle tX_\mathrm{s}) + \mathcal{O}(\triangle t^3) \quad (3\text{-}14c)$$

where *X* refers to the total process, X_d and X_s refer to two different sub-processes (i.e., deterministic and stochastic processes) respectively and $\triangle t$ refers to one time-step.

Equation (3-14a) is of first-order accuracy while Equations (3-14b) and (3-14c) are of second-order accuracy (Liu and Chan, 2017a; Zhou et al., 2014b). The operator splitting schemes are shown as Figure 3.1.

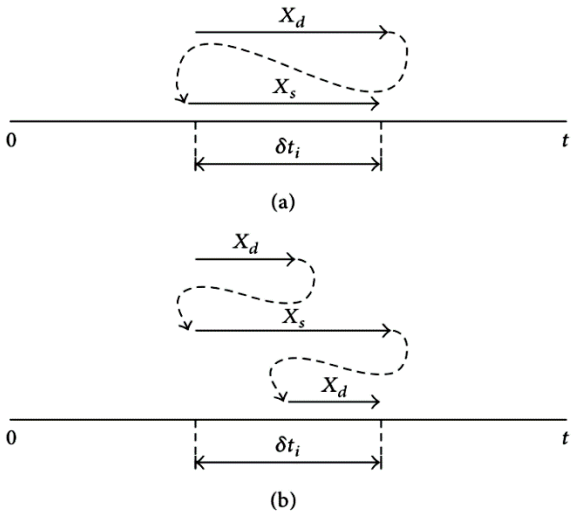

Figure 3.1 Operator splitting schemes. (a) First order Lie scheme; (b) second order Strang scheme (Zhou et al., 2014b).

Zhou et al. (2014) and Zhou and Chan (2016) used operator splitting technique to solve the GDE, and the flowchart of operator splitting Monte Carlo method for solving GDE is shown in Figure 2.7. By dealing with the split processes one by one and making further approximations which neglect the diffusion and convection terms under certain conditions, the GDE including deterministic processes (nucleation, surface growth) and stochastic process (coagulation) can be solved efficiently (Patterson et al., 2006).

In the present study, the second-order Strang splitting method is used which is described by the Equation (3-14b). In the present study, X refers to the total aerosol dynamic process, X_s refers to coagulation process which is modelled by the stochastic method, X_d refers to nucleation and condensation processes which are solved by deterministic integration method. As X_d includes two processes (i.e., nucleation and condensation processes), Equation (3-14b) becomes,

$$\exp(\delta tX) = \exp\left(\frac{1}{2}\delta tX_{\text{nucl}}\right)\ \exp\left(\frac{1}{2}\delta tX_{\text{cond}}\right)\exp\left(\delta tX_{\text{coag}}\right)\exp\left(\frac{1}{2}\delta tX_{\text{cond}}\right)\exp\left(\frac{1}{2}\delta tX_{\text{nucl}}\right) + \mathcal{O}\left(\delta t^3\right) \tag{3-15}$$

3.5 Sectional Method

In the present study, a sectional method (SM) is used to verify the proposed MC method, and the algorithm of SM is briefly described in the following.

The sectional method used was developed by Prakash et al. (2003) based on the former sectional method developed by Gelbard et al. (1980) and the coagulation nodal method developed by Lehtinen and Zachariah (2001). In this sectional method, particles only exit at discretized nodes. By limiting the number of the particle parameters, this model makes the computational work quite simple and time-saving.

Specifically, the GDE at node *k* is given by,

$$\frac{\partial n_k}{\partial t} = \left[\frac{\partial n_k}{\partial t}\right]_{\text{nuc1}} + \left[\frac{\partial n_k}{\partial t}\right]_{\text{coag}} + \left[\frac{\partial n_k}{\partial t}\right]_{\text{cond}} \tag{3-16}$$

The population change due to nucleation, coagulation and condensation are respectively given by,

$$\left[\frac{\partial n_k}{\partial t}\right]_{\text{nuc1}} = \xi_k J_k(t) \tag{3-17}$$

$$\left[\frac{\partial n_k}{\partial t}\right]_{\text{coag}} = \frac{1}{2}\sum_{\substack{i=2\\ j=2}} \chi_{ijk} K_{i,j} n_i n_j - n_k \sum_{i=2} K_{i,k}\, n_i \tag{3-18}$$

$$\left[\frac{\partial n_k}{\partial t}\right]_{\text{cond}} = \frac{v_1}{v_k - v_{k\text{-}1}} K_{1,k\text{-}1}(n_1 - n^s_{1,k\text{-}1}) n_{k\text{-}1} - \frac{v_1}{v_{k+1} - v_k} K_{1,k}(n_1 - n^s_{1,k}) n_k \tag{3-19}$$

where ξ_k and χ_{ijk} are expressed as (Prakash et al., 2003; Shigeta and Watanabe, 2010),

$$\xi_k = \begin{cases} \dfrac{v_0}{v_k}; & \text{if } v_{k-1} \le v_0 \le v_k \ , \\ \dfrac{v_0}{v_2}; & \text{if } v_0 \le v_1, \\ 0; & \text{otherwise.} \end{cases}$$

$$\chi_{ijk} = \begin{cases} \dfrac{v_{k+1} - (v_i + v_j)}{v_{k+1} - v_k}; & \text{if } v_k \le v_i + v_j \le v_{k+1} \ , \\ \dfrac{(v_i + v_j) - v_{k-1}}{v_k - v_{k-1}}; & \text{if } v_{k-1} \le v_i + v_j \le v_k \ , \\ 0; & \text{otherwise.} \end{cases}$$

More detailed information about this sectional method can be referred to Prakash et al. (2003).

3.6 Computational Fluid Dynamics (CFD)

3.6.1 Fluid and scalar equations

The fluid flows are governed by the laws of the physical conservation, and the basic conservation equations include conservation laws of mass, momentum and energy. Therefore, CFD is based on the solution of the continuity and Navier–Stokes (N-S) equations. The mass continuity, momentum and species equations can be expressed as (Chan et al., 2010):

$$\frac{\partial \rho}{\partial t} + \frac{\partial (\rho u_i)}{\partial x_i} = 0 \tag{3-20}$$

$$\frac{\partial \rho u_i}{\partial t} + \frac{\partial \rho u_i u_j}{\partial x_j} = -\frac{\partial p}{\partial x_i} + \frac{\partial}{\partial x_j}[\mu(\frac{\partial u_i}{\partial x_j} + \frac{\partial u_j}{\partial x_i})] \tag{3-21}$$

$$\frac{\partial \rho \phi}{\partial t} + \frac{\partial \rho u_i \phi}{\partial x_j} = \frac{\partial}{\partial x_j}(D_s \frac{\partial \phi}{\partial x_j}) + S_\phi \tag{3-22}$$

where ρ is the density, u_i is the velocity, p is the pressure, μ is the kinetic viscosity, ϕ is an arbitrary scalar (i.e., enthalpy, species mass concentration or any variable) governed by the transport equation, D_s is the diffusion coefficient, and S_ϕ is the source term, t and x_j is the time and the coordinate, respectively (Chan et al., 2010).

3.6.2 Numerical simulation approaches

To solve the turbulent N-S equation in Equation (3-21), there are three turbulence models: direct numerical simulation (DNS), large eddy simulation (LES) and Reynolds averaged Navier–Stokes (RANS) approach (Xu et al., 2003).

3.6.2.1 Direct numerical simulation (DNS)

a) Navier-Stokes equations are solved numerically without adopting any turbulence model, so no assumptions or empirical constants are needed;

b) There will be no problem of closure; theoretically all of the turbulent flow problems can be solved by DNS;

c) DNS can give the evolution process (both in time and space) of any instantaneous quantity (e.g. velocity and pressure) in 3D flow fields; and

d) The clear flow structure of turbulence characteristics can be obtained.

However, for practical engineering purposes, DNS is not only too computational costly, but also the details of the numerical simulation are usually not required. So two general engineering approaches to modelling turbulence (i.e., LES and RANS) are still widely used in many scientific and engineering problems.

3.6.2.2 Large eddy simulation (LES)

In LES simulations, the turbulent flows are decomposed into two parts of large- and small-scale structures: the large eddies are directly computed on an Eulerian grid, while the small eddies are modelled (Chan et al., 2008; Luo et al., 2004; Pesmazoglou and Kempf, 2017; Rodrigues et al., 2018). In LES, the Navier-Stokes equation in Equation (3-21) becomes:

$$\frac{\partial \rho \overline{u_i}}{\partial t} + \frac{\partial \rho \overline{u_i}\overline{u_j}}{\partial x_j} = -\frac{\partial \overline{p}}{\partial x_i} + \frac{\partial}{\partial x_j}[\mu\left(\frac{\partial \overline{u_i}}{\partial x_j} + \frac{\partial \overline{u_j}}{\partial x_i}\right) - \tau_{ij}] \tag{3-23}$$

where τ_{ij} refers to the subgrid scale (SGS) stress tensor, representing the motions at scales that are smaller than the filter width; τ_{ij} is written as:

$$\tau_{ij} = \rho(\overline{u_i u_j} - \overline{u_i}\overline{u_j}) \tag{3-24}$$

where τ_{ij} cannot be solved explicitly, therefore it requires to be modelled. The SGS model of Smagorinsky (1963) is often used in the research studies because of its simplicity and low consumption of time and computer memories.

3.6.2.3 Reynolds averaged Navier–Stokes (RANS)

In the RANS approach, the Navier–Stokes equation in Equation (3-21) becomes:

$$\frac{\partial \rho \overline{u_i}}{\partial t} + \frac{\partial \rho \overline{u_i}\overline{u_j}}{\partial x_j} = -\frac{\partial \overline{p}}{\partial x_i} + \frac{\partial}{\partial x_j}[\mu(\frac{\partial \overline{u_i}}{\partial x_j} + \frac{\partial \overline{u_j}}{\partial x_i})] + \frac{\partial}{\partial x_j}(-\rho\overline{u_i' u_j'}) \tag{3-25}$$

where the Reynolds stress $-\rho\overline{u_i' u_j'}$ is introduced in Equation (3-25).

Compared to DNS and LES, RANS requires lower computational accuracy in predicting the turbulent flows and is sensitive to the turbulence model used.

However, the substantially lower computational cost of RANS makes it still quite popular in many engineering applications today (Kardan et al., 2018).

3.7 Summary

The fundamental theories that are used to formulate the proposed CFD-Monte Carlo method are briefly introduced to present a theoretical framework of the methodology in the present study. The basic concepts and assumptions as well as mathematical theories/governing equations i.e., PBE, Monte Carlo methods, operator splitting method, and CFD solutions of turbulent flows are presented so that the methodology used in the present study can be more easily reassembled.

Chapter 4 Monte Carlo Simulation of One-component Aerosol Dynamics

4.1 Introduction

The purpose of this chapter is to propose and develop a new differentially weighted operator splitting Monte Carlo (DWOSMC) method, and demonstrate the ability of describing complex aerosol dynamics of this DWOSMC method.

By using the operator splitting (OS) technique, this DWOSMC method coupled the stochastic Monte Carlo method for calculating coagulation process, and deterministic integration method for calculating nucleation and condensation processes.

In order to prove the computational accuracy and efficiency of this newly developed DWOSMC method, it is firstly verified by analytical solutions for typical cases of simultaneous coagulation and condensation processes, simultaneous nucleation and coagulation processes, and simultaneous nucleation, coagulation and condensation processes accordingly. It is further verified by comparing the simulation results with a sectional method of relatively complex cases of simultaneous coagulation and condensation processes, simultaneous nucleation and coagulation processes, and simultaneous nucleation, coagulation and condensation processes accordingly.

4.2 Numerical Methodology

4.2.1 General dynamic equation

The general dynamic equation that governs the evolution of aerosols is written as Equation (3-1). If the effects of convection and diffusion are not considered, Equation (3-1) becomes,

$$\frac{\partial n}{\partial t} = \left[\frac{\partial n}{\partial t}\right]_{\text{nuc1}} + \left[\frac{\partial n}{\partial t}\right]_{\text{coag}} + \left[\frac{\partial n}{\partial t}\right]_{\text{cond}} \tag{4-1}$$

The treatment of different processes is described in the following sections.

4.2.1.1 Nucleation

Nucleation process refers to the process that the saturated vapours convert into particles of a critical size, v_0. Thus the number density of other particles (i.e., volume is larger than v_0) does not change due to the nucleation process, and the nucleation process contributes to the variation of particle number concentration and the total particle volume fraction due to the production of new particles. The particle number concentration change due to nucleation is (Kalani and Christofides, 2002),

$$\left[\frac{\partial n}{\partial t}\right]_{\text{nuc1}} = \delta_{v_0}(v) J_0(t) \tag{4-2}$$

The nucleation kernel, $J_0(t)$ describes the rate of formation of particles with volume, v_0. The $\delta_{v_0}(v)$ is the standard Dirac function, $\delta_{v_0}(v) = 0,\ (v \neq v_0)$.

In the present study, the critical size of the nucleation process and the initial volume of the particles used is v_0. The nucleated particles are sorted into the weight of the corresponding simulated particle, i which represents the real particles with volume, v_0,

$$w_i^{'} = w_i + J_0(t)\delta t \tag{4-3}$$

where $w_i^{'}$ and w_i are the weight of simulated particle, i after and before the nucleation event, respectively, and δt is one time-step.

4.2.1.2 Coagulation

Coagulation process refers to two particles collide and combine with each other to form a new larger particle. It is described by the famous Smoluchowski's equation including two terms and is expressed as Equation (4-4) (Seigneur et al., 1986; Wei, 2016). The coagulation kernel, $K(v,\tilde{v})$ describes the rate of particles with volume, v coagulating with particles with volume, $\tilde{v}$. In different aerosol regimes, $K(v,\tilde{v})$ can be a constant value or a value that depends on the volume of particles.

$$\left[\frac{\partial n}{\partial t}\right]_{\text{coag}} = \frac{1}{2}\int_0^v K(v-\tilde{v},\tilde{v})n(\tilde{v})n(v-\tilde{v})\mathrm{d}\tilde{v} - \int_0^\infty K(v,\tilde{v})n(v)n(\tilde{v})d\tilde{v} \tag{4-4}$$

The coagulation kernel for the free molecule regime and continuous regime are written as Equations (3-5) and (3-6), respectively.

The treatment of coagulation event in the present study is according to the DWMC method described in Section 3.3.

4.2.1.3 Condensation

Condensation process is the reverse process of evaporation, and the condensation rate, $I_0(v,t)$ is usually related to the surface area of the particles. Theoretically, the total particle number does not change because of the condensation

process; however, the size of all of the particles will be larger. Therefore, the particle size distribution will change because of condensation process.

The change in particle size distribution caused by condensation event (Ramabhadran et al., 1976) is,

$$\left[\frac{\partial n(v,t)}{\partial t}\right]_{\text{cond}} = -\frac{\partial (I_0 n)}{\partial v}(v,t) \tag{4-5}$$

In the treatment of condensation event in the present study, the weights of the simulated particles remain the same, which means that a condensation event does not change the total particle number, whereas the volume of simulated particle *i* changes accordingly as follows:

$$\frac{dv_i}{dt} = I(v) \tag{4-6}$$

where v_i is the volume of simulated particle, *i*.

4.2.2 Differentially weighted operator splitting Monte Carlo method

In the present study, a new differentially weighted operator splitting Monte Carlo (DWOSMC) method is proposed and developed by using operator splitting (OS) technique to combine stochastic and deterministic methods, which makes the calculation more flexible and efficient. In this new DWOSMC method, the stochastic Monte Carlo method is used for calculating the coagulation process, while the deterministic integration method is used for calculating deterministic processes (i.e., nucleation and condensation, etc.).

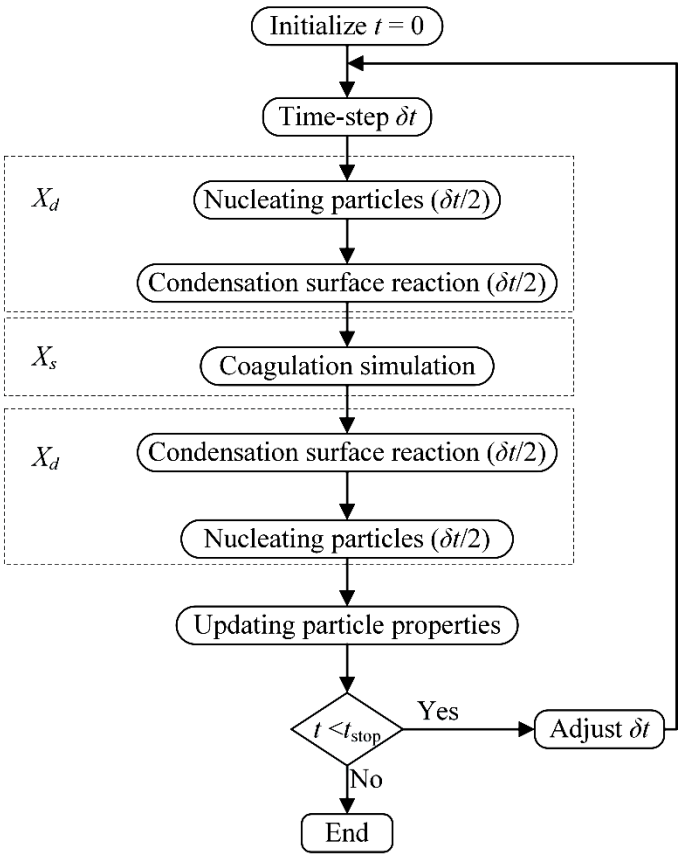

Figure 4.1 Flowchart of DWOSMC algorithm (Liu and Chan, 2016).

Figure 4.1 shows the flowchart of the full algorithm of DWOSMC method. The second order operator splitting in Equation (3-15) is shown. Specifically, the full algorithm is described as follows:

Step 1. Initialization. At the very beginning of the numerical simulation, i.e., when the integration time $t = 0$, the properties (volume, diameter, weight, and number density etc.) of the simulated particles are initialized and stored in arrays.

Step 2. Generating time-step, δt. In the simulation process, the choice of an appropriate time-step is vital. It is expected to be small enough to ensure that the successively happened coagulation events are uncoupled and that the integration of other physical processes is accurate. The time scale for different aerosol dynamic processes can be determined as follows:

(i) Coagulation

For all of the simulated particles in the system, the time-step for the coagulation event should be determined as (Zhao et al., 2010),

$$\Delta t_{\text{coag}} = \min|\forall_i (V_s / \sum_{j=1, j\neq i}^{N} K_{ij}^{'}) \tag{4-7}$$

where V_s is the volume of simulation system, N is the total number of simulated particles, , and $K_{ij}^{'}$ is the normalized coagulation kernel for particle, i and particle, j, where $K_{ij}^{'} = 2K_{ij}w_j\max(w_i,w_j)/(w_i+w_j)$.

(ii) Nucleation

The time-step for the nucleation event should be determined by,

$$\Delta t_{\text{nucl}} = 1/(v_0 J_0(t)) \tag{4-8}$$

where $J_0(t)$ is the nucleation kernel and v_0 is the volume of the newly created particles.

(iii) Condensation

The time-step for the condensation event is determined by Debry et al. (2003) and Liu and Chan (2017a),

$$\Delta t_{\text{cond}} = v_i / I_0(v,t) \tag{4-9}$$

where v_i is the volume of the particle, i and $I_0(v,t)$ is the condensation kernel.

In order to ensure the accuracy of the numerical simulation, the adopted time-step value, δt should be smaller than the minimum value of all the above-mentioned time scales (Debry et al., 2003). δt is calculated as follows:

$$\delta t = \alpha \min(\Delta t_{coag}, \Delta t_{nucl}, \Delta t_{cond}) \quad (4\text{-}10)$$

where α is a constant of 0.01(Xu et al., 2014; Zhao et al., 2009) during the calculation in order to ensure an accurate integration of all aerosol dynamic processes.

Step 3. Handling the aerosol dynamic processes. The second-order Strang splitting method is used herein. For nucleation and condensation processes, splitting the time-step into two parts, the simulation for nucleation and condensation processes is firstly calculated within the first $\delta t/2$, and then the coagulation process is calculated for the time-step, δt. At last, nucleation and condensation processes are then calculated within the second $\delta t/2$. The integration procedure in Equation (3-15) from t^{m-1} to t^m where t is the total calculation time, m is the step number and $t^m = t^{m-1}+\delta t$) as follows:

(i) Integration of nucleation based on Equation (4-2) for a time period of $\delta t/2$;

(ii) Integration of condensation based on Equation (4-6) for a time period of $\delta t/2$;

(iii) Integration of coagulation based on Equations (3-9) to (3-13a) for a time period of δt;

(iv) Integration of condensation based on Equation (4-6) for a time period of $\delta t/2$; and

(v) Integration of nucleation based on Equation (4-2) for a time period of $\delta t/2$;

Step 4. Updating the properties of the simulated particles and obtaining the information of the particles at time, t^m.

Step 5. Repeating Steps 2 to 4 if the accumulated simulation time, t^m is smaller than t_{stop}, otherwise, the current Monte Carlo simulation is completed and the next Monte

Carlo simulation is then started. Eight Monte Carlo repetitions are used and the average results are obtained to reduce the stochastic errors.

4.3 Numerical Setup and Verification

4.3.1 Description of the studied cases

This newly proposed and developed DWOSMC method is verified by both corresponding analytical solutions (Maisels et al., 2004; Palaniswaamy and Loyalka, 2008; Ramabhadran et al., 1976) and a sectional method (Prakash et al., 2003), and three different test problems are considered in the present study, i.e., simultaneous coagulation and condensation processes, simultaneous nucleation and coagulation processes, and simultaneous nucleation, coagulation and condensation processes. For every test problem, the DWOSMC method is initially verified by the corresponding analytical solutions, and then the results obtained from DWOSMC method are compared with the sectional method for more complex studied cases. The studied cases are described in the following Sections 4.3.1.1 to 4.3.1.3.

4.3.1.1 Validation of aerosol dynamic processes with analytical solutions

For typical aerosol dynamics processes, the analytical solutions are available. To initially verify this DWOSMC method, five typical cases with analytical solutions are chosen, i.e. three simultaneous coagulation and condensation processes, one simultaneous nucleation and coagulation processes, and one simultaneous nucleation, coagulation and condensation processes. The parameters, initial conditions and analytical solutions for each studied case are given in Table 4.1.

Table 4.1 Parameters of initial conditions and analytical solutions used for validation cases I to V, where $\tau = t\sqrt{2AJ_0}$, $B = 1/N_0\sqrt{2J_0/A}$, $E = DC_0/AN_0$ and Coag: Coagulation, Cond: Condensation and Nucl: Nucleation (Liu and Chan, 2018a).

Process	Case	Parameter	Analytical solution	Initial conditions
Coag+ Con	I	$K = K_0$ $I = \sigma_1 v$	$N(t) = \frac{N_0}{1 + K_0 N_0 t/2}$ $\emptyset(t) = \emptyset_0[\exp(\sigma_1 t)]$	$K_0 = 5\times10^{-6}(\mathrm{m^3 s^{-1}})$ $\sigma_1 = 2\times10^{-2}\ (\mathrm{s^{-1}})$
	II	$K = K_0$ $I = \sigma_0$	$N(t) = \frac{N_0}{1 + K_0 N_0 t/2}$ $\emptyset(t) = \emptyset_0[1 + \frac{2\sigma_0}{K_0\emptyset_0}\ln(\frac{N_0}{N})]$	$K_0 = 5\times10^{-7}(\mathrm{m^3 s^{-1}})$ $\sigma_0 = 1\times10^{-5}(\mathrm{s^{-1}})$
	III	$K = K_1(u+v)$ $I = \sigma_1 v$	$N(t) = N_0\exp[-\frac{K_1\emptyset_0}{\sigma_1}(\exp(\sigma_1 t)-1)]$ $\emptyset(t) = \emptyset_0[\exp(\sigma_1 t)]$	$K_1 = 1\times10^{17}(\mathrm{s^{-1}})$ $\sigma_1 = 0.5\ (\mathrm{s^{-1}})$
Nucl+ Coag	IV	$K = A$ $J = J_0$	$\frac{N}{N_0} = B\frac{1+B\tan(\tau/2)}{\tanh(\tau/2)+B}$ $\frac{V}{V_0} = 1+\frac{1}{2}B\tau$	$A = 4\times10^{-28}(\mathrm{m^3 s^{-1}})$ $J_0 = 1.91\times10^{28}(\mathrm{s^{-1}})$
Nucl+ Coag+ Cond	V	$K = A$ $J = J_0$ $I = D$	$\frac{N}{N_0} = B\frac{1+B\tan(\tau/2)}{\tanh(\tau/2)+B}$ $\frac{V}{V_0} = 1+(\frac{1}{2}B+E)\tau+$ $2E\ln(\frac{1+\exp(-\tau)}{2}+\frac{1-\exp(-\tau)}{2B})$	$A = 4\times10^{-28}(\mathrm{m^3 s^{-1}})$ $J_0 = 1.91\times10^{28}(\mathrm{s^{-1}})$ $D = 2\times10^{-28}\ (\mathrm{m^3 s^{-1}})$ $C_0 = 1.91\times10^{28}(\mathrm{s^{-1}})$

4.3.1.2 Validation of aerosol dynamic processes with a sectional method

For more complicated aerosol dynamic processes, this DWOSMC method is verified through a sectional method (Prakash et al., 2003) for three additional cases including one free molecule regime rate coagulation and linear rate condensation case, one free molecule regime rate coagulation and constant rate nucleation case, and one constant rate nucleation, free molecule regime rate coagulation and linear rate condensation case. The parameters and initial conditions for each studied case are given in Table 4.2.

Table 4.2 Parameters and initial conditions used for three verification cases, VI to VIII (Liu and Chan, 2018a).

Problem	Case	Parameters	Initial conditions
Coag+Cond	VI	K is given by Equation (3-5) $I = \sigma_1 v$	$\sigma_1 = 10$ (s^{-1})
Nucl+Coag	VII	K is given by Equation (3-5) $J = J_0$	$J_0 = 1\times10^{20}$(s^{-1})
Nucl+Coag+Cond	VIII	K is given by Equation (3-5) $I = \sigma_1 v$ $J = J_0$	$\sigma_1 = 0.5$ (s^{-1}) $J_0 = 1\times10^{20}$(s^{-1})

4.3.2 Assessment of the numerical simulation results

To assess the accuracy of this newly proposed and developed DWOSMC method, the relative error, ε is utilized in the analysis of the numerical simulation results where ε is expressed as Equation (4-11):

$$\varepsilon = |A(t)\text{-}A_0(t)|/A_0(t) \tag{4-11}$$

where A(t) and A_0(t) are the values obtained via the DWOSMC method and corresponding reference method at time t, respectively. The maximum relative error, ε_{max} is calculated by taking the maximum value of the relative error in Equation (4-11).

4.4 Results and Discussion

4.4.1 Validation with analytical solutions

4.4.1.1 Simultaneous coagulation and condensation processes

For studied cases I to III, 100,000 real particles and the order of 10^{-17} m^3 are used as the initial particle population, N_0 and the initial volume of particles, V_0,

respectively. A simulation period of 200 s is used for Cases I and II, and a simulation period of 3.5 s is used for Case III. An increasing number of simulated particles (i.e., N_p = 100, 500, 1000 and 2000) is used for the calculation.

Figure 4.2(a) to (f) show the variations of particle number concentration and total particle volume concentration as the function of time for Cases I to III. It can be seen that the particle number concentration decreases over time but the total particle volume concentration increases over time for simultaneous coagulation and condensation processes. From Table 4.1, the particle number concentration depends only on the coagulation rate for Cases I and II but not the condensation rate. While for Case III, both the coagulation and condensation rates affect the particle number concentration. For Cases I and III, the total particle volume concentration depends only on the condensation rate but not the coagulation rate. The results obtained from DWOSMC method agree well with the analytical solutions for Cases I to III (Palaniswaamy and Loyalka, 2008; Ramabhadran et al., 1976) as shown in Figure 4.2.

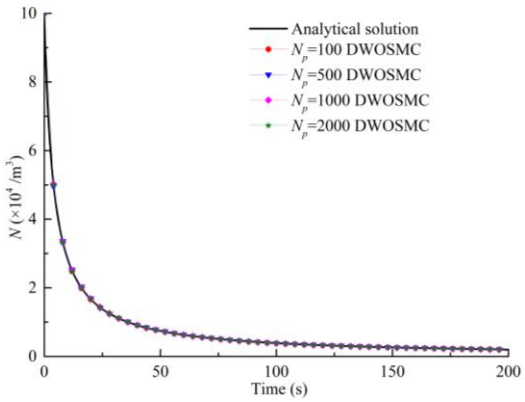

(a) Case I

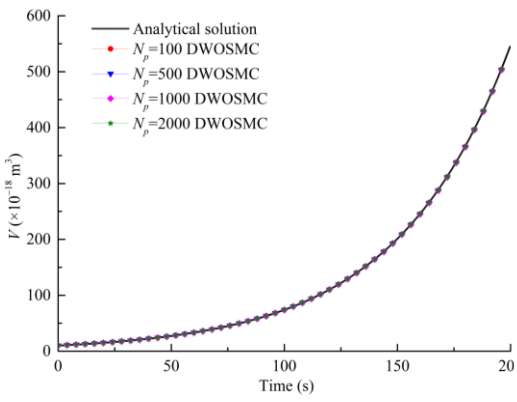

(b) Case I

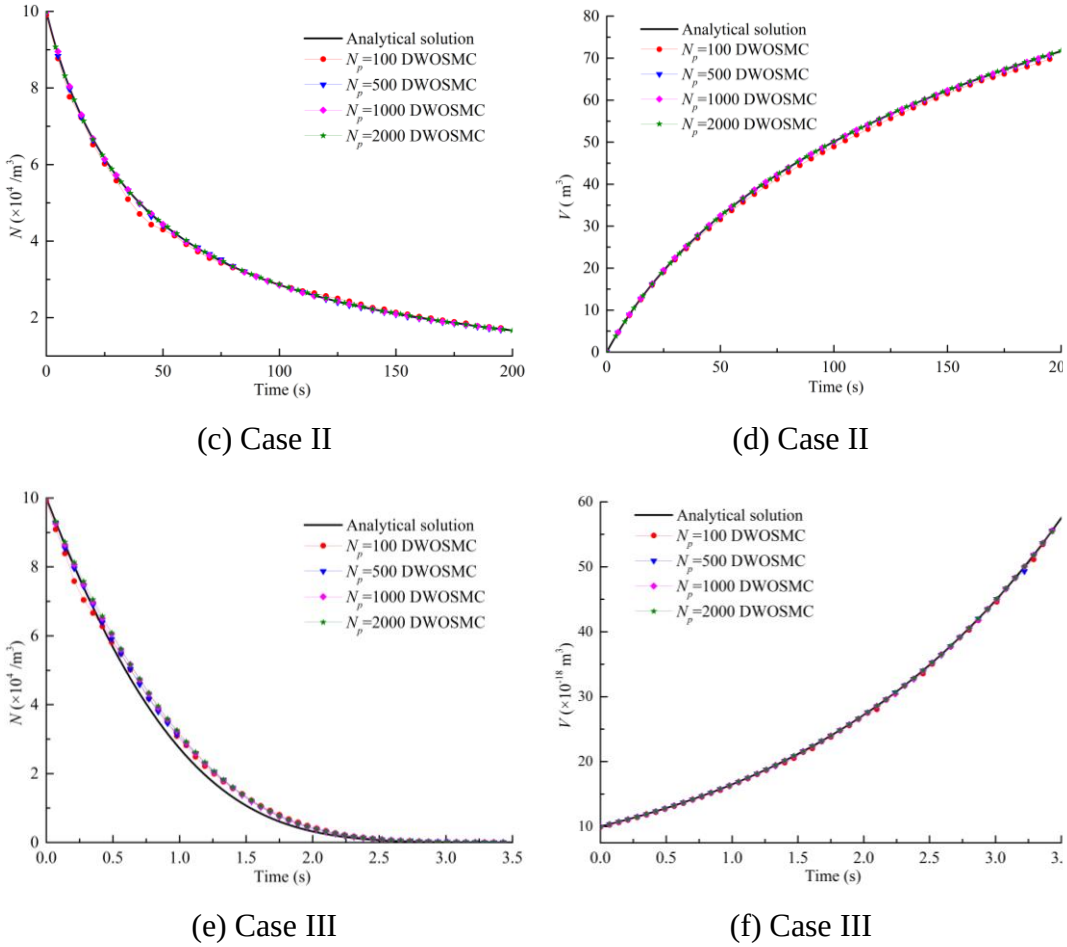

(c) Case II (d) Case II

(e) Case III (f) Case III

Figure 4.2 Evolutions of particle number concentration, N and total particle volume concentration, V as the function of time for different simultaneous coagulation and condensation processes in Cases I to III using both DWOSMC method (Liu and Chan, 2018a) and analytical solutions (Ramabhadran et al., 1976).

4.4.1.2 Simultaneous nucleation and coagulation processes

For studied Case IV, the initial particle number concentration, N_0 and initial total particle volume, V_0 are 1.91×10^{23} and 10^{-4} m^3, respectively. The simulation time, t_{stop} for Case IV is 45 ms. The numerical simulation results of N/N_0 and V/V_0 are shown in Figure 4.3(a) and (b), respectively.

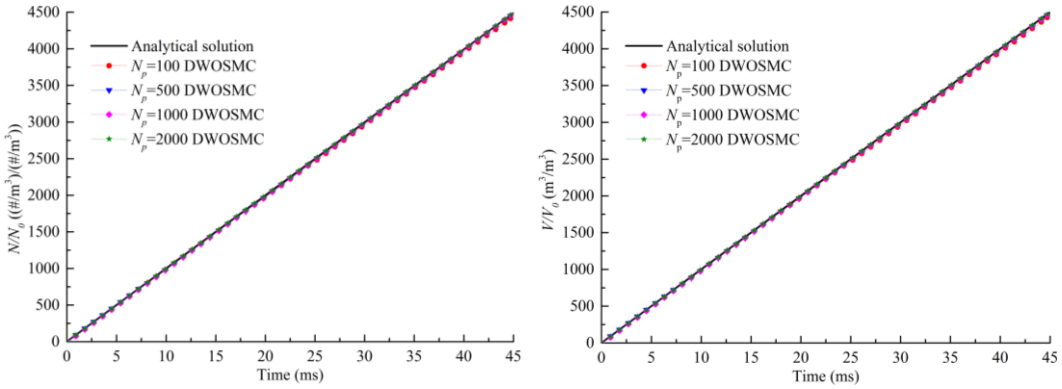

Figure 4.3 Evolutions of (a) N/N_0 and (b) V/V_0 obtained from DWOSMC method and analytical solutions (Maisels et al., 2004) for simultaneous constant rate nucleation and constant rate coagulation processes in Case IV (Liu and Chan, 2018a).

It can be found that the results show approximately linear relationship within a short period of time. The numerical simulation results obtained from DWOSMC method are consistent with the analytical solutions. When the simulated particle number reaches 500, both the evolutions for the particle number concentration and the total particle volume demonstrate very small fluctuations and relative errors.

4.4.1.3 Simultaneous nucleation, coagulation and condensation processes

For Case V, the initial particle number concentration, N_0 and initial total particle volume, V_0 are 1.91×10^{23} and 1×10^{-4} m^3, respectively. The simulation time for Case V is 45 ms. The numerical simulation results of N/N_0 and V/V_0 are shown in Figure 4.4 (a) and (b), respectively. Similar to Case IV in Figure 4.3, both the evolutions of N/N_0 and V/V_0 exhibit nearly linear relationship within a very short period of time. Even when only 100 simulated particles are used, the numerical simulation results remain very high consistency with the analytical solutions for constant rate nucleation, coagulation and condensation processes.

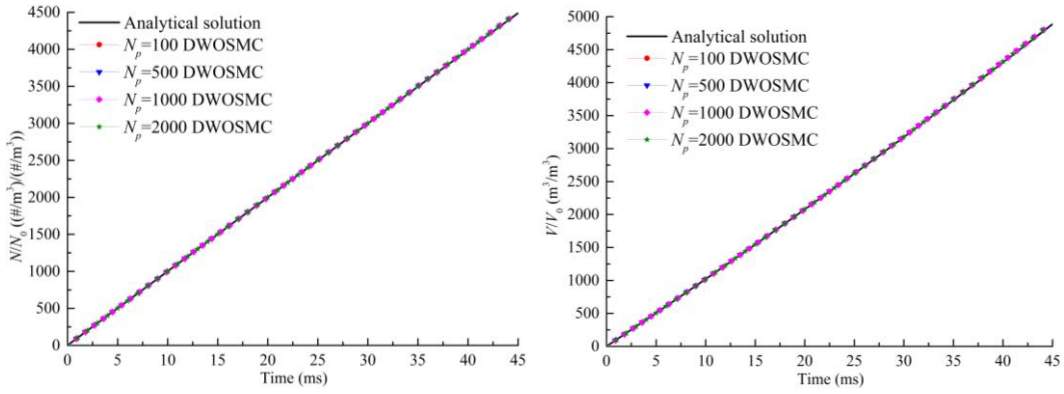

(a) (b)

Figure 4.4 Evolutions of (a) N/N_0 and (b) V/V_0 obtained from DWOSMC method and analytical solutions (Maisels et al., 2004) for simultaneous constant rate nucleation, constant rate coagulation and constant rate condensation processes in Case V (Liu and Chan, 2018a).

4.4.2 Validation with a sectional method

4.4.2.1 Simultaneous coagulation and condensation processes

For Case VI, the initial particle number concentration, N_0 and initial total particle volume, V_0 are 1×10^{18} and 1.77×10^{-9} m^3, respectively. The simulation time used is 10 ms. The evolutions of particle number concentration, N, particle average diameter, d, total particle volume concentration, V, and the second moment, M_2, as a function of time for Case VI are shown in Figure 4.5(a) to (d) for simultaneous free molecule regime rate coagulation and linear rate condensation processes. The simulation results of a sectional method are used as a reference.

In Figure 4.5(a), it can be found that the particle number concentration decreases over time because the coagulation reduces the number of particles, whereas the condensation process does not change the number of the particles. The numerical simulation results obtained from DWOSMC method agree well with the sectional method even when only 100 simulated particles are used. For the

evolutions of average particle diameter and the total particle volume, there is significant difference between the simulation results of DWOSMC and sectional method when only 100 simulated particles are used as shown in Figure 4.5(b) and (c), respectively.

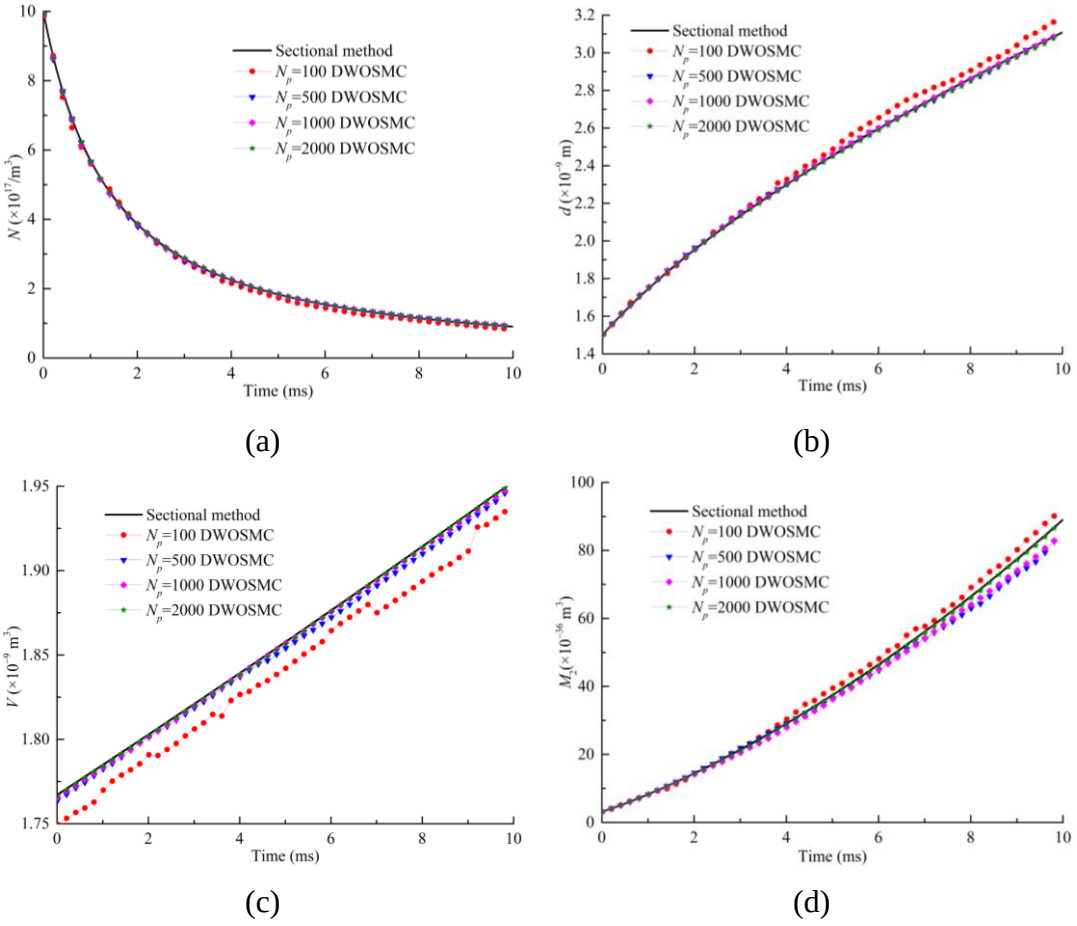

Figure 4.5 Evolutions of (a) the particle number concentration, N, (b) the average particle diameter, d, (c) the total particle volume concentration, V, and (d) the second moment, M_2 obtained from DWOSMC method and sectional method (Prakash et al., 2003) for simultaneous free molecule regime rate coagulation and linear rate condensation processes in Case VI (Liu and Chan, 2018a).

When the simulated particle number reaches 500 or 1000, the simulation results of DWOSMC method are in good agreement with the sectional method. As the coagulation process does not change the total particle volume, the total particle

volume demonstrates an approximate linear relationship over time because the condensation kernel has a linear rate. As both the coagulation and condensation processes contribute to the increase of the particle diameter, the average particle diameter increases quite fast and nonlinearly over time. For the evolutions of the second moment, there are relatively larger errors than for other parameters. But it can be found that as the number of simulated particles increases, the relative error decreases. The relative error is rather small when 2000 simulated particles are used.

4.4.2.2 Simultaneous nucleation and coagulation processes

For Case VII, the initial particle number concentration, N_0 and initial total particle volume, V_0 are 1×10^{18} and 1.77×10^{-9} m^3, respectively. The simulation time for Case VII is 4.5 ms. The evolutions of particle number concentration, N, particle average diameter, d, total particle volume concentration, V, and the second moment, M_2, as a function of time for Case VII are shown in Figure 4.6(a) to (d) for simultaneous free molecule regime rate coagulation and constant rate nucleation processes.

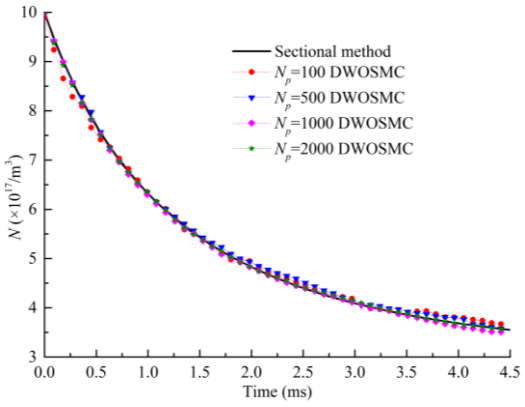

(a)

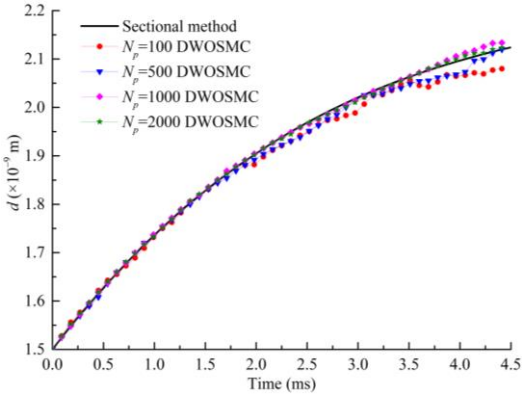

(b)

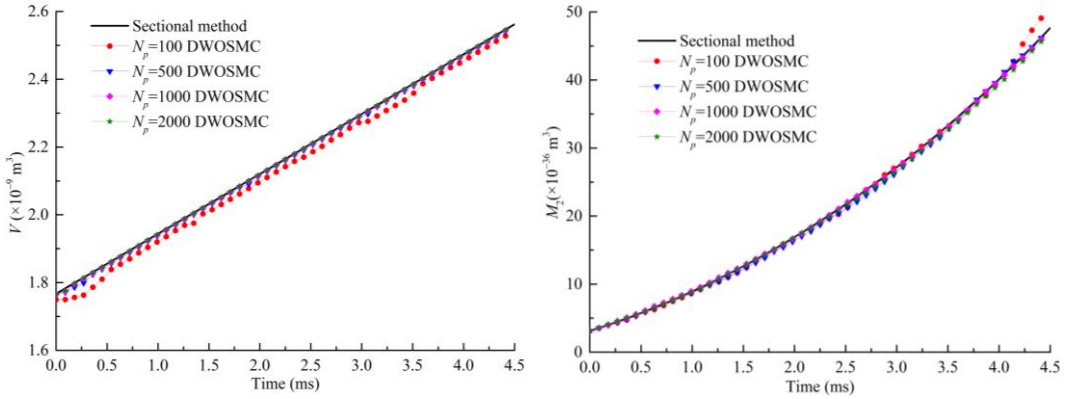

(c) (d)

Figure 4.6 Evolutions of (a) the particle number concentration, N, (b) the particle average diameter, d, (c) the total particle volume concentration, V, and (d) the second moment, M_2 obtained from DWOSMC method and sectional method (Prakash et al., 2003) for free molecule regime rate coagulation and constant rate nucleation processes in Case VII (Liu and Chan, 2018a).

From Figure 4.6(a) and (b), it can be found that the coagulation process dominates the entire process, because the particle number concentration decreases and the average particle diameter increases over time. However, for the nucleation process, the particle number concentration increases and the average particle diameter decreases over time. Hence, the coagulation process completely eliminates the effect of the nucleation process. While from Figure 4.6(c) and (d), the effect of nucleation process can be clearly observed as the total particle volume and the second moment increase over time. In Figure 4.6, it can also be found that when 1000 simulated particles are used, the numerical simulation results obtained from DWOSMC method agree well with the sectional method, with very small fluctuations and errors.

4.4.2.3 Simultaneous nucleation, coagulation and condensation processes

For Case VIII, the initial particle number concentration N_0 and initial total particle volume V_0 are 1×10^{18} and 1.77×10^{-9} m^3, respectively. The simulation time

for Case VIII is 3 ms. The evolutions of the particle number concentration, N, the average particle diameter, d, the total particle volume concentration, V, and the second moment, M_2, as a function of time for Case VIII are shown in Figure 4.7(a) to (d), respectively, for simultaneous constant rate nucleation, free molecule regime rate coagulation and linear rate condensation processes.

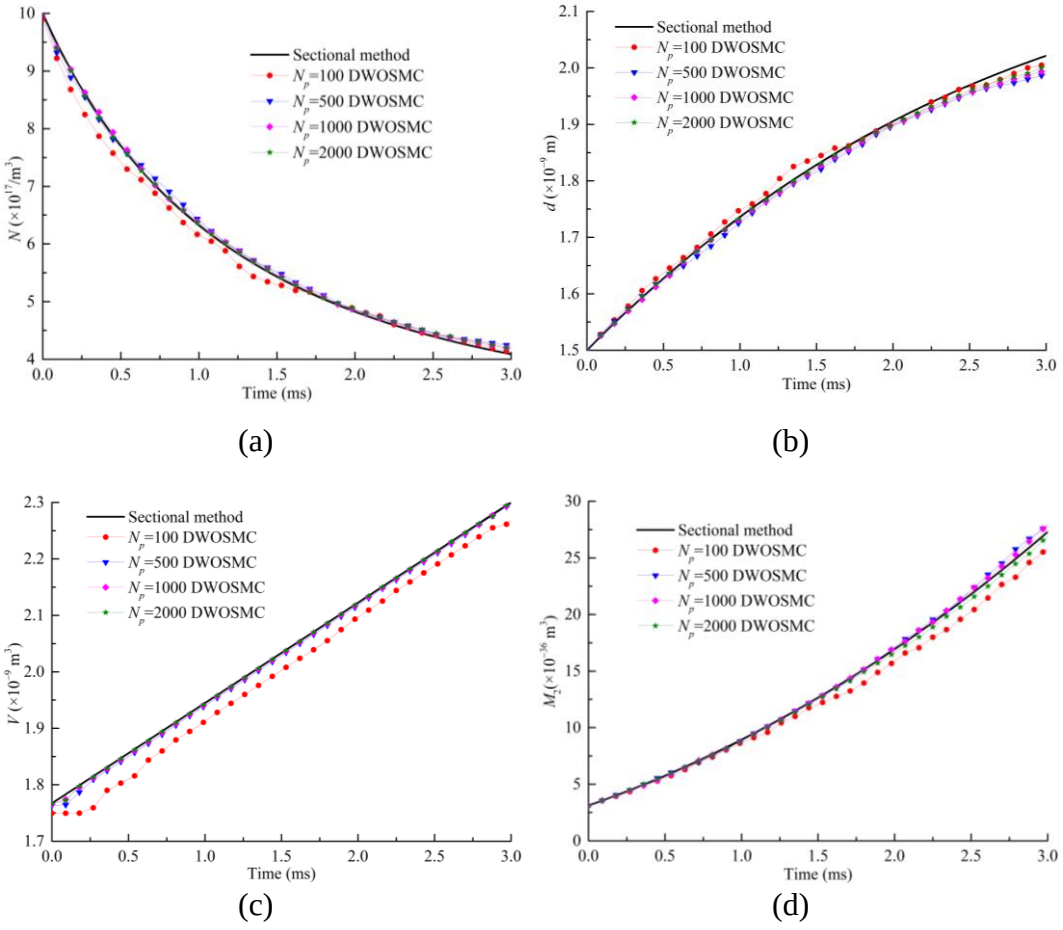

Figure 4.7 Evolutions of (a) the particle number concentration, N, (b) the particle average diameter, d, (c) the total particle volume concentration, V, and (d) the second moment, M_2, obtained from DWOSMC method and sectional method (Prakash et al., 2003) for simultaneous constant rate nucleation, free molecule regime rate coagulation and linear rate condensation processes in studied Case VIII (Liu and Chan, 2018a).

Figure 4.7(a) to (d) show that for the particle number concentration, N, the average particle diameter, d, the total particle volume, V, and the second moment

of particles, M_2, the numerical simulation results of DWOSMC method agree well with the sectional method when 1000 to 2000 simulated particles are used.

4.4.3 Computational efficiency and accuracy analysis

To further understand the computational efficiency and accuracy of this newly proposed and developed DWOSMC method, the maximum relative error for the particle number concentration and the total particle volume for the case studies are shown in Table 4.3 and Table 4.4. It is clearly shown that, for the same case, the maximum relative error decreases when the number of simulated particles increases. For different cases, the more complicated the case is, the higher the maximum relative error is. For constant rates in Cases IV and V, the maximum relative errors are within 1% when only 500 simulated particles are used, whereas for Cases VII and VIII, more simulated particles are needed to achieve the same accuracy. For Table 4.3 and Table 4.4, the numerical results show that the maximum relative errors obtained from the particle number concentration are commonly larger than those obtained from the total particle volume. For most of the cases, when the number of simulated particles reaches 2000, the maximum relative errors obtained from the particle number concentration are within 2%, whereas the maximum relative errors obtained from the total particle volume are within 1%. It is because the evolution of the particle number concentration is mainly due to the stochastic coagulation process, which is calculated by Monte Carlo method by introducing some statistical errors. The evolution of the total particle volume is mainly caused by the nucleation and condensation processes which are calculated by deterministic method with much smaller errors. This also indicates that for most of the classical and typical cases used in the present study, 2000 simulated particles are sufficiently good with small errors

which indicates that this newly proposed and developed DWOSMC method provides very high computational efficiency and accuracy.

Table 4.3 The maximum relative error of N for different cases using DWOSMC method compared with the analytical solutions or the sectional method (Liu and Chan, 2018a).

ε_{max}(%) for N / Case	Particle number, N_p			
	100	500	1000	2000
I	5.51	2.22	1.71	0.80
II	2.30	1.71	0.91	0.62
III	4.01	3.52	2.82	1.79
IV	2.31	0.15	0.16	0.03
V	0.40	0.32	0.26	0.20
VI	8.22	2.33	1.51	1.00
VII	4.12	3.11	2.20	1.22
VIII	5.53	3.22	2.21	2.00

Table 4.4 The maximum relative error of V for different cases using DWOSMC method compared with the analytical solutions or the sectional method (Liu and Chan, 2018a).

ε_{max}(%) for V / Case	Particle number N_p			
	100	500	1000	2000
I	1.51	0.22	0.20	0.08
II	2.71	0.58	0.31	0.20
III	6.01	1.22	0.71	0.52
IV	2.46	0.19	0.21	0.07
V	0.63	0.50	0.41	0.32
VI	1.20	0.27	0.15	0.10
VII	3.01	0.82	0.61	0.50
VIII	3.20	1.52	0.61	0.58

4.5 Summary

A newly differentially weighted operator splitting Monte Carlo (DWOSMC) method is developed and verified by corresponding analytical solutions and a sectional method through classical and typical cases including four cases for simultaneous coagulation and condensation processes in different regimes, two cases for simultaneous nucleation and coagulation processes in different regimes, and two cases for different simultaneous nucleation, coagulation and condensation processes. For the relatively typical cases, the numerical simulation results of DWOSMC method demonstrates very good consistency with the analytical solutions. For the complex cases, the numerical simulation results of DWOSMC method are also consistent with the results obtained from the sectional method. In some cases, only 500 simulated particles are good enough for obtaining the maximum relative error within 1%. Even for the most complex case in the present study, 2000 simulated particles are sufficient to simulate the particle number concentration, the total particle volume concentration, the average particle diameter and the second moment of particles. This newly proposed and developed DWOSMC method is proved to have very high computational efficiency and accuracy, and has a high potential for solving complex aerosol dynamic problems.

Chapter 5 Monte Carlo Simulation of two-component Aerosol Dynamics

5.1 Introduction

In natural or engineering applications, aerosol particles are essentially multivariate in compositions, such as acid rain formation and downfall, soot formation and growth in combustion chambers, nanoparticle synthesis in applications of ceramics and drug delivery, heterotypic processes of blood components etc. (Fang et al., 2018; Fino et al., 2016; Kolb and Worsnop, 2012). In these fields, particles often consist of multiple components, and the compositional distribution affects the properties of particles. Many properties of particles such as light scattering, radioactivity and capturing strategy are highly dependent on the particle size and compositional distributions. Therefore, in this chapter, the newly proposed and developed differentially weighted operator splitting Monte Carlo (DWOSMC) method is further developed to study multi-component properties of aerosol dynamics considering coagulation and condensation processes that are very important phenomena for having a better understanding of the evolution of particle size and compositional distributions.

5.2 Numerical Methodology

5.2.1 General dynamic equation

According to Section 3.2.2, the governing equation for a two-component aerosol system that only considers coagulation and condensation processes becomes (Gelbard and Seinfeld, 1978; Zhao and Zheng, 2011),

$$\frac{\partial n(v_A,v_B,t)}{\partial t} =$$
$$\frac{1}{2}\int_0^{v_A}\int_0^{v_B} K(v_A - v_A',v_B - v_B',v_A',v_B', t)\, n(v_A - v_A',v_B - v_B', t)n(v_A',v_B', t)\mathrm{d}v_A'\mathrm{d}v_B'$$
$$-n(v_A,v_B,t)\int_0^{\infty}\int_0^{\infty} K(v_A,v_B,v_A',v_B', t)n(v_A',v_B', t)\mathrm{d}v_A'\mathrm{d}v_B'$$
$$-\frac{\partial(I_A n)}{\partial v_A}(v_A,v_B,t) - \frac{\partial(I_B n)}{\partial v_B}(v_A,v_B,t) \qquad (5\text{-}1)$$

5.2.2 Extension of the DWOSMC to two-component systems

In Chapter 4, a differentially weighted operator splitting Monte Carlo (DWOSMC) method is newly proposed and developed for one-component aerosol systems by using the operator splitting (OS) technique to combine stochastic MC and deterministic integration methods. In the present study, the DWOSMC method is further developed to simulate multi-component aerosol systems. A brief outline of the algorithm's application to two-component systems for coagulation and condensation processes is given as follows:

(a) Start the predetermined Monte Carlo loop number, *M*.

(b) Initialization. The initial value of particle properties (e.g., size, weight, number concentration, component composition, etc.) is first assigned according to an initial compositional distribution. During the simulation of the DWOSMC method, the weights of different simulated particles can be different. For a two-component aerosol system, w_i is defined as,

$$w_i = \frac{N_r(v_A,v_B)}{N_s(v_A,v_B)} \qquad (5\text{-}2)$$

where $N_r(v_A,v_B)$ is the number of real particles of A-component volume size, v_A and B-component volume size, v_B and $N_s(v_A,v_B)$ is the number of simulated particles representing those real particles, $N_r(v_A,v_B)$. In the present study, the weights of all simulated particles are set to the same value, $w_{i,0}$ at the time of initialization. The initial size, v_0 and number density distributions, $n(v_A,v_B,0)$ of the particles are set according to the initial particle distributions assigned.

(c) Choose a time-step, δt. A variable time scale is determined by different aerosol dynamic processes. Specifically, the characteristic time scale used for coagulation events is written as Equation (4-7), For condensation events, the characteristic time scale is written as Equation (4-9).

To guarantee the accuracy of this newly proposed method in simulating both condensation and coagulation processes, an appropriate time-step that is smaller than both characteristic time scales of the two events should be used. In the present study, the time-step is written as:

$$\delta t = \alpha \min(\Delta t_{coag}, \Delta t_{cond}) \tag{5-3}$$

where α is an empirical parameter set as 0.01 (Xu et al., 2014; Zhao et al., 2009) during calculation to ensure that an accurate integration of aerosol dynamic processes is achieved.

(d) Integration. Stochastic and deterministic aerosol dynamic processes are managed by applying the second-order Strang splitting method (Mclachlan and Quispel, 2002) which is expressed as:

$$\exp(\delta t X) = \exp\left(\frac{1}{2}\delta t X_2\right)\exp(\delta t X_1)\exp\left(\frac{1}{2}\delta t X_2\right) + \mathcal{O}(\delta t^3) \tag{5-4}$$

where X is the total process of two sub-processes, and X_1 and X_2 refer to the coagulation process and condensation process, respectively.

Within the time-step, the condensation process is first calculated for the first half time-step, $\delta t/2$, and then the coagulation process is simulated for one time-step, δt. Finally, the condensation process is calculated for the last half time-step of $\delta t/2$. The integration procedure used for the total process of the two sub-processes for one time-step is described in steps (e) to (g).

(e) Integration of condensation for a time-step of $\delta t/2$.

The condensation event affects the particle size distribution of aerosols because it produces larger particles. In two-component systems, there are two condensation kernels (i.e., one for component A and one for component B) written as $I_A(v_A)$ and $I_B(v_B)$, respectively. In the present study, all particles are assumed to be spherical and that the volume of particles is the sum of their two components after the condensation event which is written as:

$$\frac{\mathrm{d}v_i(v_A,v_B,t)}{\mathrm{dt}} = I_A(v_A)+I_B(v_B) \tag{5-5}$$

Specifically, in the present study, the condensation event within a time-step of $\delta t/2$ is calculated as:

$$v_i^{'} = v_i + (I_A(v_A)+I_B(v_B))\delta t/2 \tag{5-6}$$

$$w_i^{'} = w_i \tag{5-7}$$

where w_i and v_i refer to the weight and volume of simulated particle, i, respectively, before the condensation event and $w_i^{'}$, and $v_i^{'}$ refer to the weight and volume of simulated particle i, respectively, after the condensation event.

(f) Integration of coagulation for a time-step of δt.

The simulation of coagulation is based on the DWMC method proposed by Zhao et al. (Zhao et al., 2010, 2009). The occurrence of coagulation events between two particles, *i* and *j* is based on probability selections and is calculated according to Equations (3-9) to (3-12).

After the coagulation event, the previous particles are replaced with two newly weighted simulated particles, and the conservation of volume is considered while the properties of these particles are changed. The coagulation process is described as:

$$\text{If} \quad w_i = w_j, \begin{cases} w_i^{'}=w_i/2;\ v_i^{'}=v_i+v_j,\ v_{i,\mathrm{A}}^{'}=v_{i,\mathrm{A}}+v_{j,\mathrm{A}},\ v_{i,\mathrm{B}}^{'}=v_{i,\mathrm{B}}+v_{j,\mathrm{B}}; \\ w_j^{'}=w_j/2;\ v_j^{'}=v_i+v_j;\ v_{j,\mathrm{A}}^{'}=v_{i,\mathrm{A}}+v_{j,\mathrm{A}},\ v_{j,\mathrm{B}}^{'}=v_{i,\mathrm{B}}+v_{j,\mathrm{B}}; \end{cases} \tag{5-8a}$$

$$\text{If} \quad w_i \neq w_j, \begin{cases} w_i^{'}=\max(w_i,w_j)-\min(w_i,w_j);v_i^{'}=v_m|_{w_m=\max(w_i,w_j)}; \\ v_{i,\mathrm{A}}^{'}=v_{m,\mathrm{A}}|_{w_m=\max(w_i,w_j)},\ v_{i,\mathrm{B}}^{'}=v_{m,\mathrm{B}}|_{w_m=\max(w_i,w_j)}\ ; \\ w_j^{'}=\min(w_i,w_j);v_j^{'}=v_i+v_j; \\ v_{j,\mathrm{A}}^{'}=v_{i,\mathrm{A}}+v_{j,\mathrm{A}},\ v_{j,\mathrm{B}}^{'}=v_{i,\mathrm{B}}+v_{j,\mathrm{B}}; \end{cases} \tag{5-8b}$$

where $w_i^{'}$, $w_j^{'}$, $v_i^{'}$ and $v_j^{'}$ represent the weight or volume of newly created simulated particles, *i* and *j* after the coagulation event. $v_{i,\mathrm{A}}^{'}$, $v_{i,\mathrm{B}}^{'}$, $v_{j,\mathrm{A}}^{'}$ and $v_{j,\mathrm{B}}^{'}$ are the volumes of components, A and B in newly created simulated particles, *i* and *j* after the coagulation event. In the present study, the density of particles is assumed to be constant, and so the conservation of particle volume in Equation (5-8) denotes the conservation of mass during the coagulation event.

(g) Condensation is integrated for a time-step of $\delta t/2$. The calculation procedure is the same as that used in step (e).

(h) The properties of simulated particles are updated to obtain information (size, composition and number density, etc.) on the particles, as the particles are assumed to be spherical before and after coagulation and condensation events, and thus particle diameters can be easily obtained.

(i) Repeat steps (c) to (h) until the predetermined stopping time, t_{stop} is reached, and then exit the current Monte Carlo loop.

(j) Start a new Monte Carlo loop if the calculated Monte Carlo loop number, R is smaller than the predetermined Monte Carlo loop number, M. Otherwise the averaged results are obtained to output the information of the aerosol system. In the present study, eight Monte Carlo loops are carried out.

Figure 5.1 presents a flowchart of the full algorithm of the two-component DWOSMC method.

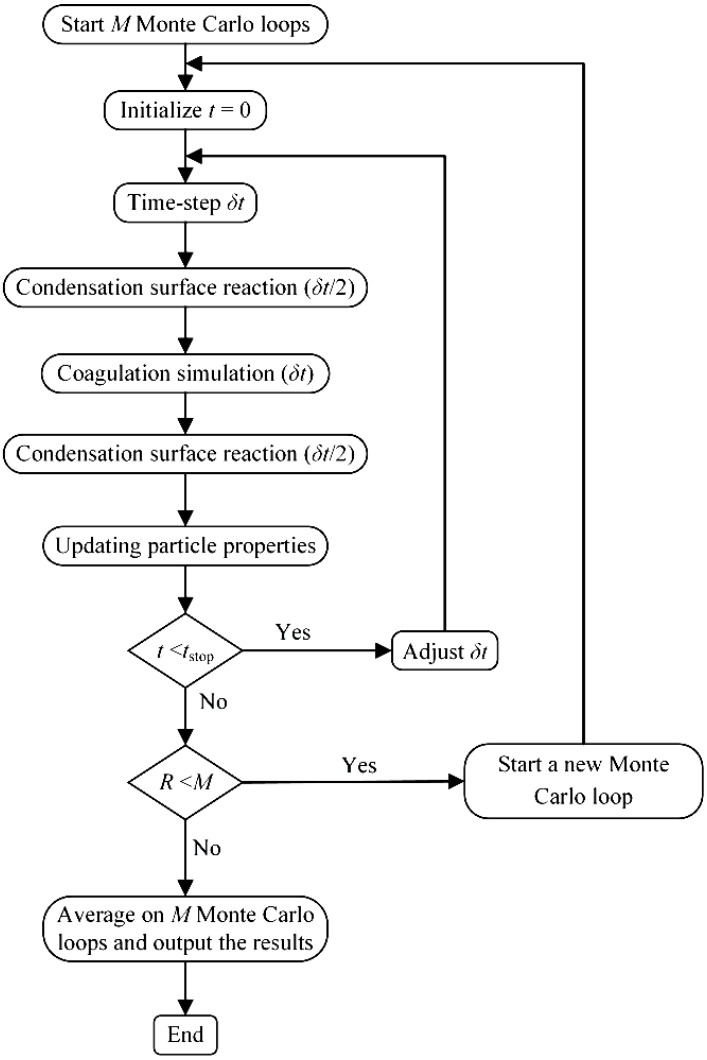

Figure 5.1 Flowchart of the two-component DWOSMC algorithm (Liu and Chan, 2018b).

5.3 Results and Discussion

In the present study, the performance of this newly proposed and developed multi-component DWOSMC method is evaluated using a sectional method (Prakash et al., 2003), which is also further developed according to the concept of Kim and Seinfeld (1990) on a moving sectional method that describes the two-component system. First, the DWOSMC and sectional methods are evaluated in a simple one-component case for which analytical solutions exist. Then, two-

component systems with different kernels and initial particle size distributions are examined to determine the capacity of the multi-component DWOSMC method to simulate aerosol dynamics. In the present study, different cases are successively investigated to study the simultaneous coagulation and condensation processes. For the sectional method, particles only exist at discretized nodes, and the aerosol size spectrum is divided into 50~70 sections. The same number of nodes is also used for the DWOSMC method to store the particle size and compositional distributions of aerosols.

5.3.1 One-component coagulation and condensation case

This developed multi-component DWOSMC method is firstly used to calculate a one-component aerosol system by setting the growth kernels of components A and B to be the same. The results are verified by analytical solutions, and compared with the sectional method (Kim and Seinfeld, 1990; Prakash et al., 2003) and a non-weighted direct simulation Monte Carlo (DSMC) method (Liffman, 1992) to evaluate the computational efficiency and accuracy of this DWOSMC method.

For a one-component aerosol system, a constant kernel coagulation and a linear kernel condensation are considered in Case I. The initial particle distribution and the coagulation and condensation kernels are the same with Case I in Section 4.3. From Table 4.1, the analytical solutions for dimensionless particle number concentration $N(t)/N_0$, and total particle volume concentration $V(t)/V_0$ are given by,

$$N(t)/N_0 = \frac{1}{1 + K_0 N_0 t/2} \tag{5-9}$$

$$V(t)/V_0 = \exp(\sigma_1 t) \tag{5-10}$$

Figure 5.2(a) shows the time evolution of dimensionless particle number concentration N/N_0 and total particle volume V/V_0. For simultaneously occurring coagulation and condensation processes, the particle number density decreases over time due to the coagulation event, and the total particle volume increases over time due to the condensation process. As expected, excellent matches are found from the SM, DWOSMC and DSMC methods and from the analytical solutions, respectively.

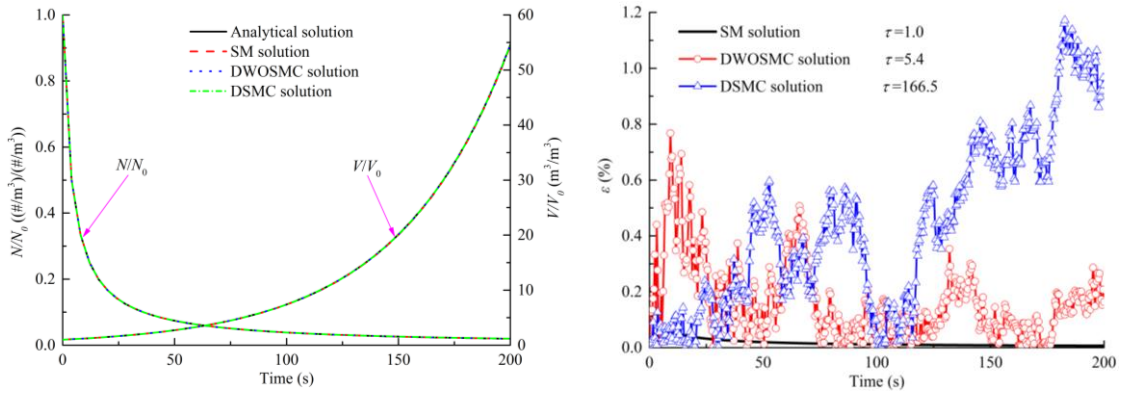

(a) (b)

Figure 5.2 Time evolution of (a) dimensionless particle number concentration, N/N_0 and total particle volume, V/V_0 ; and (b) the relative error, ε (%) for N/N_0 obtained from the SM, DWOSMC and DSMC methods, and the corresponding normalized computation time, τ for Case I (Liu and Chan, 2018b).

The computational accuracy and efficiency of the three methods are further examined. The relative error, ε (%) of the particle number concentration and normalized computation time, τ are shown in Figure 5.2 (b). The relative error, ε is defined as Equation (4-11), and the normalized computation time, τ is defined by the following equations:

$$\tau = t/t_{SM} \tag{5-11}$$

where t_{SM} is the computation time required for SM, and t is the amount of computation time required for corresponding SM, DWOSMC and DSMC methods, respectively.

In Figure 5.2(b), the relative errors, ε obtained from the three methods are quite small and are mostly less than 1%. On the other hand, it is observed that the relative error obtained from the DSMC method is greater than that obtained from the SM and DWOSMC methods. Furthermore, much less computational time is required for the DWOSMC method than for the DSMC method, proving that the DWOSMC method is much more computationally accurate and efficient than the DSMC method. Furthermore, the relative error obtained from the SM is extremely small at less than 0.2% for the whole numerical simulation for Case I. As the SM closely reflects the analytical solution shown in Figure 5.2(a) and (b), it is then used to verify the proposed two-component DWOSMC method in the present study.

The particle number distributions studied in Case I is shown in Figure 5.3, which shows that initially uniform distributed particles evolve into a normal distribution over time. Satisfactory agreement is also found between the SM and Monte Carlo methods.

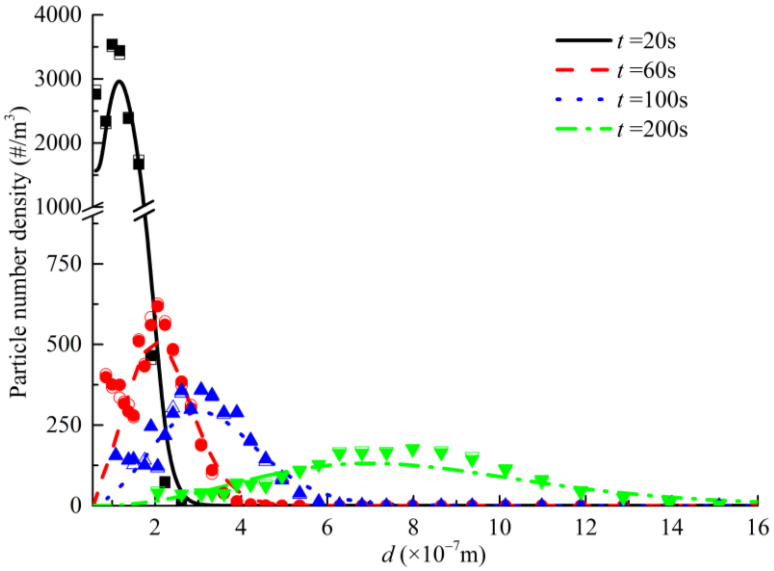

Figure 5.3 Evolution of particle number distributions obtained from the sectional (solid line), DWOSMC (scattered solid points) and DSMC (scattered unshaded points) methods for Case I (Liu and Chan, 2018b).

5.3.2 Two-component coagulation and condensation processes and constant coagulation kernel cases

For a multi-component aerosol system, the component-related volume density of particles is of interest. The total volume density of a particle is defined as (Gelbard et al., 1980; Sandu, 2006),

$$\xi(v,t) = vn(v,t) \tag{5-12}$$

The i-th component related volume density of particle of volume, v is:

$$\xi_i(v,t) = v_i(v,t)n(v,t) \tag{5-13}$$

Specifically, for a two-component system, $\xi_A(v,t)$ and $\xi_B(v,t)$ are the volume density values of the A-component and B-component, respectively, and then $\xi(v,t)= \xi_A(v,t)+ \xi_B(v,t)$.

When particles are divided into multiple sections by size, the component-related volume density of $v_{l,k} < v_k < v_{u,k}$ in size in the k-th section is:

$$q_{a,b}^{k}(t) = \int_{v_{l,k}}^{v_{u,k}} v_{\mathrm{A}}^{a}(v,t) v_{\mathrm{B}}^{b}(v,t) n(v,t) \mathrm{d}v \qquad (0 \le \mathrm{a,b} \le 1) \qquad (5\text{-}14)$$

where $v_{l,k}$ and $v_{u,k}$ are the lower and upper bounds of the volume of particles in the k-th section, respectively and $v = v_{\mathrm{A}}+v_{\mathrm{B}}$. Specifically, $q_{0,0}^{k}$ is the particle number concentration of the k-th section. $q_{1,0}^{k}$, and $q_{0,1}^{k}$ are the particle volume densities of components A and B in the k-th section, respectively.

In the following studied cases, the component-related volume densities of particles are presented in all particle volume sections where the particle volume is converted into a particle diameter as an independent variable. Therefore, $q_{0,0}$ is the particle number distribution, and $q_{1,0}$ and $q_{0,1}$ are the particle volume density distributions of components, A and B, respectively.

5.3.2.1 Initially uniformly distributed and compositionally equal volume case

The initial particle size distribution is considered to be uniform for Case II. The initial total particle number is $N_0 = 10^5/\mathrm{m}^3$ and the initial average particle volume is $v_0 = 1\times10^{-22}$ m^3 where the particles consist of equal volumes of components A and B. The constant coagulation kernel is given by $K_0 = 5\times10^{-6}$ m^3/s, and linear condensation kernels for components, A and B are given by $I_{\mathrm{A}} = \sigma_{\mathrm{A}} v_{\mathrm{A}}$, $\sigma_{\mathrm{A}} = 1\times10^{-3}$/s, and $I_{\mathrm{B}} = \sigma_{\mathrm{B}} v_{\mathrm{B}}$, $\sigma_{\mathrm{B}} = 2\times10^{-3}$/s, respectively. A numerical simulation time of 200 s is used.

Figure 5.4 shows the time evolution of the dimensionless particle number concentration, N/N_0 and total particle volume V/V_0 as well as the particle number distribution for simulation times t of 20, 60, 100 and 200 s. In Figure 5.4(a), the particle number concentration and total particle volume obtained by using the

DWOSMC method are in excellent agreement with those obtained from the SM. In Figure 5.4(b), as the initial particle diameter is uniform and small, the particle number density of small diameters is quite large when the simulation time is 20 s. In addition, as simulation time advances, both coagulation and condensation events take place, and the particle number distribution evolves to a normal distribution after 100 s and 200 s of simulation time. From Figure 5.4(a) and (b), the results of the DWOSMC method coincide with those obtained from the SM.

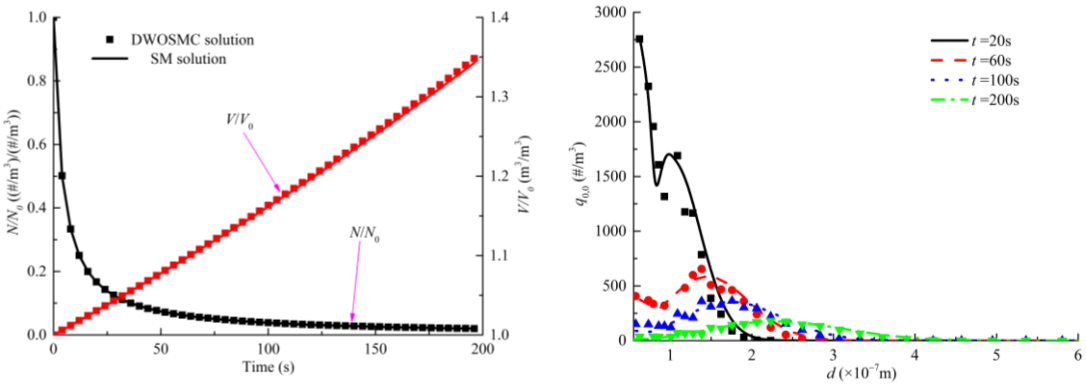

(a) (b)

Figure 5.4 Time evolutions of (a) N/N_0 and V/V_0 and (b) particle number distributions obtained from the SM (solid line) and DWOSMC method (scattered solid points) for Case II (Liu and Chan, 2018b).

The time evolutions of particle volume density distributions of components A and B for Case II are shown in Figure 5.5(a) and (b), respectively. It is shown that the variation tendencies of particle volume density distributions for components A and B are quite similar over time while the peak value of $q_{1,0}$, and $q_{0,1}$ moves along the larger particle diameter, d. This occurs because both coagulation and condensation processes generate a larger average particle diameter. From Figure 5.5(a) and (b), the results obtained from the DWOSMC method agree well with those of the SM. Hence, the DWOSMC method can predict two-component particle

volume distributions for constant coagulation kernels and linear condensation kernels.

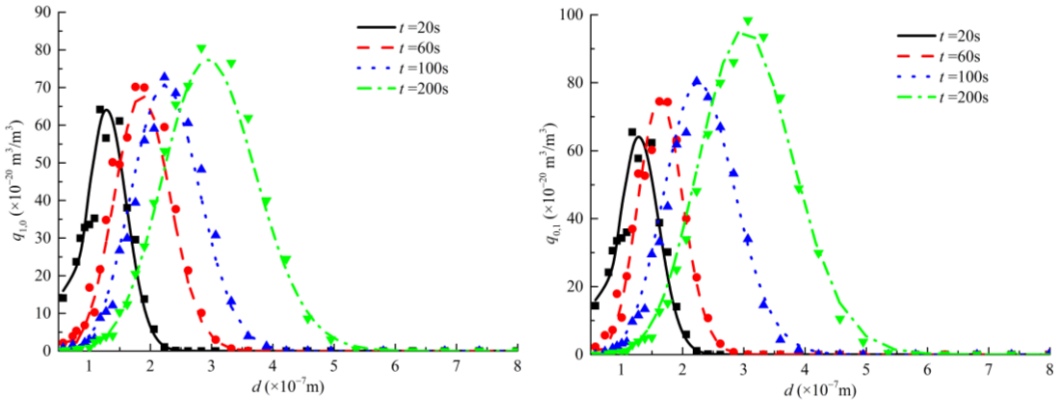

(a) (b)

Figure 5.5 Time evolutions of particle volume density distributions of (a) A-component and (b) B-component obtained from the SM (solid line) and DWOSMC method (scattered solid points) for Case II (Liu and Chan, 2018b).

5.3.2.2 Initially uniformly distributed and compositionally different volume case

The initial particle size distribution is considered to be uniform while the compositions of components, A and B are different for Case III. The initial total particle number is $N_0 = 10^5/\text{m}^3$ and the initial average particle volume is $v_0 = 1\times10^{-22}$ m^3 while the volumes of components A and B are $v_{A0} = v_0/3$ and $v_{B0} = 2v_0/3$, respectively. Coagulation and condensation kernels are the same as those used for Case II. A simulation period of 200 s is used.

The time evolution of dimensionless particle number density, N/N_0 and total particle volume, V/V_0, as well as the particle number distribution of, $q_{0,0}$ for different simulation times (i.e., 60 and 200 s) for Case III are shown in Figure 5.6. For N/N_0 and V/V_0, results obtained from the SM and DWOSMC method show excellent agreement with one another. For $q_{0,0}$, the distribution of $q_{0,0}$ suffers fluctuations when the simulation time is 60 s, and fluctuations resulting from the DWOSMC method

tend to be greater than those of the SM, but the distribution curve for these two methods share the similar patterns. The distribution of $q_{0,0}$ is normal when the simulation time reaches 200 s, and results obtained from the DWOSMC method and SM agree well with one another.

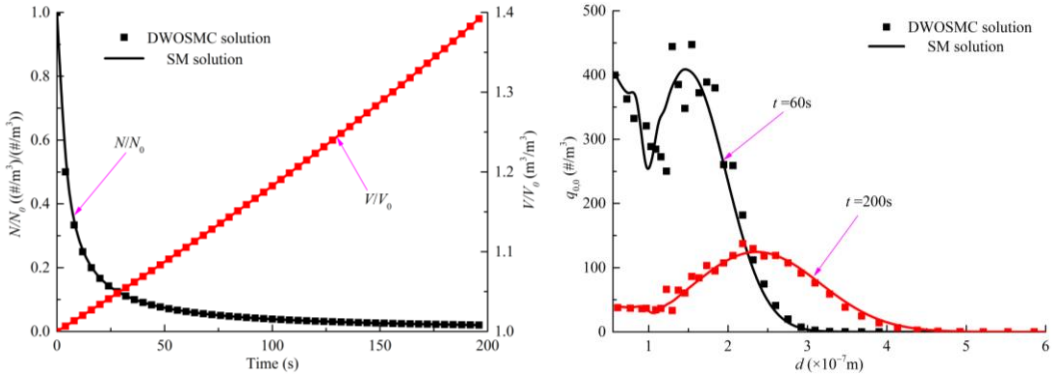

(a) (b)

Figure 5.6 Time evolution of (a) N/N_0 and V/V_0 and (b) particle number distributions obtained from the SM (solid line) and DWOSMC method (scattered solid points) for Case III (Liu and Chan, 2018b).

Figure 5.7 shows the particle volume density distributions of components, A and B for different simulation times (i.e., 60 s and 200 s). From Figure 5.7(a), while the distribution trends of these two methods are similar for a simulation time of 60 s, but some fluctuations result from the DWOSMC method. While such fluctuations vanish when the simulation time reaches 200 s and while the distributions of $q_{1,0}$, and $q_{0,1}$ increase and broaden, results obtained from the DWOSMC method agree well with those obtained from SM.

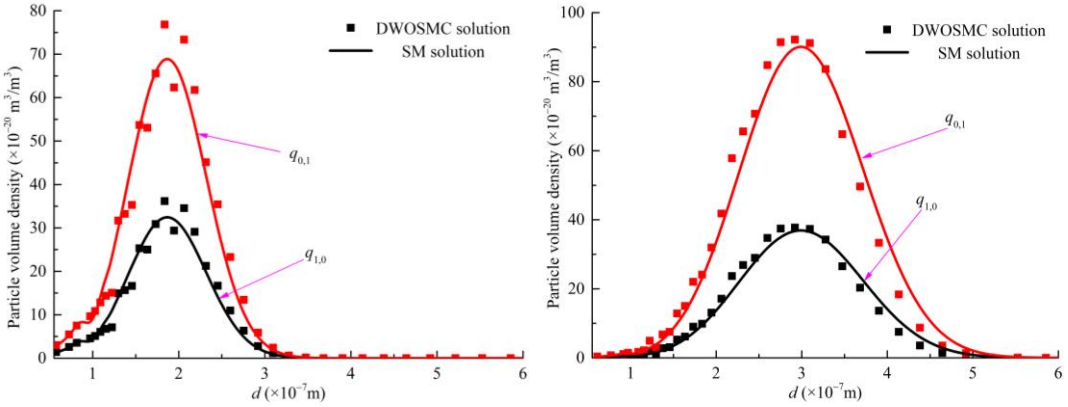

Figure 5.7 Particle volume density distributions of $q_{1,0}$ and $q_{0,1}$ for simulation times (a) t = 60 s and (b) t = 200 s obtained from the SM (solid line) and DWOSMC method (scattered solid points) for Case III (Liu and Chan, 2018b).

5.3.2.3 Initially non-uniformly distributed and compositionally different volume case

The initial particles are exponentially distributed according to Equation (5-15) (Zhao et al., 2005b), and the compositions of components, A and B are different for Case IV. The initial total particle number is N_0 =10^5/m^3, and the initial average particle volume is v_0 = 1×10^{-22} m^3 while the volumes of components, A and B are $v_{A0} = v_0/3$ and $v_{B0} = 2v_0/3$, respectively. Coagulation and condensation kernels used are the same as those used for Case II. A simulation period of 200 s is used.

$$n(v_A,v_B,0) = N_0/v_0\times\exp(-\frac{v(v_A,v_B,0)}{v_0}) \quad (5\text{-}15)$$

In Figure 5.8(a), it is remarkable that dimensionless particle number density, N/N_0 and total particle volume, V/V_0 values obtained from the SM and DWOSMC method are in excellent agreement with one another. The particle number distributions observed at simulation times, t = 20 s and 200 s are shown in Figure 5.8(b). It should be noted that for the initially exponentially distributed case,

the PSD for simulation time, t = 20 s more closely reflects a normal distribution than it does for initially uniformly distributed Case II**.** Particles are normally distributed when the simulation time reaches 200 s. The results obtained from the DWOSMC method are in excellent agreement with those obtained from SM.

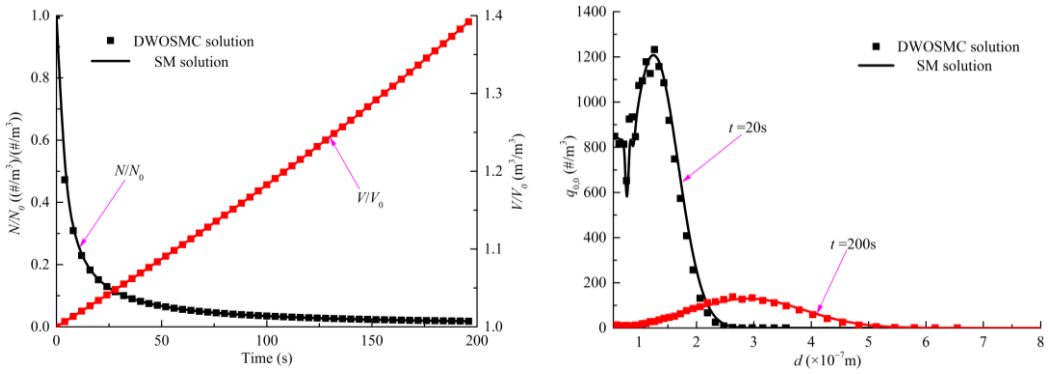

(a) (b)

Figure 5.8 Time evolution of (a) N/N_0 and V/V_0 and (b) particle number distributions obtained from the SM (solid line) and DWOSMC method (scattered solid points) for Case IV (Liu and Chan, 2018b).

The component related particle volume density distributions of $q_{1,0}$, and $q_{0,1}$ obtained over simulation periods t = 20 s and 200 s are shown in Figure 5.9(a) and (b), respectively. It can be clearly observed that the particle volume density distributions of both components increase and grow broader, and that the difference between the particle volume density distributions of components A and B is pronounced. Particle volume density distributions obtained through the DWOSMC are consistent with those obtained from the SM.

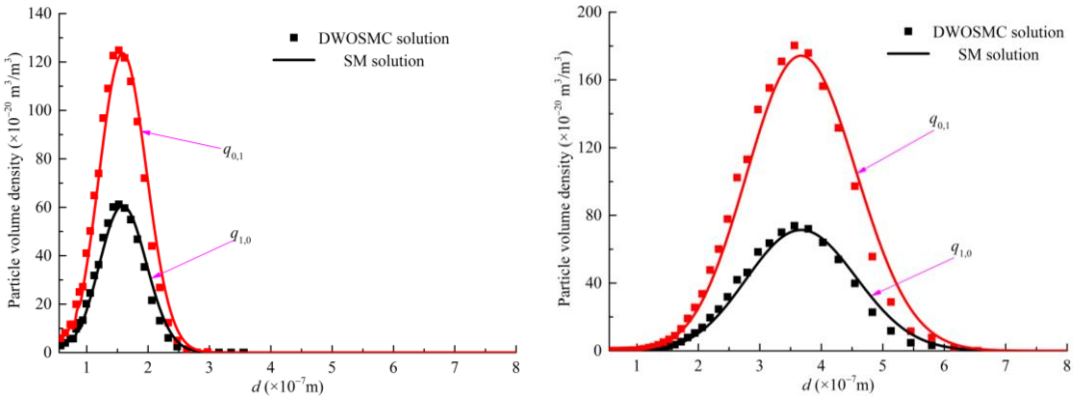

Figure 5.9 Particle volume density distributions of $q_{1,0}$ and $q_{0,1}$ for simulation times (a) t = 20 s and (b) t = 200 s obtained from the SM (solid line) and DWOSMC method (scattered solid points) for Case IV (Liu and Chan, 2018b).

5.3.3 Two-component coagulation and condensation processes and the sum coagulation kernel case

The coagulation kernel is no longer constant and is written as $K = K_0(v_i+v_j)$ (Zhao et al., 2010) for Case V. The initial particle size distribution satisfies a normal distribution according to Equation (5-16), and the compositions of components A and B are different. The initial total particle number is $N_0 = 10^{11}$/m^3 and the initial average particle volume is $v_0 = 5\times10^{-19}$ m^3 while the volumes of components, A and B are $v_{A0} = v_0/3$, $v_{B0} = 2v_0/3$, respectively. The standard deviation σ is 2×10^{-18} m^3. The linear condensation kernels for components A and B are given by $I_A = \sigma_A v_A$, $\sigma_A = 1\times10^{-3}$/s, $I_B = \sigma_B v_B$ and $\sigma_B = 2\times10^{-3}$/s, respectively. A simulation period of 100 s is used.

$$n(v_A,v_B,0) = \frac{N_0}{\sqrt{2\pi}\sigma}\times\exp\left(-\frac{(v(v_A,v_B,0)-v_0)^2}{2\sigma^2}\right) \quad (5\text{-}16)$$

The time evolution of dimensionless particle number density N/N_0 and total particle volume V/V_0, and the particle number distribution of $q_{0,0}$ for simulation times, 10 s and 100 s are shown in Figure 5.10 for Case V. As expected, for N/N_0 and V/V_0,

results obtained from the DWOSMC and SM are in agreement with one another. For the particle size distribution shown in Figure 5.10(b), as particles are initially normally distributed, the distribution of $q_{0,0}$ closely reflects a normal distribution when the simulation time reaches 10 s. In contrast to patterns found from the other cases, the peak diameter of particles almost remains at the same value for Case V. The results obtained from the DWOSMC method and SM are in excellent agreement with one another.

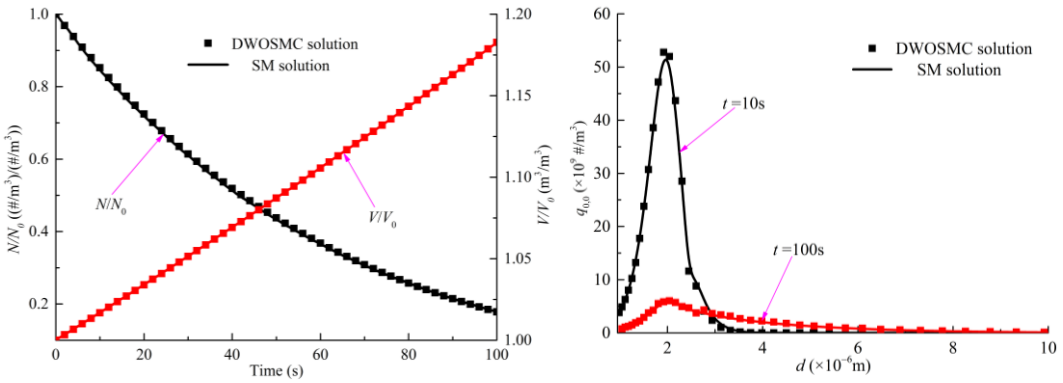

(a) (b)

Figure 5.10 Time evolution of (a) N/N_0 and V/V_0 and (b) particle number distributions obtained from the SM (solid line) and DWOSMC method (scattered solid points) for Case V (Liu and Chan, 2018b).

Figure 5.11 shows the particle volume density distributions of components, A and B for the simulation times of 10 s and 100 s. The peak diameter of $q_{1,0}$ and $q_{0,1}$ tends to be larger while the peak diameter of $q_{0,0}$ distribution does not change much as shown in Figure 5.10(b). As the time period reaches 100 s, the distributions of $q_{1,0}$, and $q_{0,1}$ become broader and more closely reflect normal distributions. The results obtained from the DWOSMC method are in excellent agreement with those obtained from the SM.

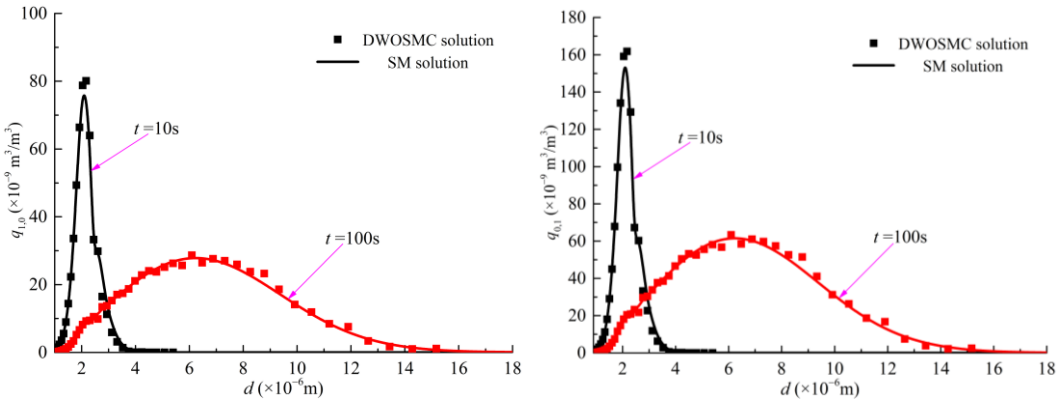

(a) (b)

Figure 5.11 Particle volume density distributions of (a) $q_{1,0}$ and (b) $q_{0,1}$ for simulation times t =10 s and t =100 s obtained from the SM (solid line) and DWOSMC method (scattered solid points) for Case V (Liu and Chan, 2018b).

5.3.4 Two-component coagulation and condensation processes and the free molecule regime case

Coagulation and condensation processes are considered to occur in a free molecule regime (where the diameter of particles is smaller than the mean free path of air) for Case VI. In the free molecule regime, the coagulation kernel is determined as Equation (3-5).

The initial particle size distribution satisfies a normal distribution in Equation (5-16), and the compositions of components, A and B are different. The initial total particle number is $N_0 = 10^{12}/\text{m}^3$ and the initial average particle volume is $v_0 = 3\times10^{-18}$ m^3 while the volumes of components, A and B are $v_{A0} = v_0/3$ and $v_{B0} = 2v_0/3$, respectively. The standard deviation, σ is 1×10^{-18} m^3. The linear condensation kernels of components, A and B are given by $I_A = \sigma_A v_A$, $\sigma_A = 1\times10^{-3}$/s, $I_B = \sigma_B v_B$ and $\sigma_B = 2\times10^{-3}$/s, respectively. A simulation period of 100 s is used.

Figure 5.12 shows the time evolution of dimensionless particle number density, N/N_0 and total particle volume, V/V_0 as well as the particle number distribution of $q_{0,0}$ for Case VI. For N/N_0 and V/V_0, the results obtained from the DWOSMC method and SM are in excellent agreement with one another as shown in Figure 5.12(a). In Figure 5.12(b), the distribution curve of $q_{0,0}$ is steep and narrow for a simulation period of 10 s, and the distribution curve of $q_{0,0}$ is broader and much more gradual as the simulation time reaches 100 s. At a simulation time of 10 s, some fluctuations are observed at the peak value of $q_{0,0}$. However, when the simulation time reaches 100 s, the peak diameter of $q_{0,0}$ is larger, the distribution of $q_{0,0}$ is normal with slight fluctuations, and the results obtained from the DWOSMC method and SM agree well with one another.

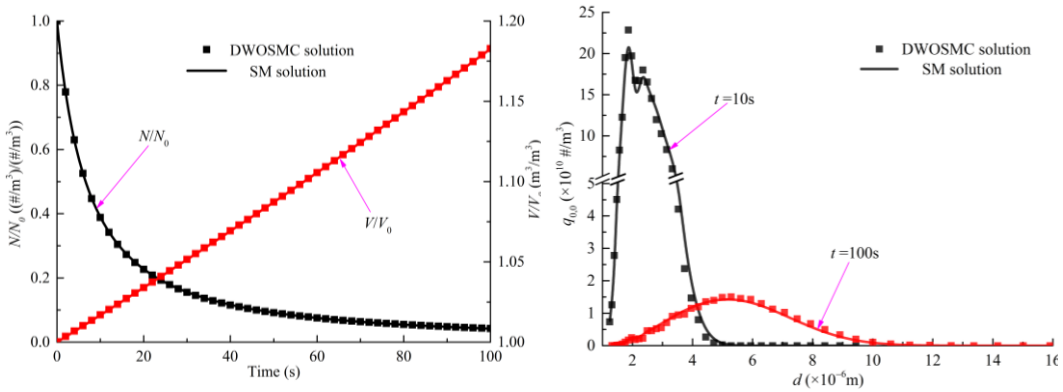

(a) (b)

Figure 5.12 Time evolution of (a) N/N_0 and V/V_0 and (b) particle number distributions obtained from the SM (solid line) and DWOSMC method (scattered solid points) for Case VI (Liu and Chan, 2018b).

Figure 5.13 shows the particle volume density distributions for components A and B for simulation times of 10 s and 100 s. Figure 5.13(a) shows that the distribution of $q_{1,0}$ tends to be broader and that the peak diameter of $q_{1,0}$ is larger. Similar variations are found for component B as shown in Figure 5.13(b), though the value of $q_{0,1}$ is larger than $q_{1,0}$ due to the use of different condensation kernels for

components A and B. The distributions of $q_{1,0}$ and $q_{0,1}$ obtained from the DWOSMC method and SM agree well with one another.

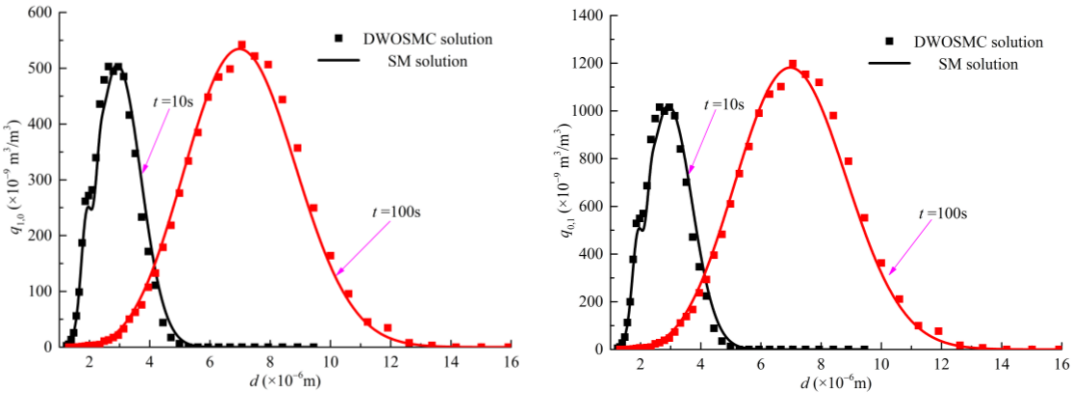

(a) (b)

Figure 5.13 Particle volume density distributions of (a) $q_{1,0}$ and (b) $q_{0,1}$ for simulation times t= 10 s and 100 s obtained from the SM (solid line) and DWOSMC method (scattered solid points) for Case VI (Liu and Chan, 2018b).

The normalized combined number density distribution of A-component and B-component (i.e., the bivariate compositional distribution) is defined as follows:

$$n_d = 100n(v_A, v_B, t)/N_0 \tag{5-17}$$

In Case VI, the bivariate compositional distributions for different simulation times, t are shown in Figure 5.14. The contour plot of the normalized bivariate compositional distribution function is mostly positioned in the diagonal area based on the dimensionless coordinates of v_A/v_0 and v_B/v_0. As simulation time increases from t = 20 s to t = 100 s, the normalized bivariate compositional distribution function tends to be smaller but distributes across a larger region with respect to compositional particle volumes.

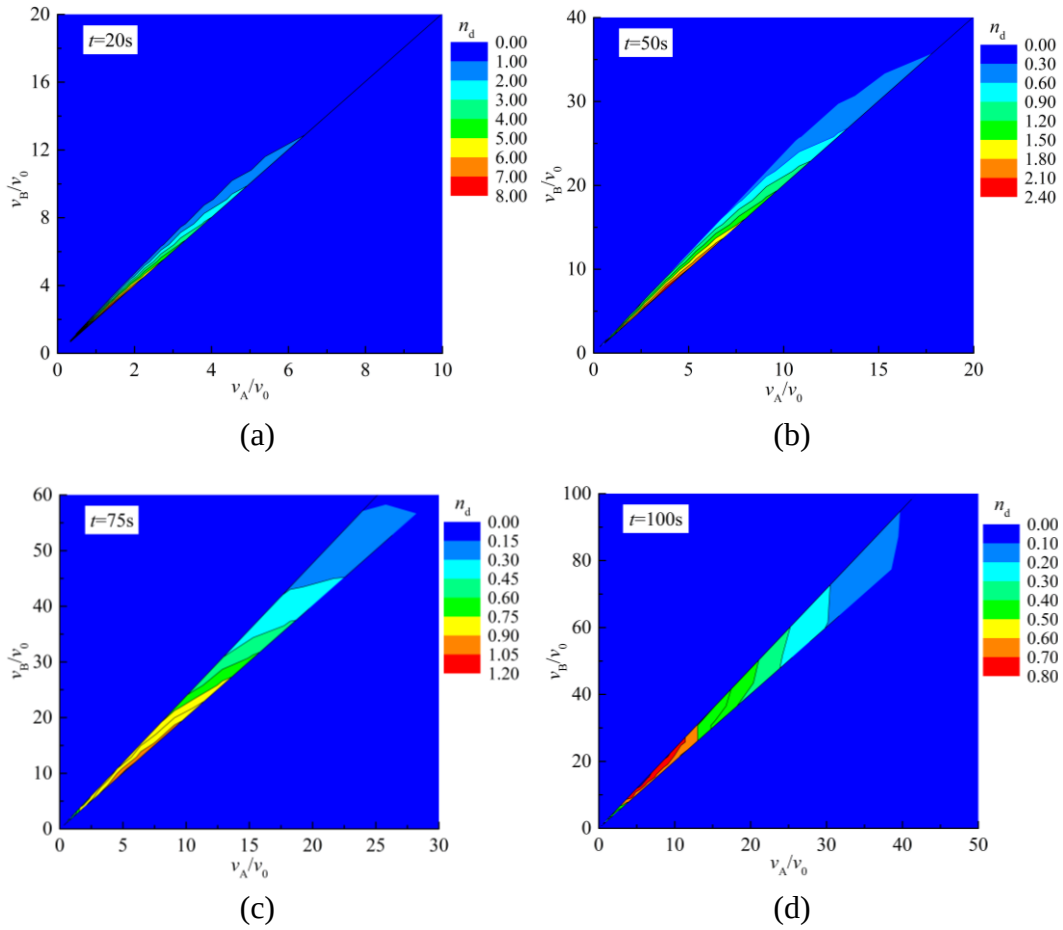

Figure 5.14 Dimensionless bivariate compositional distributions at different simulation times, t obtained from the DWOSMC method for Case VI (Liu and Chan, 2018b).

5.3.5 Computational accuracy and efficiency analysis

To evaluate the computational accuracy and efficiency of the newly proposed and developed multi-component DWOSMC method in the present study, the calculated relative error, ε (%) according to Equation (4-11) (here A_0(t) is the value obtained from the sectional method) is shown in Figure 5.15. The normalized computation times, τ according to Equation (5-11) (i.e., the reference value is the computational time of Case I obtained from the SM) for the studied cases are listed in Table 5.1. In Figure 5.15, maximum relative errors range within 0.8% for Cases I to IV and 1.2% for Cases V and VI, respectively. The results show that this new

DWOSMC method is computationally accurate and the relative errors generated are very small even in complex two-component systems involving coagulation and condensation processes. In addition, the relative errors obtained from two-component Cases II to VI do not tend to be significantly larger than those of one-component Case I. Furthermore, it is well known that the SM is generally more computationally powerful than the MC method for one-component systems (e.g., for Case I). When the two methods are further extended to consider two-components, Table 5.1 shows that τ of the DWOSMC method generates much smaller values than the SM for most of the two-component cases. This is the case because when considering more component information, the programming algorithm for the SM correspondingly becomes more complex while the MC method does not. Hence, it is concluded that the newly proposed and developed multi-component DWOSMC method is superior to the SM in terms of its computational efficiency in addressing complex multi-component problems.

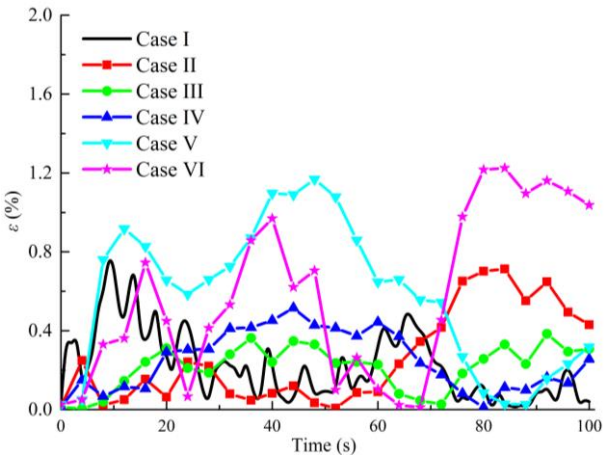

Figure 5.15 Time evolution of the relative errors, ε (%) for N/N_0 obtained from the DWOSMC method for different cases (Liu and Chan, 2018b).

Table 5.1 Normalized computation times, τ obtained from different cases using the SM and DWOSMC method (Liu and Chan, 2018b).

τ / Case	Methods	
	SM	DWOSMC
I	1.0	5.4
II	63.5	22.4
III	101.0	24.2
IV	115.1	24.4
V	177.2	25.5
VI	190.1	28.7

5.4 Summary

A differentially weighted operator splitting Monte Carlo (DWOSMC) method is further proposed and developed to simulate two-component aerosol dynamics in the present study. Compared to traditional Monte Carlo (MC) methods, the multi-component DWOSMC method proposed in the present study adopts "different weights" which is more suitable for obtaining the compositional distributions of particles, especially for multi-component systems. In addition, the operator splitting technique renders it applicable and more efficient method to couple the stochastic MC method with the deterministic integration method.

Different initial size distribution functions and initial compositional distributions of particles are studied under various regimes of simultaneous aerosol coagulation and condensation that include three cases involving constant coagulation kernel, one case involving sum coagulation kernel and one case involving free molecule coagulation kernel, respectively. For all of these cases studied, the dimensionless particle number density, total particle volume, particle

number distribution and component related particle volume density distributions are examined, and the results obtained from the DWOSMC method agree well with those obtained from the SM.

The present results and findings show that the newly proposed and developed multi-component DWOSMC method is more computationally accurate and efficient than traditional non-weighted MC methods. Furthermore, the SM is more computationally efficient than the DWOSMC when applied to one-component aerosol simulation systems while the DWOSMC tends to be more computationally efficient when applied to two-component aerosol simulation systems. This is the case because considering more than one form of component information does not significantly increase the complexity of the MC algorithm while much higher levels of complexity are required to use the SM algorithm to simulate more than one component of aerosol dynamics. With such high levels of computational efficiency and accuracy based on the specific data and evidence obtained, the newly developed multi-component DWOSMC method can predict not only particle size distributions, but can also determine component-related particle volume density and bivariate compositional distributions.

Chapter 6 Simulation of a spatially inhomogeneous particle-laden turbulent flow

6.1 Introduction

The phenomenon of particle-laden turbulent flows is quite common in a broad range of scientific and engineering applications including atmospheric dispersion of pollutants (Chan et al., 2018a, 2010, 2008; Zhong et al., 2018), fluidized beds (Ayeni et al., 2016; Clarke et al., 2018; Xu et al., 2000), soot particles in combustion chambers (Lucchesi et al., 2017; Zhao et al., 2018; Zucca et al., 2006), aerosol reactors (Chan et al., 2018b; Liu and Chan, 2017b; Yu et al., 2008b), indoor airborne particles emitted in cooking process (Lai and Chen, 2015; Wang et al., 2018) and so on.

Most of the previous studies focused on particle-laden flows in simplified configurations. However, in some realistic geometry, the irregular flow structure of channels may induce a large inhomogeneous flow field, which further affects the concentration distribution of the dispersed particles. Focusing on inhomogeneous flows, Vincont et al. (2000) conducted experiments in both water channel and wind tunnel where the passive scalars were released from the line source slot into the near-wake flow behind a square rod obstacle in order to obtain the properties of the preferential concentration fields of passive scalars. In the present study, the numerical simulation is based on the wind tunnel experiments (Vincont et al., 2000), and the significance of two-way coupling effect on particle-fluid interactions is examined for a wide range of particle Stokes numbers.

The flow structure of a turbulent particle-laden injection downstream of a square rod obstacle from the experimental study of Vincont et al. (2000) is simulated for the particle Stokes numbers ranging from 0~100. It is the first Eulerian-Lagrangian numerical simulation of the mentioned wind tunnel experiments by using two-way coupling method. Firstly the numerical results are validated and compared with available experimental results (Vincont et al., 2000). Then, the effects of two-way coupling method between the dispersed and continuous phases, turbulent dispersion and Reynolds number based on the characteristic length of a square rod obstacle on the particle preferential concentration distribution are examined for different particle Stokes number cases.

6.2 Numerical Methodology

6.2.1 Eulerian equations for the continuous gas phase

The transport of the continuous fluid phase is governed by the well-known Navier-Stokes (N-S) equations that describe the conservation of mass, momentum and energy, and are presented by the following equations in incompressible fluid flows:

$$\frac{\partial u_i}{\partial x_i}+\frac{\partial u_j}{\partial x_j}=0 \tag{6-1}$$

$$\frac{\partial u_i}{\partial t}+\frac{\partial u_i u_j}{\partial x_j}=-\frac{1}{\rho}\frac{\partial p}{\partial x_i}+\nu_f\frac{\partial^2 u_i}{\partial x_j \partial x_j}+f_P \tag{6-2}$$

where u_i is the velocity, p is the pressure, ρ is the density and ν_f is the kinematic viscosity. f_P represents the force applied by the dispersed solid particles because of interphase coupling. If one-way coupling effect is considered, i.e., the influence of the dispersed phase on the carrier fluid phase is neglected, hence the value of f_{p} in

Equation (6-2) should be zero. Otherwise, when two-way coupling is considered, f_{p} is calculated according to Equation (6-3).

$$f_{\mathrm{p}} = -\frac{1}{m_{\mathrm{f}}}\sum_{k=1}^{M} f_{\mathrm{p}k} \tag{6-3}$$

where $f_{\mathrm{p}k}$ is the drag force acting on particle, k that is described in Equation (6-5), M is the number of particles that are tracked within the computational cell and m_{f} is the mass of fluid within the computational cell.

6.2.2 Lagrangian particle tracking

The dispersed particle phase is described by a Lagrangian Monte Carlo method, and the governing equation of the position and velocity of a particle is given by Newton's second law of motion which is written as (Fan et al., 1997; Sommerfeld, 2001):

$$\frac{\mathrm{d}x_{P,i}}{\mathrm{d}t} = u_{P,i} \tag{6-4}$$

$$\frac{\mathrm{d}u_{P,i}}{\mathrm{d}t} = \frac{3}{4}\frac{\rho}{\rho_P d_P} c_{\mathrm{D}}\,(u_i - u_{P,i})|\vec{u} - \vec{u_P}| + f_s \tag{6-5}$$

where x_P is the position, u_P is the velocity of the particles, u is the velocity of the continuous gas phase and d_P is the diameter of the dispersed particles. The first term in the right-hand side of Equation (6-5) represents the drag force that the carrier flow imposes on the particles. The drag coefficient C_D is formulated by (Zhu et al., 2007),

$C_D = 24(1+0.15Re_P^{0.687})/Re_P$ when $Re_P<1000$ and

$$C_D = 0.44 \ , \ Re_P \geq 1000 \tag{6-6}$$

where Re_P is the relative Reynolds number,

$$Re_P = \frac{d_P|\vec{u}-\vec{u_P}|}{v_f} \tag{6-7}$$

In Equation (6-5), f_s represents the contributions from forces other than drag force, for example, gravity, lift, Basset, etc. It is observed that the Stokes drag is the dominant force for a large scale of density ratios between the dispersed particles and the carrier gas flows, the effect of other forces imposed on particles is only about 1% (Armenio and Fiorotto, 2013). Therefore, the force considered in the present study is only the drag force.

The corresponding Stokes number of particles is defined as,

$$St = \tau_P/\tau_f \tag{6-8}$$

where $\tau_P = \rho_p d_p^2/(18\rho_f v_f)$ is the particle relaxation time and $\tau_f = L/u$ is the flow response time where L is the characteristic length of the carrier gas flow and the characteristic length of the obstacle, h is used for the present study. The Stokes number has a significant influence on the interaction between the particles and the carrier flows. When the particle Stokes number is very low (e.g., smaller than 0.01), the dispersed particles follow perfectly the streamlines of fluid flow. However, when the particle Stokes number is high (e.g., larger than 10), the effect of fluid flow on particles becomes weaker, and particles tend to follow the trajectory of the original injection particles. From Equation (6-8), it can be seen that under the condition of predetermined flow structure and fluid material, the Stokes number is only a function of particle size and the density ratio of the particles to the gas. In the present study,

the two-way coupling effects on both the preferential concentrations of particles and the fluid flow field is studied in a wide range of Stokes numbers.

Considering coupling the motion of dispersed particles and the fluid phase, many previous studies focused on one-way coupling effect, in such case, the influences of dispersed particles on the carrier flows are supposed to be negligible. Thus, the numerical simulation of the transport of particles can be calculated on the basis of pre-existing fluid flow fields which can save much computational time and computer memory. However, in many cases, especially in cases where the volume fraction of dispersed particles, φ_v is larger than 10^{-4}, the effects of particles on the continuous phase cannot be neglected. The interaction between these two phases may affect the preferential concentration of the particles. When the volume fraction, φ_v continues to increase, a four-way coupling method should be considered which implies the interaction effect between the particles (e.g., particle-particle collision) should also be calculated.

6.2.3 Particle-particle collision simulation

In the present study, four-way coupling (particle-particle collision) effect is observed in the validation case that is compared with the experimental results (Vincont et al., 2000). A Lagrangian Monte Carlo method is used to calculate the solid particles, because of its stochastic and statistical characteristics, more particles in the simulation system implies more computer memories and computational time consumption are needed. To overcome the conflicts of large number of real particles and the potential limitation of computer capacity with enhancing computational accuracy, the "weighted" simulated particles are used, i.e., one simulated particle represent w_i (the weight) real particle, which is a quite popular concept of Monte

Carlo simulation to simulate complex particle-fluid systems to avoid the need for extremely high computer performance.

Herein, the simulation of the particle-particle collisions is based on probabilistic rules. The occurrence probability of collision between two particles, *i* and *j* is calculated based on the theory of O'Rourke (1981), which is based on the relative velocity, sizes and the weights of the two collided particles, and is written as Equation (6-9),

$$P_{\mathrm{col},ij} = \exp(-C_{ij}^{'}) \tag{6-9}$$

where $C_{ij}^{'}$ is the normalized collision rate of the simulated particles.

$$C_{ij}^{'} = w_{\min} C_{ij} \tag{6-10}$$

where $w_{\min}$ is the smaller weight of the two collided particles and C_{ij} is the collision kernel as follows:

$$C_{ij} = \frac{\pi}{4}(d_i+d_j)^2 |u_i-u_j| \frac{\delta t}{V_{\mathrm{cel}}} \tag{6-11}$$

where d_i, d_j, u_i and u_j are the diameter and the velocity of the collided particles, *i* and *j*, respectively. δt is the time-step, V_{cel} is the volume of the computational grid which contains those two particles. Herein, it is assumed that only particles in the same computational grid can collide with each other.

A random number from a uniform distribution between zero and one，r_1 is generated to evaluate the occurrence of collision event between particles, *i* and *j*. If Equation (6-12) is satisfied, then collision will take place.

$$r_i \le P_{\mathrm{col},ij} \tag{6-12}$$

If a successful collision is observed, the next step is to deal with the collision event of those two particles, *i* and *j*.

In the O'Rourke's collision model, the treatment of collision event between particles, *i*, and *j* is based on the conservation of momentum. The calculations are as follows:

The total momentum of these two particles is,

$$\boldsymbol{m}_r = m_i\boldsymbol{u}_i + m_j\boldsymbol{u}_j \tag{6-13}$$

where $\boldsymbol{u}_i$, $\boldsymbol{u}_j$, $\boldsymbol{u}_i'$ and $\boldsymbol{u}_j'$ are the velocity vector of particles, *i* and *j* before and after the collision event, respectively.

After collision, the velocity vectors of these two collided particles are calculated as (O'Rourke, 1981),

$$\boldsymbol{u}_i' = [\boldsymbol{m}_r + m_j(\boldsymbol{u}_i - \boldsymbol{u}_j)g_f]/(m_i + m_j) \tag{6-14}$$

$$\boldsymbol{u}_i' = [\boldsymbol{m}_r + m_j(\boldsymbol{u}_i - \boldsymbol{u}_j)g_f]/(m_i + m_j) \tag{6-15}$$

where g_f is the collision restitution coefficient and is related to the diameter of particles and the impact parameter. For a perfectly elastic collision event, g_f is equal to 1, for a perfectly inelastic collision event, g_f is equal to 0 where the detailed information can be referred to O'Rourke (1981). In the present study, g_f is randomly generated between 0 and 1.

6.2.4 Turbulent dispersion model

Turbulent flows are unsteady and chaotic, the velocity of gas varies significantly and irregularly both spatially and temporally. In consequence, particles

suspended in turbulent flow would also have random motions because of being perturbed.

In the present study, the average velocity of the continuous fluid flow is solved by Reynolds-Averaged Navier-Stokes Equations (RANS) equations. In order to take the turbulence effect into consideration, a stochastic fluctuation should be added into the calculation of the fluid flow velocity.

The real velocity of the fluid flow is described as,

$$u = \bar{U} + u' \tag{6-16}$$

where u is the transient velocity of the fluid, $\bar{U}$ is the mean velocity which can be calculated by RANS turbulence model and u' is the fluctuation velocity.

The velocity fluctuation of fluid flow is described by the discrete random walk (DRW) model (Ghahramani et al., 2014; Katz et al., 1999) and is calculated as,

$$u' = \lambda \sigma_i \tag{6-17}$$

where λ is a number with Gaussian distribution with zero mean and unit variance.

In isotropic flows,

$$\sigma_i = (\frac{2}{3}k)^{1/2} \tag{6-18}$$

where k is the time-averaged turbulent energy.

In the present study, the flow is anisotropic where σ_i is described as follows,

$$\sigma_1 = \frac{0.40y^+}{1+0.0239(y^+)^{1.496}} u^* \tag{6-19}$$

$$\sigma_2 = \frac{0.0116(y^+)^2}{1+0.203y^+ +0.00140(y^+)^{2.421}}u^* \tag{6-20}$$

$$\sigma_3 = \frac{0.19y^+}{1+0.0361(y^+)^{1.322}}u^* \tag{6-21}$$

where u^* is the friction velocity of fluid flow.

In anisotropic and inhomogeneous flows, a preferred method of modeling the particle dispersion in turbulent flows is the continuous random walk (CRW) model that can use a discrete Markov chain to correlate the velocity fluctuation of fluid flow with that of the previous time-step along the path of particles (Bocksell and Loth, 2006; Iliopoulos and Hanratty, 1999; MacInnes and Bracco, 1992; Rybalko et al., 2012). The discrete Markov chain for the velocity fluctuation is written as (Bocksell and Loth, 2006; Rybalko et al., 2012),

$$u'(t+\Delta t) = \exp(\frac{-\Delta t}{\tau_L})u'(t) + \sqrt{1\text{-}\exp(\frac{-2\Delta t}{\tau_L})}\sigma_i\lambda(t) + \delta u' \tag{6-22}$$

where τ_L is the Lagrangian time scale, $\delta u_i = \Delta t(\overline{u_j \frac{\partial u_i}{\partial x_j}})$ is the drift correction for inhomogeneous turbulence (Bocksell and Loth, 2006, 2001).

In the CRW model, the term on the left hand of Equation (6-22) is the instantaneous fluid velocity perturbation at time of $t+\Delta t$; the first term on the right hand of Equation (6-22) is the damping term that is related to the fluid velocity perturbation at the previous time-step where τ_L is the Lagrangian time scale; the second term on the right hand of Equation (6-22) is the stochastic term where $\lambda(t)$ is a continuous random variable that can be specified to have a Gaussian distribution with a variance of unity and σ_i is the root mean square velocity described by

Equations (6-19) to (6-21) for different directions in anisotropic flows; and the third term on the right hand of Equation (6-22), $\delta u'$ is the drift correction for inhomogeneous turbulence, and can be described as (Bocksell and Loth, 2006; 2001), $\delta u_i' = \Delta t(\overline{u_j' \frac{\partial u_i'}{\partial x_j}})$.

In the present study, the CRW model described by Equation (6-22) is used for calculating the fluctuating velocity component.

6.3 Numerical Simulation Setup

The Lagrangian particle tracking codes (Fan et al., 1997; Sommerfeld, 2001) are coupled into the Reynolds Averaged Navier-Stokes (RANS) based *k-ε* turbulence model (Ghahramani et al., 2014; Rossi and Iaccarino, 2009) to simulate the motion of dispersed particles, and the steady and transient states of the flow field. The convergence criterion for the relative residual of the velocity and continuity and other variables is set as 10^{-6} (Chan et al., 2018b).

6.4 Results and Discussion

The numerical validation and implementation of the developed and coupled codes are carried out on the same geometry and experimental data from the previous experimental study by Vincont et al. (2000), and the wind tunnel case is selected as the initial conditions of numerical validation.

6.4.1 Configuration and model description

The numerical simulation is conducted on a wind tunnel case where there is a long horizontal square rod mounted on the flat plate that significantly affects the

flow field and the preferential concentration of dispersed particles behind the obstacle. A two-dimensional square rod is fully immersed in a turbulent-boundary layer. The main flow is air from the ambient atmosphere, and incense smoke with particles is seeped into the downstream of the obstacle. The configuration of the experimental setup inside wind tunnel is shown in Figure 6.1 where the particles are released from the line source slot into the near-wake flow behind a square rod obstacle on the flat plate.

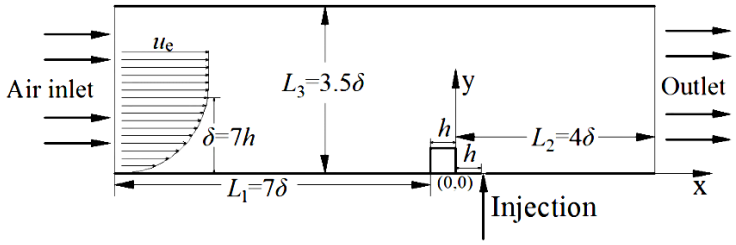

Figure 6.1 A sketch map of the wind tunnel with a mounted horizontal square rod obstacle and of the computational domain.

According to the experimental setup of Vincont et al. (2000), a horizontal square rod obstacle has a cross-section of 0.01 m × 0.01 m with an aspect ratio of 50, the main flow is a free-stream flow with a speed of u_e = 2.3 m/s with a cross-section area of 0.5 m × 0.5 m which is equivalent to the Reynolds number of the square rod obstacle, Re_h (which is $\mathrm{Re}_h = uh/v$) ≅ 1500. The boundary layer thickness, δ in this case studied is about 0.07 m, the square rod obstacle is mounted at $L_1 = 7\delta$ downstream of the air inlet flow, and the free surface is 3.5δ above the flat plate, in order to guarantee a stabilized boundary layer in the laminar-turbulent transitional flow condition. The smoke flow with particles is released from the line source slot with a speed of $u_p/u_e \cong 0.04$ through a slot width of 0.002 m at 1h downstream of the square rod obstacle.

6.4.2 Numerical validation

6.4.2.1 Grid independence and gas flow field validations

As the distributions and dynamic behaviors of particles are to a great extent affected by the gas flows, one critical factor that determines the accuracy of numerical simulation of fluid flow is the grid density. In the present study, three different grid densities (coarse meshes: 49975 cells, medium meshes: 112000 cells, and fine meshes: 199900 cells) are used to verify the grid independence. The velocity distribution profiles at upstream, $x/h = -4$ and downstream, $x/h = 4$ of the square rod obstacle for different grid density cases are shown in Figure 6.2, where $x/h = 0$ locates at the rear end of the square obstacle. It could be well observed that the velocity distribution profile calculated from the coarse mesh case deviates slightly from those medium and fine mesh cases, and no obvious differences can be seen from the results obtained between medium and fine mesh cases. Therefore, the grid density with 112000 cells is selected to perform the numerical simulations in consideration of both computational accuracy and efficiency.

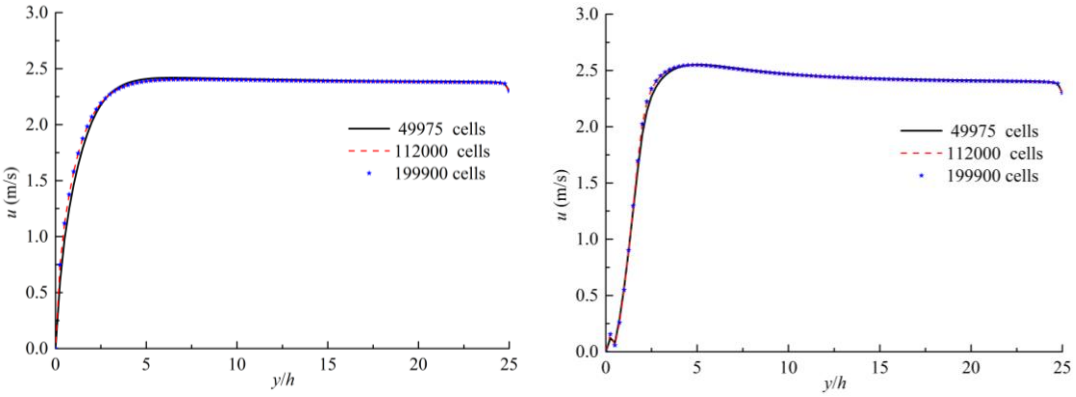

Figure 6.2 Effect of grid densities on velocity distribution profiles at (a) $x/h = -4$ and (b) $x/h = 4$.

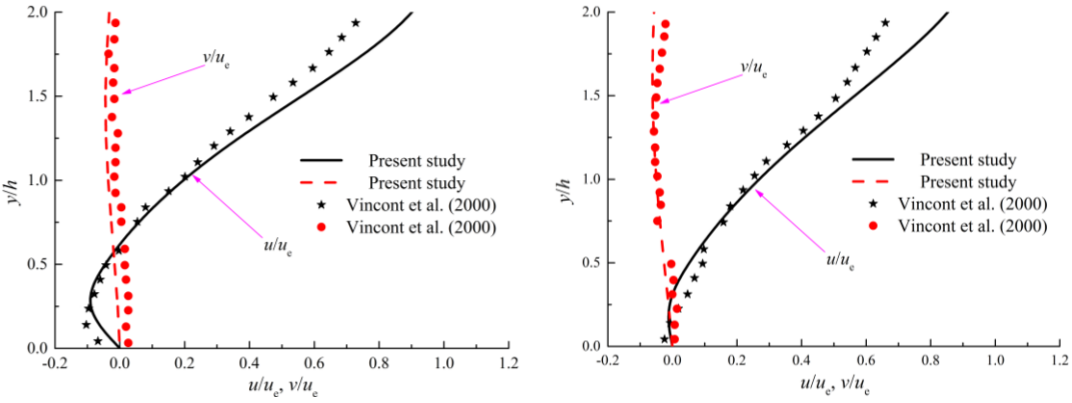

(a) (b)

Figure 6.3 Normalized velocity distribution profiles at (a) x/h = 4 and (b) x/h = 6.

In Figure 6.3, the normalized velocity distribution profiles in the streamwise direction, u/u_e, and wall-normal direction, v/u_e, are shown both at the position of x/h = 4 and x/h = 6. The numerical simulation results are compared with the experimental results available from Vincont et al. (2000). Considering the measurement errors and fluctuations, the numerical results coincide with the experimental results with some deviations

6.4.2.2 Particle concentration distribution validation

Particles are released from the line source slot at time, t_0 = 0 when the gas flow field is already calculated to reach a steady state. In order to ensure the similarity with experiments, the Lagrangian particle injection is set to be the same with Vincont et al. (2000). The released smoke is carrying particles with mean diameter of 0.9 μm and mass flux of 7.8×10^{-6} kg·s^{-1}m^{-1}, in which case, the initial particle number concentration is $C_0 \sim \mathcal{O}(\times10^{16}$ m$^{-3})$ and the initial particle volume fraction is $\varphi_v \sim \mathcal{O}(\times10^{-4})$ at the inlet. In this numerical validation case, the particle Stokes number is around 0.0004, the sampling period is $t_s \sim 200h/U_e$. Three different

coupling methods (i.e., one-way coupling, two-way coupling and four-way coupling methods) are studied and compared with the experimental results of Vincont et al. (2000).

The normalized mean particle concentration along lines of x/h = 4 and x/h = 6 are shown in Figure 6.4(a) and (b), respectively. It can be observed that the particles mostly locate inside the region of y/h = 3, and particle accumulation reaches maximum at $y/h \cong$ 1 at both the positions of x/h = 4 and x/h = 6. The tendency of particle concentration distribution of the numerical simulation results agrees with the experimental results, and it is apparent that when only one-way coupling is considered, the particle concentration distribution curve obtained from numerical simulation is far from the experimental results, and when two-way or four-way coupling is considered, the numerical simulation results coincide with the experimental results. Therefore, considering only one-way coupling between the continuous fluid phase and the dispersed particles will result in large errors, and four-way coupling seems not quite necessary in this case.

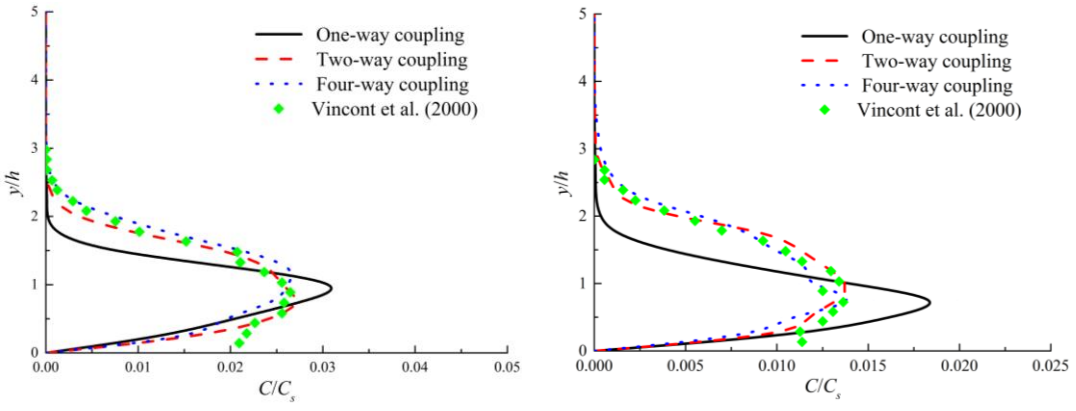

Figure 6.4 Normalized particle concentration distribution profiles at (a) x/h = 4 and (b) x/h = 6.

6.4.3 Particle field distribution analysis and two-way coupling effect

For a deeper understanding of the difference observed from Figure 6.4 between the one-way coupling and two-way coupling effects, the transient particle field distributions are shown in Figure 6.5(a) and (b).

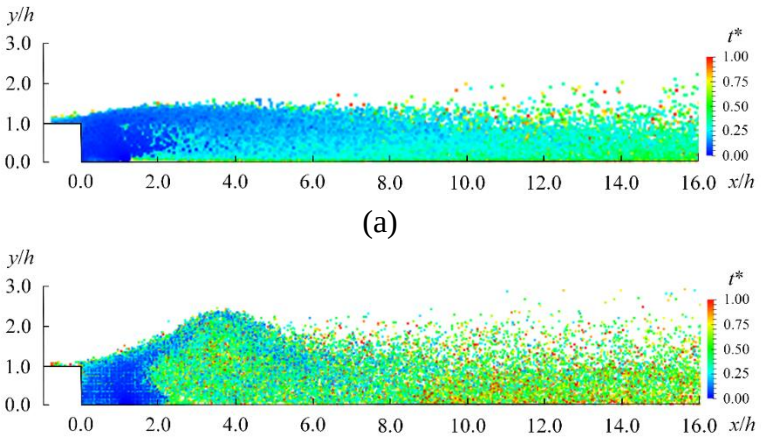

Figure 6.5 Transient particle field distribution at t^*= 1 (a) one-way coupling case and (b) two-way coupling case.

In Figure 6.5, for one-way coupling case, the particles distribute mostly within the region of y/h = 1.5, and then distribute evenly along the streamline direction. While for two-way coupling case, as shown in Figure 6.5(b), there is a peak at the position of about x/h = 4, which implies that the dispersion characteristics of the particles become stronger, thus the particle number concentration becomes smaller than one-coupling case, which can explain the phenomenon observed in Figure 6.4. Since the effect of turbulent dispersion is considered in those two cases, particles tend to locate everywhere in the wake region randomly behind the square rod obstacle, and the particle dispersion pattern is not distinct**.** Therefore, in order to further investigate the difference between one-way and two-way coupling cases, the stochastic dispersion model is then turned off for both cases, and the transient

particle field distribution at time period of $t^* = t/t_s = 0.1$, 0.2, 0.3, 0.4, ,0.6, 0.8 and 1 are given in Figure 6.6 for both cases.

One-way coupling case | Two-way coupling case

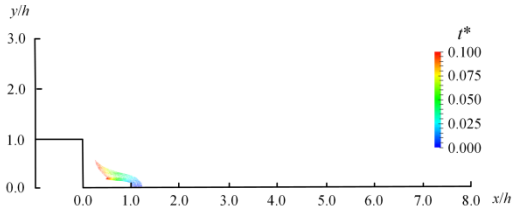

(a) $t^* = 0.1$

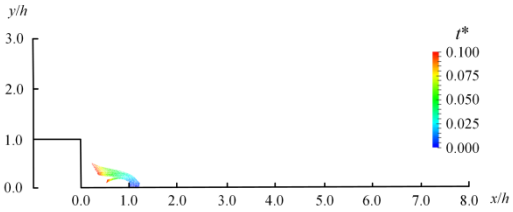

(b) $t^* = 0.1$

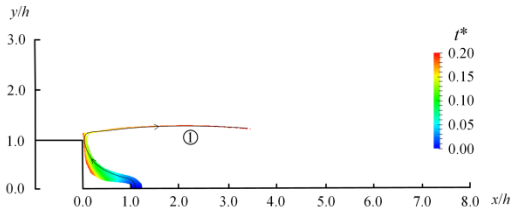

(c) $t^* = 0.2$

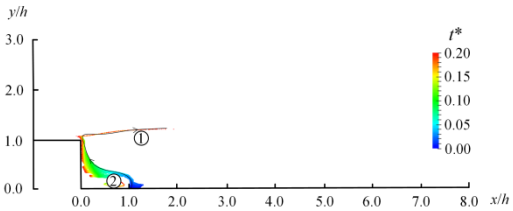

(d) $t^* = 0.2$

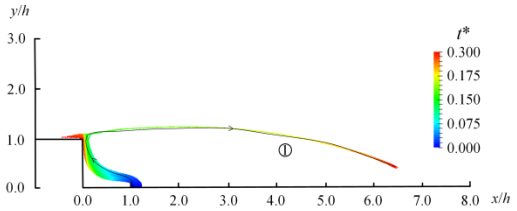

(e) $t^* = 0.3$

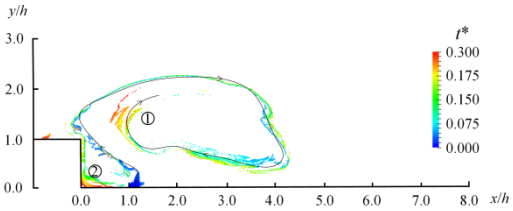

(f) $t^* = 0.3$

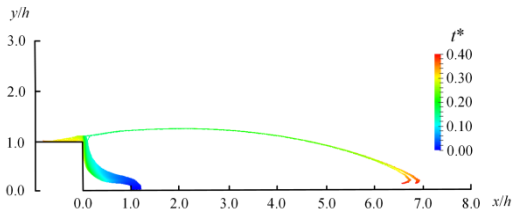

(g) $t^* = 0.4$

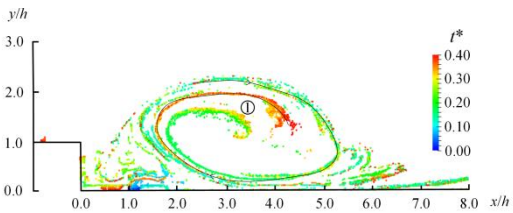

(h) $t^* = 0.4$

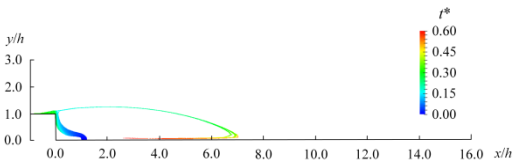

(i) $t^* = 0.6$

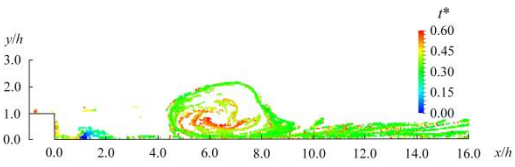

(j) $t^* = 0.6$

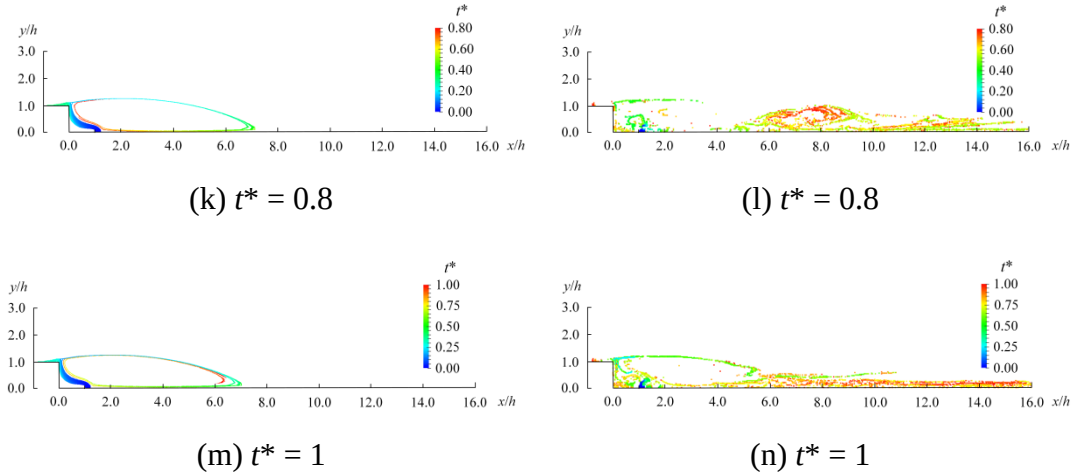

(k) t^* = 0.8 (l) t^* = 0.8

(m) t^* = 1 (n) t^* = 1

Figure 6.6 Transient particle distributions at different time periods for one-way and two-way coupling cases.

From Figure 6.6(a) and (b), the particle distributions at time t^* = 0.1 for one-way and two-way coupling cases do not have much difference. From Figure 6.6(c) and (d), the particles distribution at time t^* = 0.2 in one-way coupling case shows good consistency with the fluid flow, and particles move in the fluid flow direction. However, the particles in two-way coupling case distribute in two semicircular shapes: the first main semicircular shape at marked ① in Figure 6.6(d) is the same with the main fluid flow direction, which shows the particles that follow the flow streamline, similar to the semicircular shape in Figure 6.6(c). The second small semicircular shape at marked ② . In Figure 6.6(d) indicates that some of the particles do not perfectly follow the fluid flow direction of the continuous phase and are split away from the main flow streamline because of the two-way coupling effect.

From Figure 6.6(e) and (f), the particles distribution at time t^* = 0.3 in one-way coupling case does not change much. While for two-way coupling case, the semicircular shape at ① evolves into an approximately round circle, and the

particles in semicircular shape at ② tend to deposit close to the walls of the square obstacle.

For one-way coupling case, from time t^* = 0.4 to 1, it can be observed that the farthest position in the x-direction that the particles reach is around x/h = 7, after which the particles will change their directions, and move backward and form a vortex in the region between x/h = 0~7. For two-way coupling case, it can be observed that most particles move towards circular flow direction and fade away gradually, after which a new vortex comes into being as shown in Figure 6.6(n).

Furthermore, in the two-way coupling case, the effects of preferential particle concentration are obvious in both near- (i.e., corner) and far-wake regions of the square rod obstacle, while no particles can be found in both of these two regions in one-way coupling case.

The different particle distributions are because of different coupling methods which result in different flow structures and further affect the particle dispersion patterns. The flow fields of the continuous gas phase at different time periods are shown in Figure 6.7.

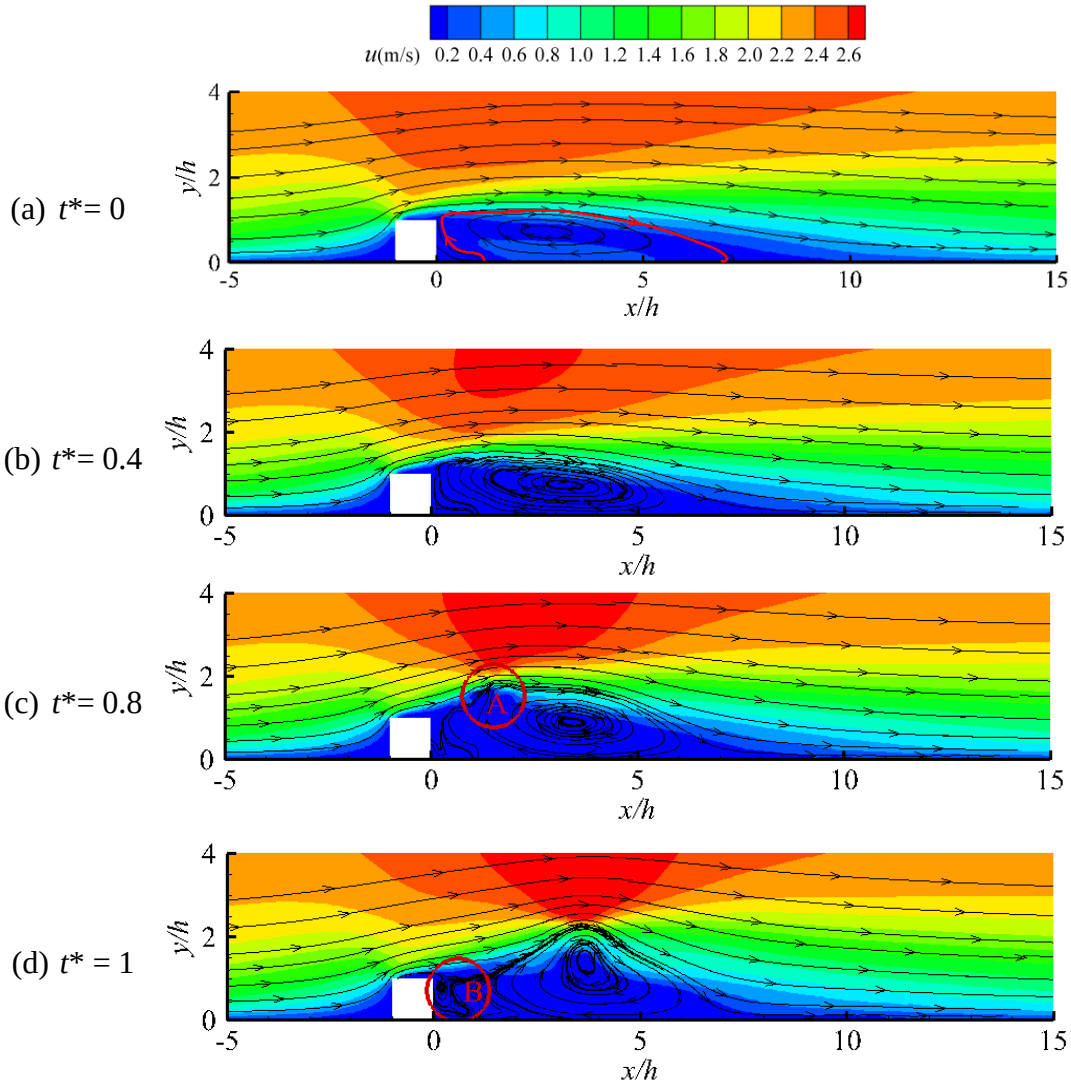

Figure 6.7 Transient flow fields at different time periods for two-way coupling case.

For one-way coupling case, the effect of particles on the continuous phase is ignored, so the flow field would stay the same when time advances as shown as Figure 6.7(a). It can be observed that there is a vortex behind the obstacle, and the flow streamline passing through x/h = 1 is the same with the particle field distributions as shown in Figure 6.6(m), which proves that in the one-way coupling case, the particles perfectly follow the motion of the carrier flow. While in the two-way coupling case, the fluid flow field is affected by the particles and the evolution

of flow field is shown in Figure 6.7(a) to (d). The vortex flow becomes larger and moves towards the main flow direction. The center of the vortex flow and the streamlines in regions, **A**, and **B** are significantly influenced by the particles, especially in **B** region, and small vortices are generated because of the wall deposition effect of the particles.

6.4.4 Particle Stokes number (St) effect

6.4.4.1 Instantaneous particle distribution

From Section 6.3, when the particle volume fraction, φ_v is approximately equal to 10^{-4} with the particle Stokes number at around 0.0004, the effect of solid particles on the continuous fluid flow field is obvious. In this section, the effect of particle Stokes number on the dispersion characteristics as well as two-way coupling effect are studied and the transient particle distributions at time, t_s for different Stokes numbers are shown in Figure 6.8.

From Figure 6.8(a) to (d), when the particle Stokes number is smaller than or equal to 0.01, the differences between the results of one-way and two-way coupling cases are shown clearly. In one-way coupling cases, particles only exist in the vortex flow and form a circular flow in the wake of the square rod obstacle. In two-way coupling cases, particles can be found in the far-field wake flow of square obstacle as well as in the near-wake flow (i.e., corner) behind the square obstacle in addition to the vortex region behind the square obstacle. This phenomenon is quite similar to what is observed in Figure 6.6(k) and (l). From Figure 6.8(e) to (l), when the Stokes number is higher than or equal to 0.1, the difference between one-way and two-way coupling cases on the particle distribution is not distinct.

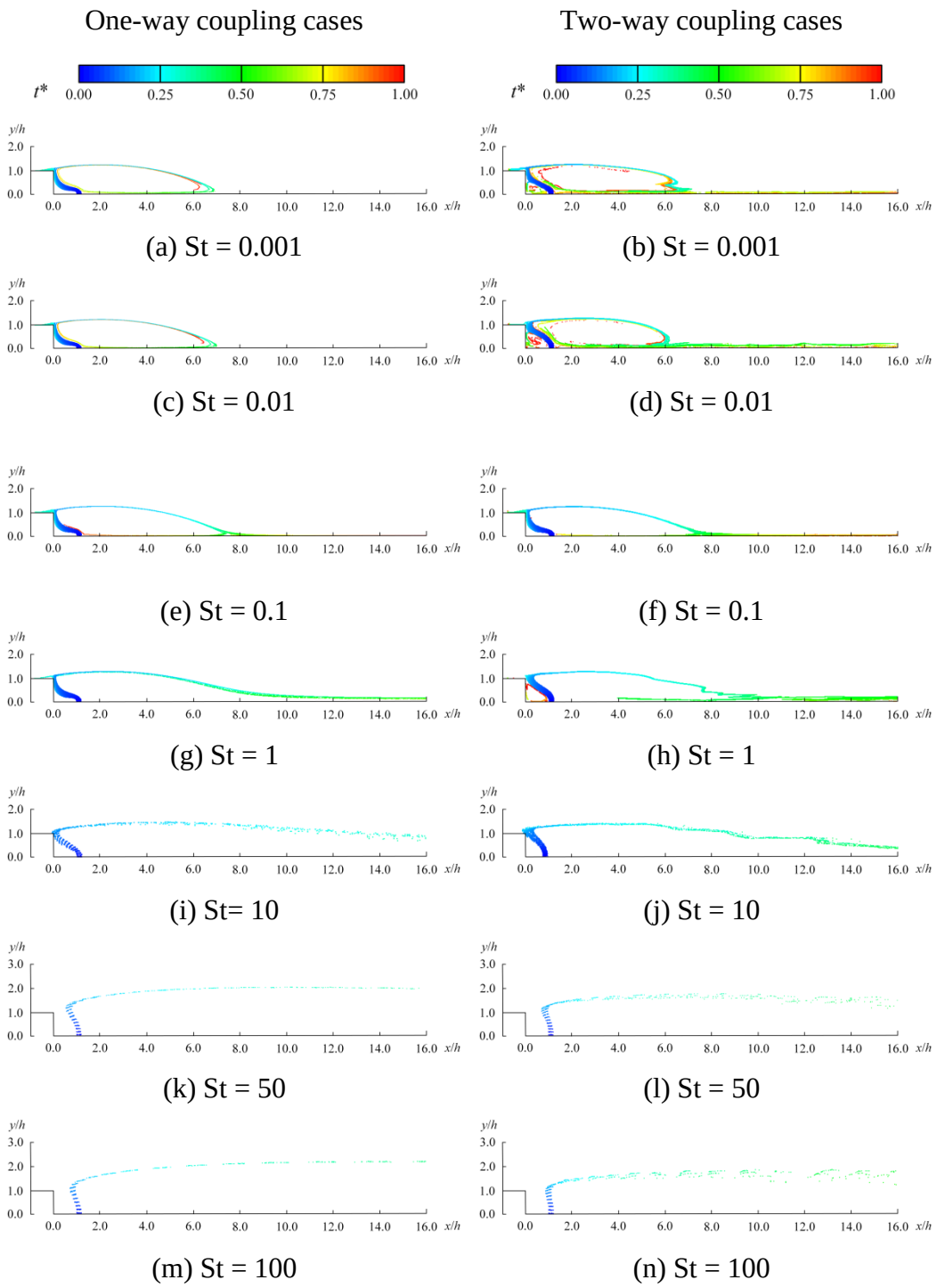

Figure 6.8 Effect of particle Stokes number on the instantaneous particle distribution for one-way and two-way coupling cases.

For the one-way coupling cases, when the particle Stokes number is smaller than or equal to 0.01 as shown in Figure 6.8(a), (c), (e), (g), (i) and (k), the particles completely follow the fluid flow direction of the continuous phase and only locate

in the vortex generated by the main fluid flow, and spread over the upper wall of the obstacle. When the particle Stoke number is 0.1, the particles start to split away at the end of the vortex, some particles move along the downstream direction while other particles continue to follow the vortex flow and change their velocity direction. When the particle Stokes number is higher than or equal to 1, the particles completely escape from the main vortex flow behind the obstacle. When the particle Stokes number continues to increase, the preferential concentration of particles changes significantly. There is no particle located in the upper wall of the obstacle when the particle Stokes number reaches 50. The trajectory of particles is nearly parallel to the lower wall of the square obstacle wake and the particles behind the injection region ($x/h > 2$) do not change their direction. This is because, when the particle Stokes number becomes higher, the inertia of the particles also becomes larger, thus they prefer to follow the moving flow trajectory of their originally injection direction.

6.4.4.2 Turbulent dispersion effect

In this section, the turbulent dispersion model is considered on the particles, the turbulent dispersion effect on the particles with different particle Stokes numbers for two-way coupling cases is shown in Figure 6.9.

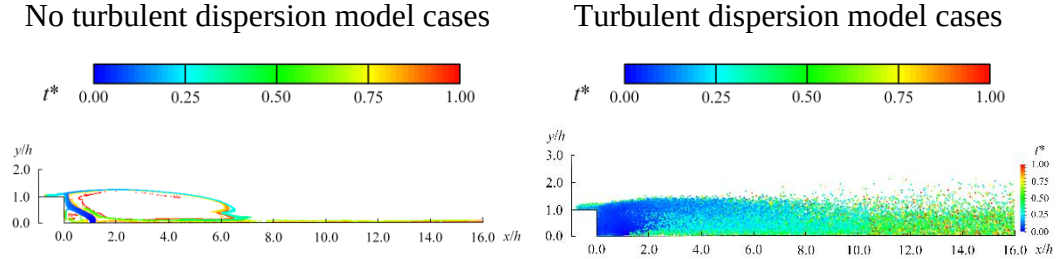

(a) St = 0.001 (b) St = 0.001

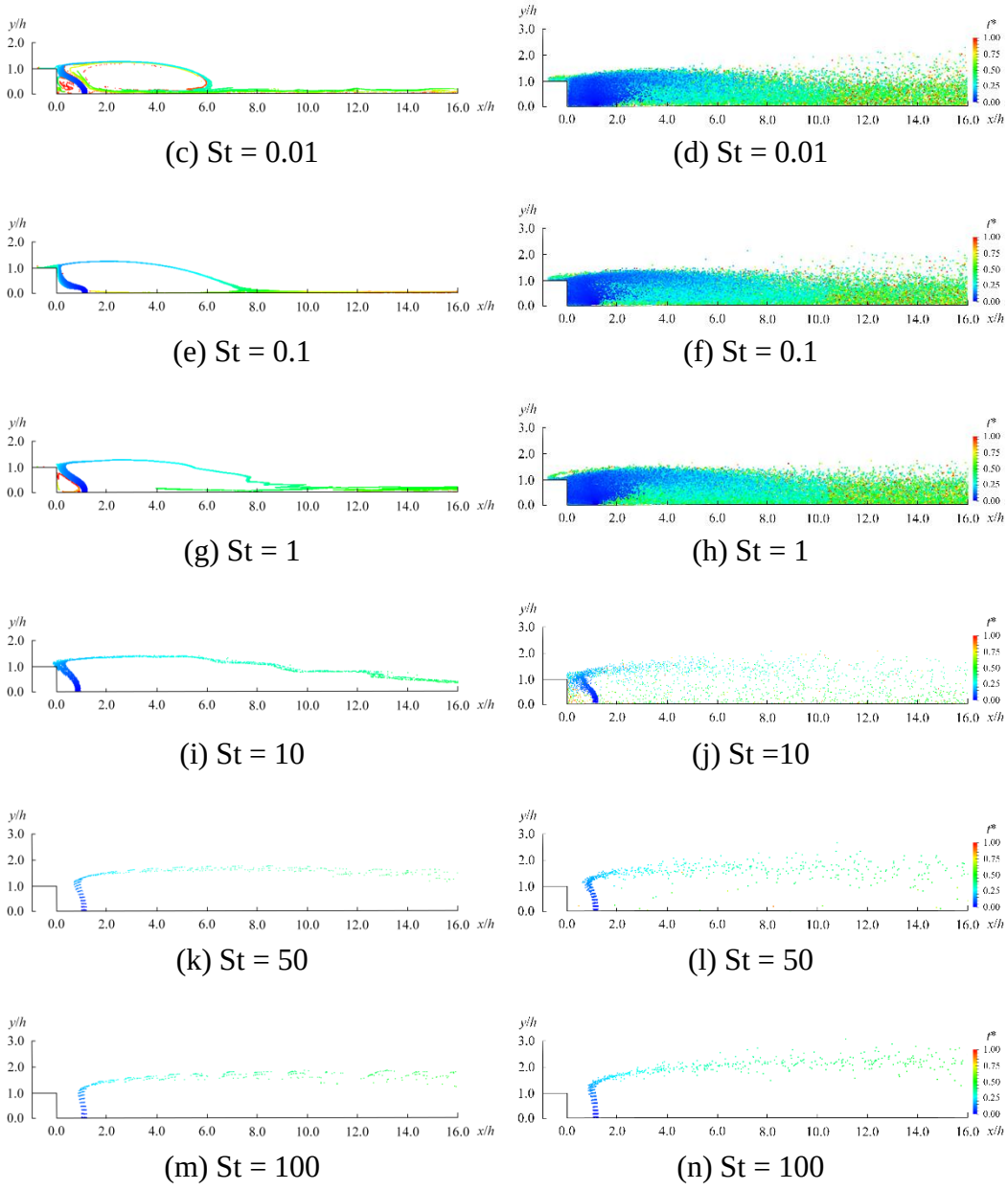

Figure 6.9 Effect of particle Stokes number and turbulent dispersion model on the instantaneous particle distribution.

It can be observed that when the particle Stokes number is smaller than 1, the behavior of the particles is significantly affected by the turbulent dispersion model. In those cases of not considering turbulent dispersion model effect, particles mainly distribute along the main flow streamline, and in those cases of considering turbulent dispersion model effect, particles almost occupy the whole area behind the

obstacle. With the increasing of particle Stokes number, the inertia of the particles becomes larger; the turbulent dispersion effect tends to become weaker. When the particle Stokes number reaches 50, the stochastic turbulent dispersion model tend to have little influence on the motion of particles, and the difference between the results obtained from different cases with and without taking into account the turbulent dispersion model is not significant.

Compared Figure 6.8 to Figure 6.9, it can be concluded that, the influence factors of turbulent dispersion model and two-way coupling effect on the particle distributions are quite similar. With the increase of the particle Stokes number, the effect of these two influence factors (both become weaker when the particle Stokes number reaches 10 or higher) are both not obvious.

6.4.4.3 Preferential particle concentration distributions

The normalized particle concentration distributions along different lines of x/h = 2, 4, 6 and 8 using the two-way coupling method are shown in Figure 6.10. It is observed that particles with different particle Stokes numbers have different particle concentration profile tendencies. When the particle Stokes number is smaller than or equal to 1, the maximum value of particle concentration is found at position of $y/h \cong 1$. The peak value of particle concentration stays approximately at the same position when the particle Stokes number is smaller than or equal to 1. Along the same line when the particle Stokes number is higher than 1, the maximum particle concentration increases with the increasing of particle Stokes number. It is also observed that when the particle Stokes number is higher than 1, with the increasing of the particle Stokes number, the particle number concentration distribution profile becomes narrower and the position of its peak value moves to further direction away

from the lower wall of the flat plate. This is because when the particle Stokes number becomes higher, the particle inertia also increases so that the turbulent dispersion effect and the wake effect of the obstacle on the particles become weaker, and the moving direction of particles tends to follow their initial velocity.

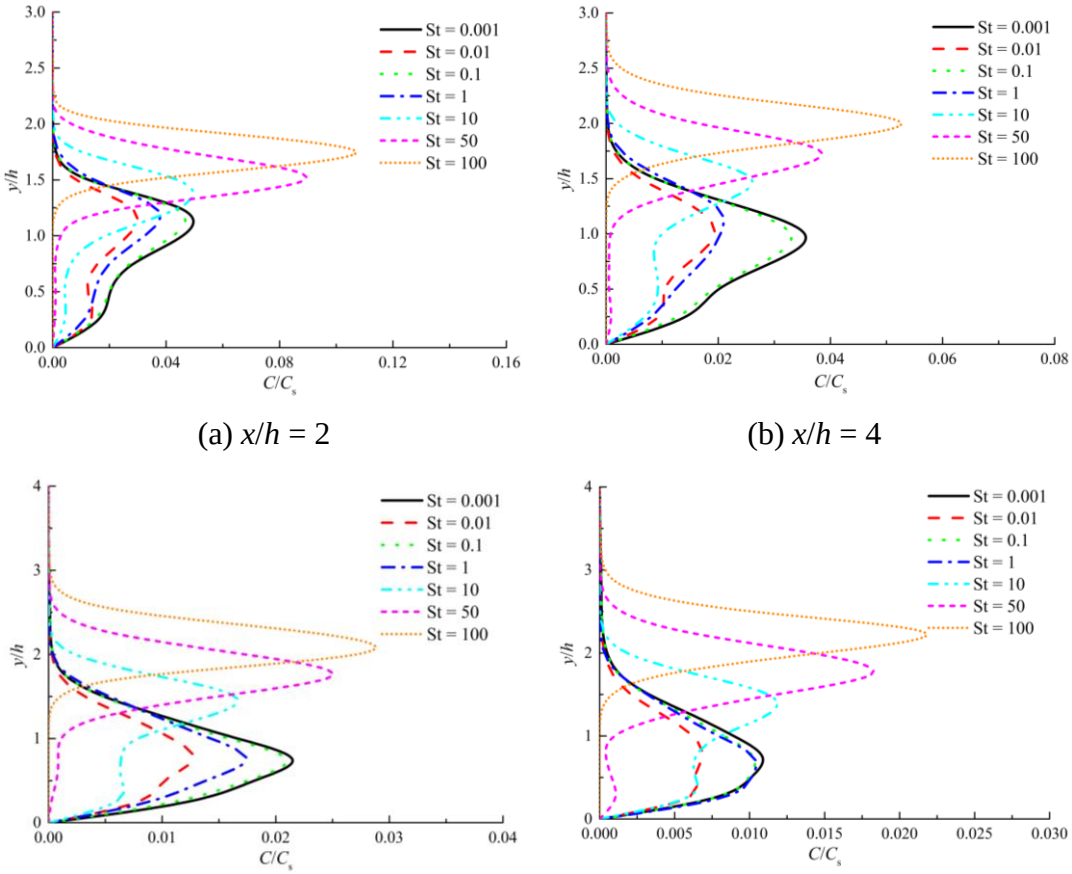

(a) x/h = 2 (b) x/h = 4

(c) x/h = 6 (d) x/h = 8

Figure 6.10 Effect of the particle Stokes number, St on the normalized particle number concentration distributions at different positions, x/h.

6.4.5 Reynolds number (Re_h) effect

The effect of Reynolds numbers based on the characteristic length of the square rod obstacle, $Re_h = uh/v$ on the normalized particle number concentration distribution profiles for the two-way coupling cases is shown in Figure 6.11. In Figure 6.11(a), when the particle Stokes number is 0.001, the profile of the particle

number concentration distribution does not change significantly with the increase of Reynolds number. The peak value of the particle concentration firstly increases and then decreases, and this variation tendency of the particle concentration distribution also applies to other cases when the particle Stokes number is 100, except that the particle concentration distribution profile becomes narrower and the position of the peak value moves to further downstream away from the lower wall of the obstacle. Furthermore, from Figure 6.11(a) to (d), the variation tendency of the normalized particle concentration profiles are almost the same at different positions (i.e., x/h = 2 to 8) and particle Stokes numbers (i.e., St = 0.001 and 100).

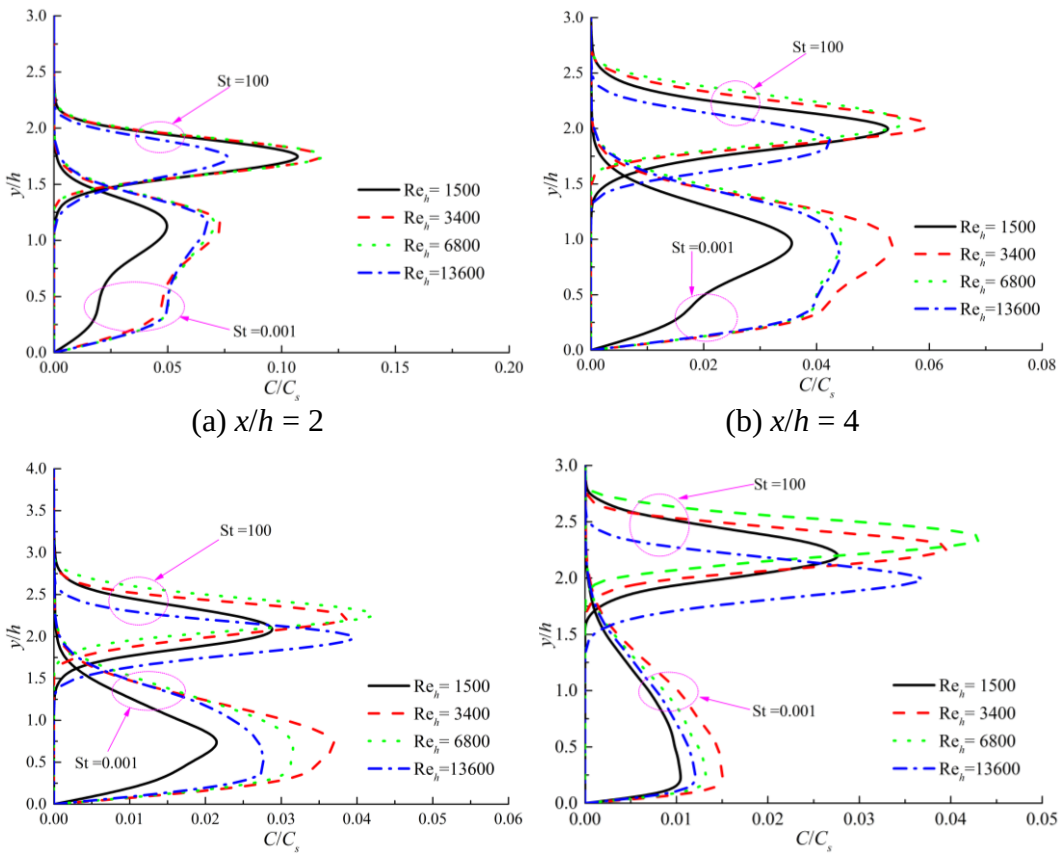

(a) x/h = 2 (b) x/h = 4

(c) x/h = 6 (d) x/h = 8

Figure 6.11 Effect of Reynolds numbers based on the square rod obstacle, Re_h on the normalized particle number concentration distribution profiles at different positions, x/h.

It is concluded that when the particle Stokes number does not change, the Reynolds number based on the obstacle has small effect on the distribution of normalized particle number concentration in the cases studied. When compared with the effect of particle Stokes number, the effect of Reynolds number on the particle distribution is relatively weak.

6.5 Summary

An Eulerian-Lagrangian model is used to simulate a spatially inhomogeneous particle-laden turbulent flow. Particles are released from the line source slot into the near-wake flow behind a square rod obstacle. The particles in turbulent flow are simulated by a coupled computational fluid dynamics (CFD)-Lagrangian Monte Carlo method. The turbulent fluctuation effects on the particle dispersion are studied using a stochastic dispersion model. The transient particle distribution and the preferential particle concentration distribution are observed for the particles released from the line source slot behind the wake flow of a square rod obstacle. The effects of particle Stokes number, two-way coupling, turbulent dispersion model, and Reynolds number based on the obstacle on the particle dispersion pattern are fully studied with the particle volume fraction, $\mathcal{O}(\times 10^{-4})$. The results show that two-way coupling method is required other than one-way coupling method because the influence of dispersed particles on the flow field is significant based on the conditions provided from the experiments of Vincont el al. (2000) that cannot be neglected. The results also reveal a significant impact of particle Stokes number on the transient particle distribution as well as the preferential particle concentration distribution. When the particle Stokes number is smaller than 1, the effects of turbulent dispersion model and two-way coupling are both important.

When increasing the particle Stokes number, the effect of two-way coupling and turbulent dispersion model are less significant and even negligible when the particle Stokes number reaches 100. Compared to the effects of two-way coupling and particle Stokes number, the effect of Reynolds number based on the obstacle on the particle number concentration distribution is not significant. With the increase of Reynolds number, the peak value of the particle concentration firstly increases and then decreases slightly.

Chapter 7 LES-DWOSMC method for simulating aerosol dynamics in turbulent flows

7.1 Introduction

In the present study, the newly developed differentially weighted operator splitting Monte Carlo (DWOSMC) method is further coupled with large eddy simulation (LES) to simulate the evolution of particle size distribution (PSD) accounting for aerosol coagulation and surface growth processes in turbulent flows. LES is used to calculate the fluid flow field, the vortex structures are captured which have significant effects on the particle dispersion pattern. The effect of the jet temperature and jet Reynolds number of the injected flows on the evolution of the PSD is also investigated.

Firstly, the newly developed LES-DWOSMC method is verified by a DNS-SM method (Miller and Garrick, 2004) for coagulation occurring in the turbulent planar jet. The time-averaged flow velocity field and mean particle diameter distributions obtained from LES-DWOSMC method show good agreement with those obtained from DNS-SM. Then the effect of jet temperature on aerosol dynamics is fully investigated for coagulation and surface growth occurring in the turbulent jet. The effect of jet Reynolds number on aerosol dynamics in the turbulent jet is also investigated for the studied cases. The evolution of time-averaged mean particle diameter, normalized particle number concentration and the particle size distribution (PSD) are studied in each case.

7.2 Numerical Methodology

Large eddy simulation (LES) for solving the Navier-Stokes N-S equations provides a good compromise between the computational accuracy and efficiency. In LES, the turbulent flows are decomposed into two parts of large- and small-scale structures: the large eddies are directly computed on an Eulerian grid, while the small eddies are modelled (Chan et al., 2008; Luo et al., 2004; Pesmazoglou and Kempf, 2017; Rodrigues et al., 2018).

In the present study, the proposed DWOSMC method is coupled with LES to study aerosol dynamics in turbulent flows. The governing equations for solving the fluid flows by LES are given in Section 3.6.2.2. The Smagorinsky subgrid-scale eddy viscosity model is used. This adopted model has widely been used and extensively validated for many research studies over the years. It assumes the equilibrium between the rates of turbulent kinetic energy production and dissipation in order to obtain a relation between the characteristic velocity and the resolved strain rate. The governing equations of the spatial position and velocity field for aerosol particles are given by Newton's second law of motion which is written as Equations (6-4) and (6-5).

The specific calculation procedure steps of this coupled LES-DWOSMC method is given as follows:

(a) Initialization. The boundary conditions and initial value of both the gas and particle phases are assigned. For the gas phase, the initial thermal and flow fields (e.g., temperature, pressure, velocity, etc.) are characterized; for the particle phase, the particle properties (e.g., weight, number concentration, size

distribution, etc.) are characterized.

(b) Start *M* Monte Carlo loops.

(c) Choose a time-step, δt. The choice of a suitable time-step should be small enough to ensure that the two-phase flows and particle dynamics are uncoupled, and different aerosol dynamic behaviors are also uncoupled.

First of all, the time step is limited by the gas phase flow. It is supposed that coagulation only occurs between particles inside one computational grid. Therefore, the displacement of the fluid element in one time-step should not be larger than the length of a computational grid. This time scale is written as,

$$\tau_f = \min(l_i/u_i) \tag{7-1}$$

where l_i and u_i are the length of grid, i and the fluid average velocity inside the grid, i, respectively.

Then, the time-step should also be smaller than the particle relaxation time scale (Zhao and Zheng, 2013), which is written as,

$$\tau_p = \rho_p d_p^2/(18\rho_f \nu) \tag{7-2}$$

Furthermore, the time scale should also be smaller than the characteristic time scales for different aerosol dynamic processes.

The characteristic time scale used for coagulation events is written as Equation (4-7). For surface growth events, the characteristic time scale is written as Equation (4-9).

To guarantee the accuracy of the newly proposed LES-DWOSMC method, an appropriate time-step that is smaller than all of those mentioned characteristic time scales should be used. In the present study, the time-step is written as:

$$\delta t \leq \min(\tau_f, \tau_p, \Delta t_{\text{coag}}, \Delta t_{\text{cond}}) \tag{7-3}$$

(d) Solving the gas flow fields. The physical conservation equations (i.e., mass, momentum and energy) of the continuous gas phase are solved, the flow field properties (i.e., velocity, pressure, temperature, etc.) are obtained.

(e) Updating the spatial position and velocity field of the particles. The motion of particles is governed by Equations (6-3) and (6-4), and thus the particle field can be solved by the Lagrangian particle tracking (LPT) method.

(f) Treatment of aerosol dynamic processes. Aerosol dynamic processes are handled by the developed DWOSMC method.

Within the time-step, the surface growth process is first calculated for the first half time-step of $\delta t/2$, and then the coagulation process is simulated for one time-step, δt. Finally, the surface growth process is calculated for the last half time-step of $\delta t/2$.

After the coagulation event, the previous particles are replaced with two newly weighted simulated particles, and the conservation of volume is considered while the properties of these particles are changed. The treatment of coagulation process considering the spatial position and the velocity field of the particles is described as Zhao and Zheng (2011):

If

$$w_i = w_j, \begin{cases} w_i^{'}=w_i/2;\ v_i^{'}=v_i+v_j;\ x_{p,i}^{'}=x_{p,i};\ u_{p,i}^{'}=(v_i u_{p,i}+v_j u_{p,j})/(v_i+v_j); \\ w_j^{'}=w_j/2;\ v_j^{'}=v_i+v_j;\ x_{p,j}^{'}=x_{p,j};\ u_{p,j}^{'}=(v_i u_{p,i}+v_j u_{p,j})/(v_i+v_j); \end{cases} \quad (7\text{-}4)$$

If

$$w_i \neq w_j, \begin{cases} w_i^{'}=\max(w_i,w_j)-\min(w_i,w_j);v_i^{'}=v_m|_{w_m=\max(w_i,w_j)}; \\ x_{p,i}^{'}=x_{p,m}|_{w_m=\max(w_i,w_j)};\ u_{p,i}^{'}=u_{p,m}|_{w_m=\max(w_i,w_j)}\ ; \\ w_j^{'}=\min(w_i,w_j);v_j^{'}=v_i+v_j; \\ x_{p,j}^{'}=x_{p,m}|_{w_m=\min(w_i,w_j)};\ u_{p,j}^{'}=(v_i u_{p,i}+v_j u_{p,j})/(v_i+v_j); \end{cases} \quad (7\text{-}5)$$

where $w_i^{'}$, $w_j^{'}$, $v_i^{'}$, $v_j^{'}$, $x_i^{'}$, $x_j^{'}$, $u_i^{'}$ and $u_j^{'}$ are the weight, volume, spatial position and velocity of newly created simulated particles, *i* and *j* after the coagulation event. In the present study, the density of particles is assumed to be constant, and so the conservation of particle volume in Equations (7-4) and (7-5) denotes the conservation of mass during the coagulation event, and therefore the velocity calculation of the particles can be based on the volume of particles.

The change in particle size distribution due to surface growth is written as Equation (4-6), and the position and velocity of particles do not change.

(g) The properties of simulated particles are updated to obtain information on the particles, as the particles are assumed to be spherical before and after coagulation and surface growth events, and thus particle diameters can be easily derived.

(h) Repeat steps (c) to (g) until the predetermined stopping time, t_{stop} is reached, and then exit the current Monte Carlo loop.

(i) Start a new Monte Carlo loop if the calculated Monte Carlo loop number, *R* is smaller than the predetermined Monte Carlo loop number, *M*. Otherwise the

averaged results are obtained to output the information of two-phase flow fields and particle distributions.

Figure 7.1 presents a flowchart of the full algorithm of the newly developed LES-DWOSMC method.

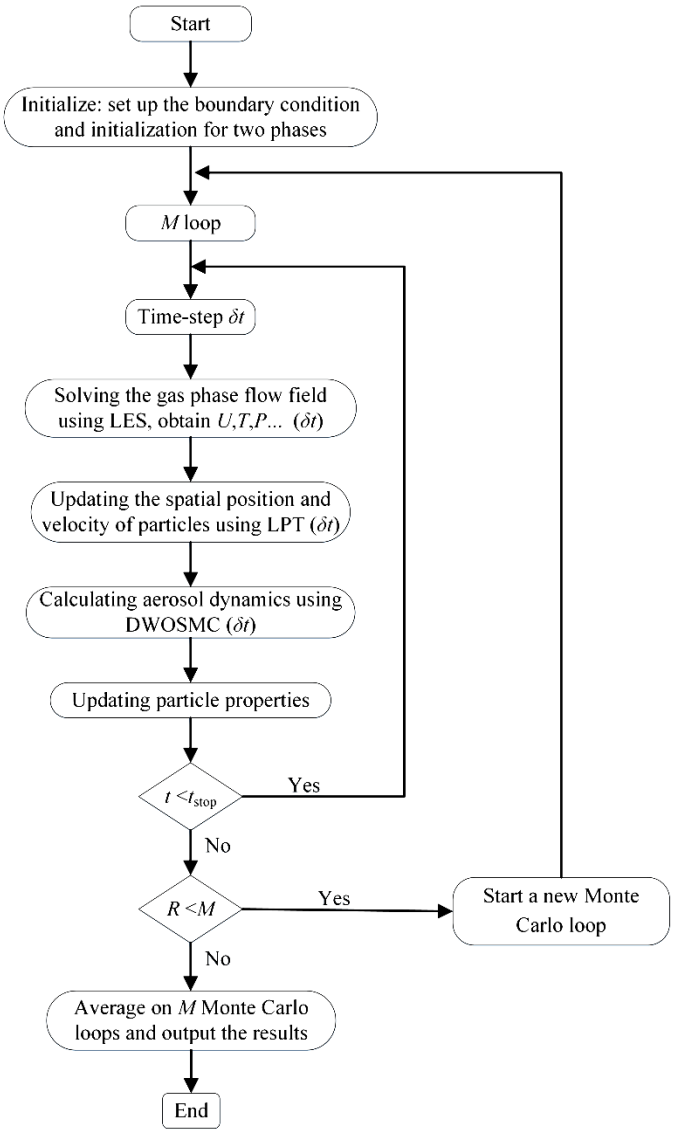

Figure 7.1 Flowchart of the newly developed LES-DWOSMC algorithm.

7.3 Numerical Simulation Setup

The developed DWOSMC is coupled into the LES turbulence model to simulate the dynamic behaviors of dispersed particles. In the present study, the Smagorinsky eddy-viscosity model is used to solve the unknown sub-grid stresses of the fluid flow field (Pesmazoglou and Kempf, 2017; Smagorinsky, 1963). Transient computing scheme is used and the convergence criterion for the relative residual of the velocity, continuity and other variables is set as 10^{-6} (Chan et al., 2018b).

7.4 Results and Discussion

Firstly, the numerical verification and implementation of the newly developed and coupled LES-DWOSMC method are examined on the numerical model used by Miller and Garrick (2004) by calculating aerosol coagulation in an incompressible and isothermal turbulent planar jet, the results are verified and compared with the direct numerical simulation-sectional method (DNS-SM) (Miller and Garrick, 2004). After the initial verification, the developed LES-DWOSMC method is used to study the effects of Reynolds number and temperature of the turbulent planar jet on the evolution of aerosol particles under the coagulation and surface growth processes.

7.4.1 Configuration and model description

Figure 7.2 shows a planar jet flow configuration examined by Miller and Garrick (2004) and also used in the present study, where the spatial coordinates, x and y are the streamwise and cross-stream directions, respectively. The diameter of the planar jet, D is 1mm, and the computational domain in x and y directions is

12×7*D*. The co-flow velocity is $U_2 = 0.55U_1$. The Reynolds number of the jet flow based on the jet diameter is, $Re_D = U_1D/\nu \cong 4000$ (Miller and Garrick, 2004).

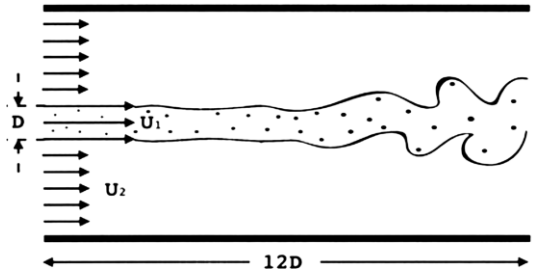

Figure 7.2 A sketch map of a planar jet flow (Miller and Garrick, 2004).

Three different grid densities (coarse meshes: 33600 cells, medium meshes: 70200 cells, and fine meshes: 279600 cells) are used to verify the grid independence. The velocity distribution profiles at x/D=6 for different grid density cases are shown in Figure 7.3(a). It can be well observed that the velocity distribution profiles calculated from the three studied meshes do not tend to have obvious difference. Furthermore, the transient distributions of the vorticity in z-direction ($\Omega_z = \partial v/\partial x - \partial u/\partial y$) calculated from the three studied meshes are shown in Figures 7.3(b) to (d). It is shown that the vortex shedding starts at around x/D = 6 in Figure 7.3(b) and at around x/D = 3.5 in both Figures 7.3(c) to (d) which are consistent with the conclusions of Miller and Garrick (2004). Since the coherent vortex structure of fluid gas has a large effect on the particle dispersion patterns, the grid density with 70200 cells proved to be sufficient to describe the gas flow and is selected to perform the numerical simulations of the present study in consideration of both computational accuracy and efficiency.

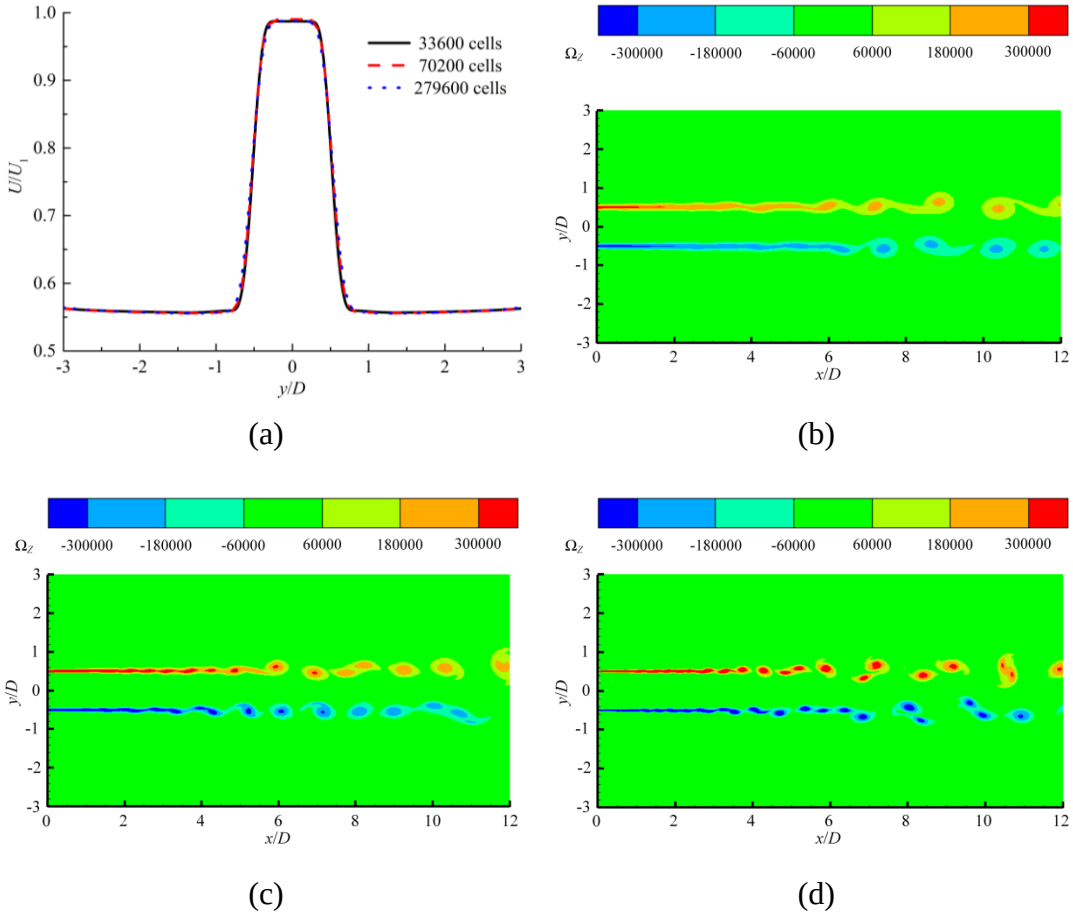

Figure 7.3 Effect of different grid densities on (a) the velocity distribution profiles, and the transient vorticity distributions by three grid densities of (b) coarse meshes: 33600 cells, (c) medium meshes: 70200 cells, and (d) fine meshes: 279600 cells.

Since the aerosol dynamics are affected by the coherent vortex structure of fluid gas, it is essential to examine the vorticity field. Figure 7.4 shows the transient evolution of the vorticity in *z*-direction at four non-dimensional times ($t^* = tU_1/D$). The choice of different times t^* is according to the time for the streamwise flows to reach $x/D = 2$, $x/D = 6$, $x/D = 10$, and after the flow is stable. It can be observed that the computational cells used are sufficient enough to capture the vortex structure of the flow field. Vorticity is generated at the interface of two parallel streams where the jet and the co-flow mix together. Vortex shedding starts at around $x/D = 3.5$, and

the peak value of vorticity magnitude becomes smaller along the streamwise direction, which is in accordance with the findings of Miller and Garrick (2004).

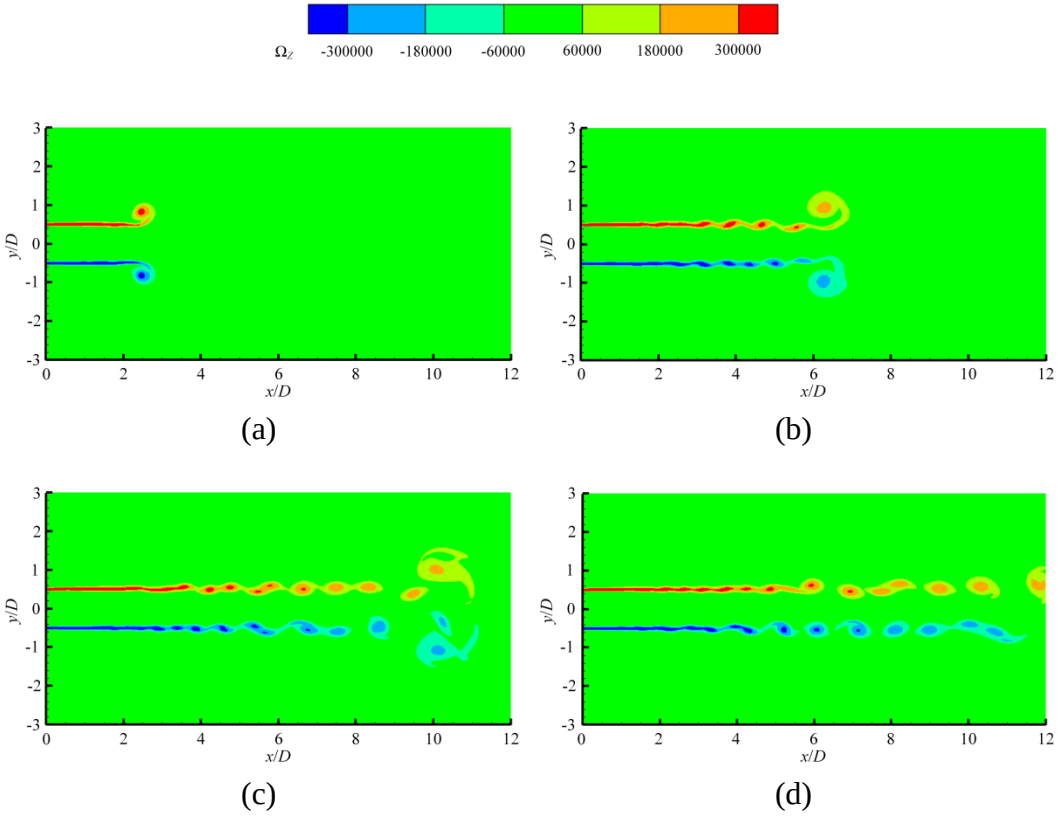

Figure 7.4 Contours of the transient evolution of vorticity at times of (a) t^* = 3.8, (b) t^* = 9.5, (c) t^* = 15.2 and (d) t^* = 28.5 at Re_D = 4000 and T_j = 300 K.

To verify the flow field in the present study, the results of time-averaged streamwise velocity of the gas phase flow at four different axial positions (x/D = 2, 6, 10, 11.5) simulated by LES are compared with the results obtained from direct numerical simulation (DNS) (Miller and Garrick, 2004). The velocity distribution profiles are shown in Figure 7.5. It can be seen that the mean velocity distributions obtained from LES agree with those obtained from DNS, and the chosen computational grid density is deemed adequate.

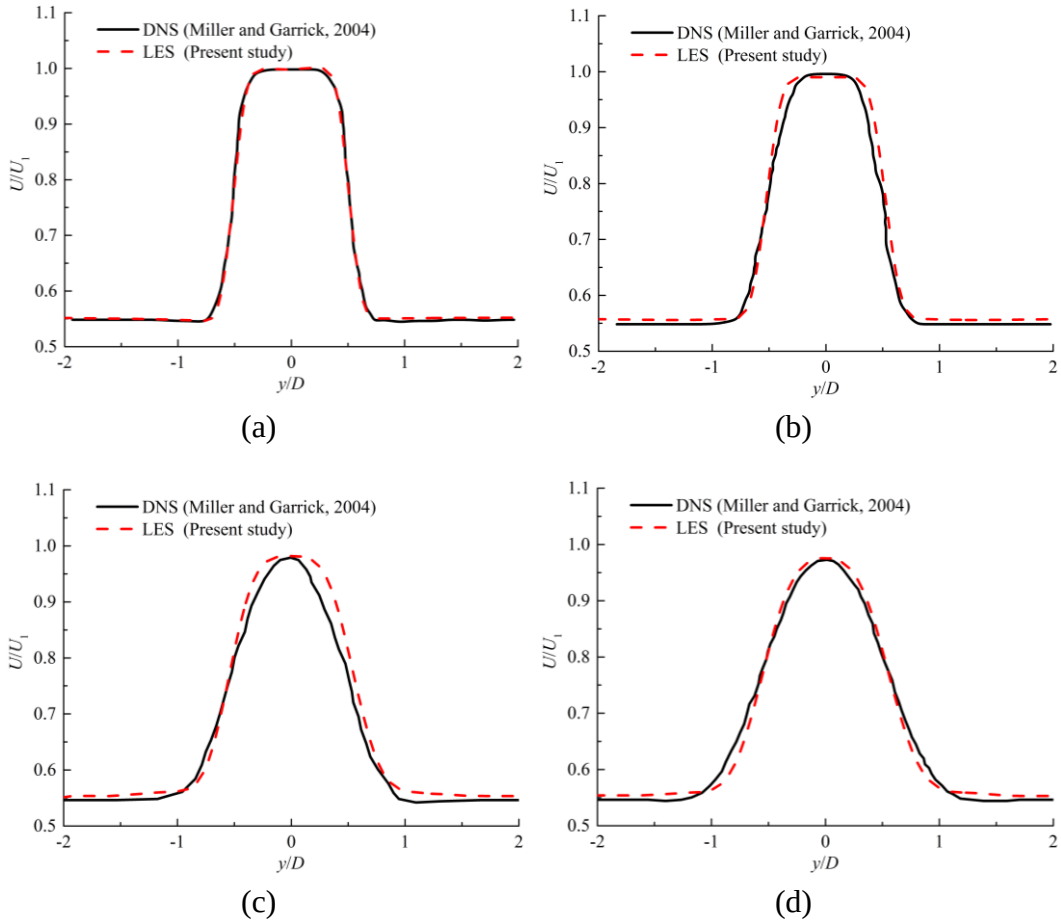

Figure 7.5 The planar jet velocity distribution profiles obtained from the present study of LES and DNS (Miller and Garrick, 2004) at (a) x/D = 2, (b) x/D = 6, (c) x/D = 10 and (d) x/D = 11.5 at Re_D = 4000 and T_j =300 K.

7.4.2 Coagulation in the turbulent planar jet

7.4.2.1 Numerical verification

In the first case studied in the present study, the flow is incompressible and isothermal with a temperature of 300K. Particles are initially uniformly distributed with a diameter of 1 nm and injected with a volume fraction of $\varphi_v \sim \mathcal{O}(\times 10^{-7})$ as similarly used by Miller and Garrick (2004). The coagulation rate under free molecule regime given by Equation (3-5) is considered.

The time-averaged mean particle diameters at four different axial positions obtained from the LES-DWOSMC method are compared with the DNS-SM (Miller and Garrick, 2004), and the results are shown in Figure 7.6.

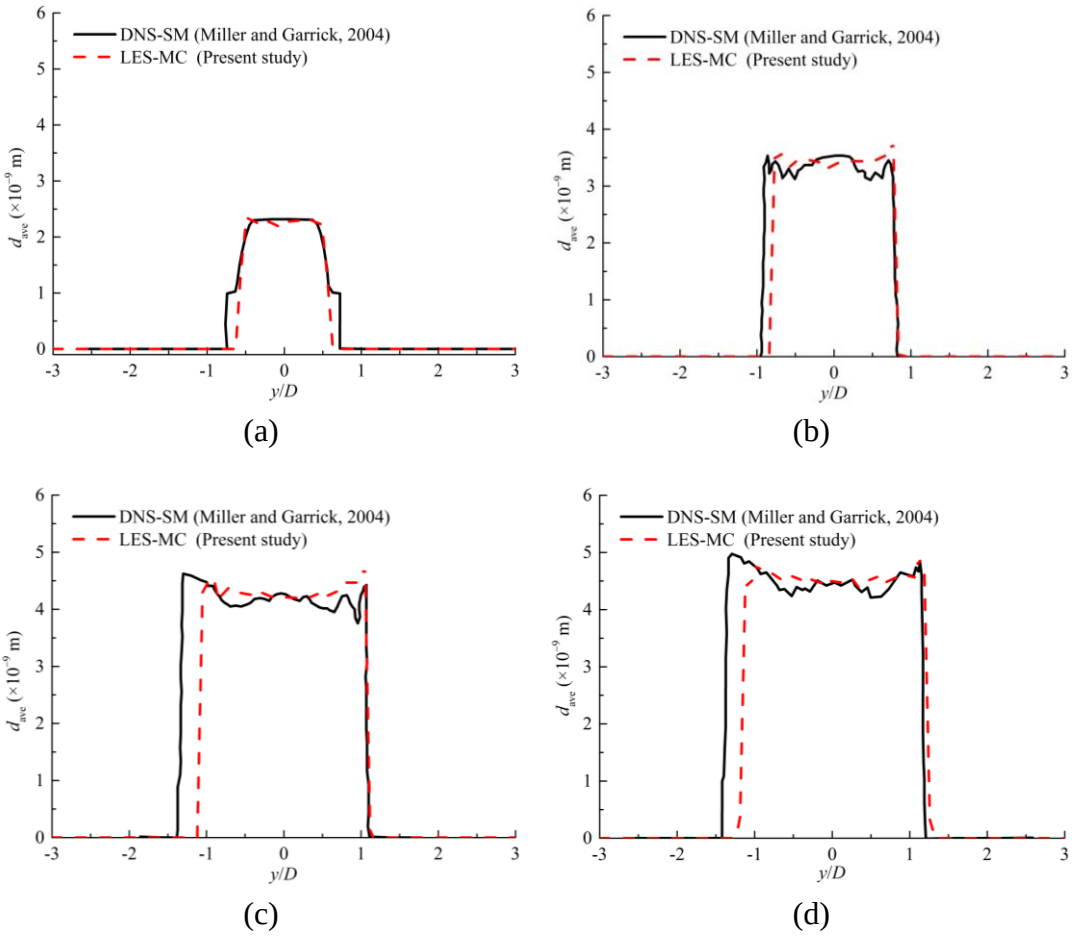

Figure 7.6 Time-averaged mean particle diameter obtained from the present study of LES-DWOSMC method and DNS-SM (Miller and Garrick, 2004) at four axial positions of (a) x/D =2, (b) x/D = 6, (c) x/D = 10 and (d) x/D = 11.5 at Re_D = 4000 and T_j =300K.

It can be seen that the time-averaged mean diameter of the particles becomes larger and the region filled with particles become wider along the streamwise direction. The results obtained from the LES-DWOSMC method are consistent with the results obtained from DNS-SM (Miller and Garrick, 2004). It can also be seen that both results show that in the interface region of the two parallel streams, the

particle diameter tends to be larger than in the jet centerline. It is because in the interface region, particles are affected by the vortex structure and acquire longer residence time to coagulate and form larger particles (Miller and Garrick, 2004; Pesmazoglou and Kempf, 2017). It can be concluded that this LES-DWOSMC method proves to be able to simulate aerosol coagulations in turbulent flows.

One advantage of MC method over deterministic methods is that the properties (e.g. diameter, volume, location, velocity, etc.) of each simulated particle can be obtained. In the present study, the transient states and dispersion characteristics of the particle field presented by the discrete simulated particles are shown in Figure 7.7.

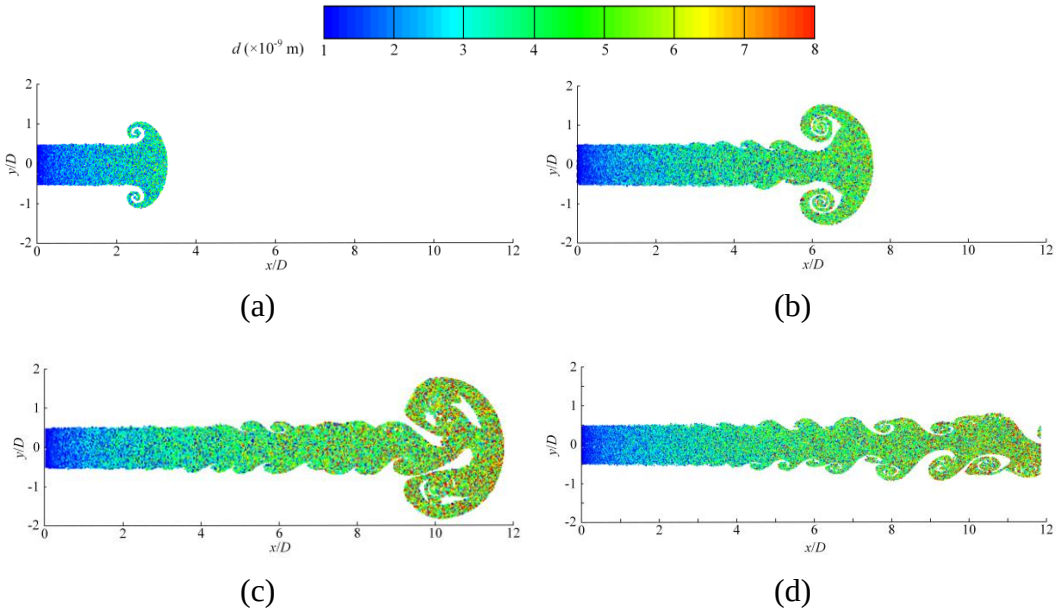

Figure 7.7 Transient particle field distribution coloured by the diameter of particles at times of (a) t^* = 3.8, (b) t^* = 9.5, (c) t^* = 15.2 and (d) t^* = 28.5 at Re_D = 4000 and T_j =300 K.

It can be observed that the transient dispersion pattern of the particles is affected by the vortex structure of the fluid flows and the transient distribution of the particles is quite similar to the contours of vorticity shown in Figure 7.4. It can

also be seen that the diameters of particles increase along the stream-wise direction because coagulation process makes the diameter of particles larger.

In the present study, the size of the aerosol particles is ~ $\mathcal{O}(\times 10^{-9}$ m), which is much smaller than the size of turbulent eddy (whose the smallest length scale is 10^{-6} m). The particle Stokes number is also much smaller than 1. So the transport behavior of the particles is perfectly affected by the turbulence vortices, which can be seen from Figs. 7.4 and 7.7, and the particles will perfectly follow the streamlines in turbulent flows.

In this developed LES-DWOSMC method, each simulated particle may have different weights. From Equations (7-4) and (7-5), it can be seen that the weights of the simulated particles become smaller after the coagulation events. The transient dispersion pattern of the particles colored by their weights at time of $t^* = 28.5$ is shown in Figure 7.8. The particles are injected with weights of $\mathcal{O}(\times 10^7)$, with the development of the jet flow, coagulation occurs, the weights of simulated particles become smaller along the streamwise direction, x. In the outlet of the jet, the weights of simulated particles are $\mathcal{O}(\times 10^4)$. Since the number of the simulated particles is assumed to be constant in the newly proposed LES-DWOSMC method, the reduction of weights implies the reduction of the number of real physical particles in the turbulent aerosol systems.

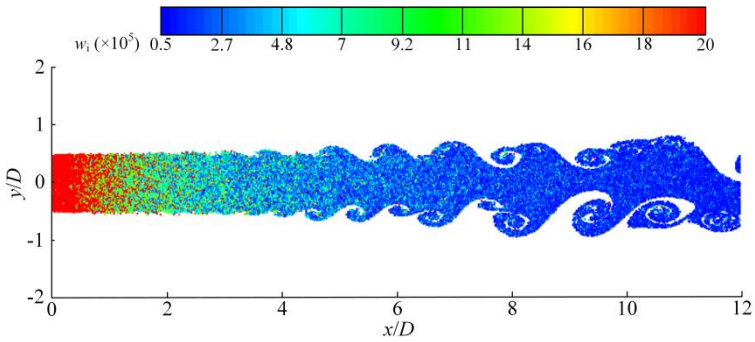

Figure 7.8 A typical transient particle field distribution coloured by the weights of simulated particles at time of t^* = 28.5 at Re_D = 4000 and T_j = 300 K.

7.4.2.2 The effect of temperature on turbulent coagulation

In the processes of soot formation and nanoparticle synthesis, aerosol particles are usually exposed in an environment with very high temperature, which will affect the aerosol dynamics processes. In the cases studied in the present study, particles are injected with three different jet temperatures, T_j of 300K, 1300K and 2300K, respectively. Other initial conditions of the particles are set up to be the same as those mentioned in Section 7.4.2.1.

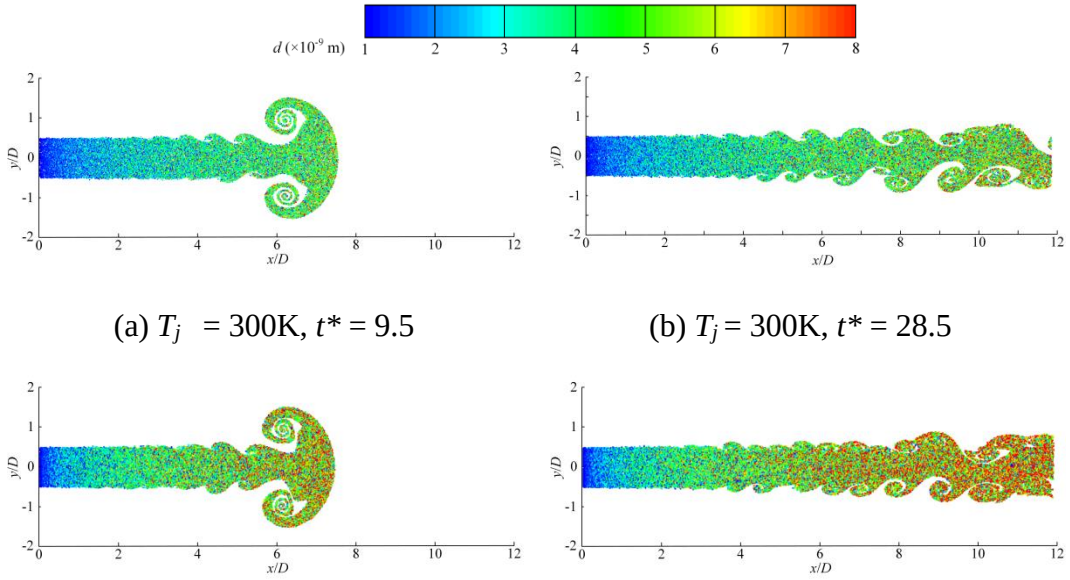

(a) T_j = 300K, t^* = 9.5 (b) T_j = 300K, t^* = 28.5

(c) T_j = 1300K, t^* = 9.5 (d) T_j = 1300K, t^* = 28.5

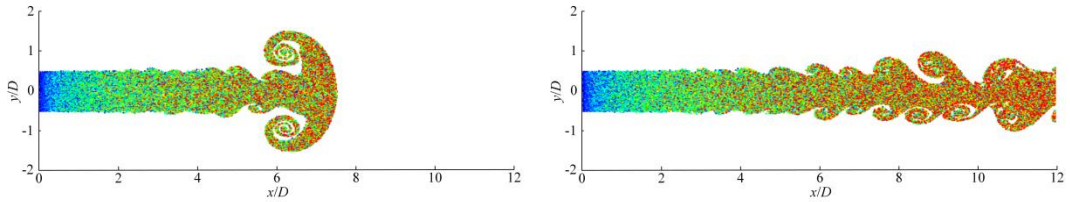

(e) T_j = 2300K, t^* = 9.5 (f) T_j = 2300K, t^* = 28.5

Figure 7.9 Transient particle field distributions at Re_D = 4000 for different T_j at times of t^* = 9.5 and t^* = 28.5.

The transient particle dispersion patterns of the three cases (i.e., T_j = 300K, 1300K and 2300K) are shown in Figure 7.9. It can be seen that with the increase of the jet temperature, the particle dispersion pattern does not change, but it is clearly noticed that particles tend to have a larger diameter at the end of the jet flow when the jet temperature is higher. It is because with higher temperature, particles become more active, which will result in more effective coagulation events, thus the particle diameter becomes larger.

The evolution of the time-averaged mean particle diameters, d_{ave} and the normalized particle number concentration, $N_c/N_{c,0}$ (where N_c is the particle number concentration, and $N_{c,0}$ is the particle number concentration in the jet inlet) at the position of y = 0 of the studied cases with different jet temperatures are shown in Figure 7.10. It is clearly shown that for each case, the time-averaged mean particle diameter increases and the normalized particle number concentration decreases along the streamwise direction because the coagulation event occurs. With the increase of jet temperature, the mean particle diameter also shows an observable increase and the reduction of particle number concentration becomes faster because the higher temperature can cause more frequent collisions between particles and strengthen the coagulation effects.

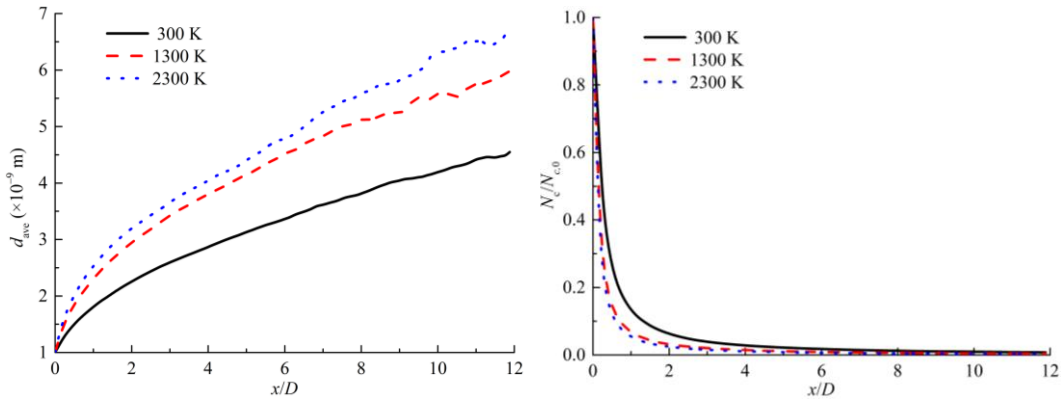

Figure 7.10 The spatial evolutions of the time-averaged (a) mean particle diameter and (b) normalized particle number concentration profiles at $y/D = 0$ and $\mathrm{Re}_D = 4000$ for different T_j.

The normalized particle size distributions (PSDs) of the studied cases for three different jet temperatures, T_j are shown in Figure 7.11, respectively. It is shown in Figure 7.11 that the peak value of the PSD curve moves towards the larger end of the particle size range and the curve of PSD becomes wider when the axial position, x/D moves along the streamwise direction. For different cases, when the temperature of the jet increases at the same position, the peak value of the PSD curve also moves towards the larger end of the particle size range. The curve of PSD also becomes wider which implies that the coagulation effect is enhanced with the increase of jet temperature. Therefore, it can be concluded that the PSD of aerosol particles or the coagulation effect of the particles can be properly controlled by introducing different ranges of temperature of the environment that the particles are exposed in.

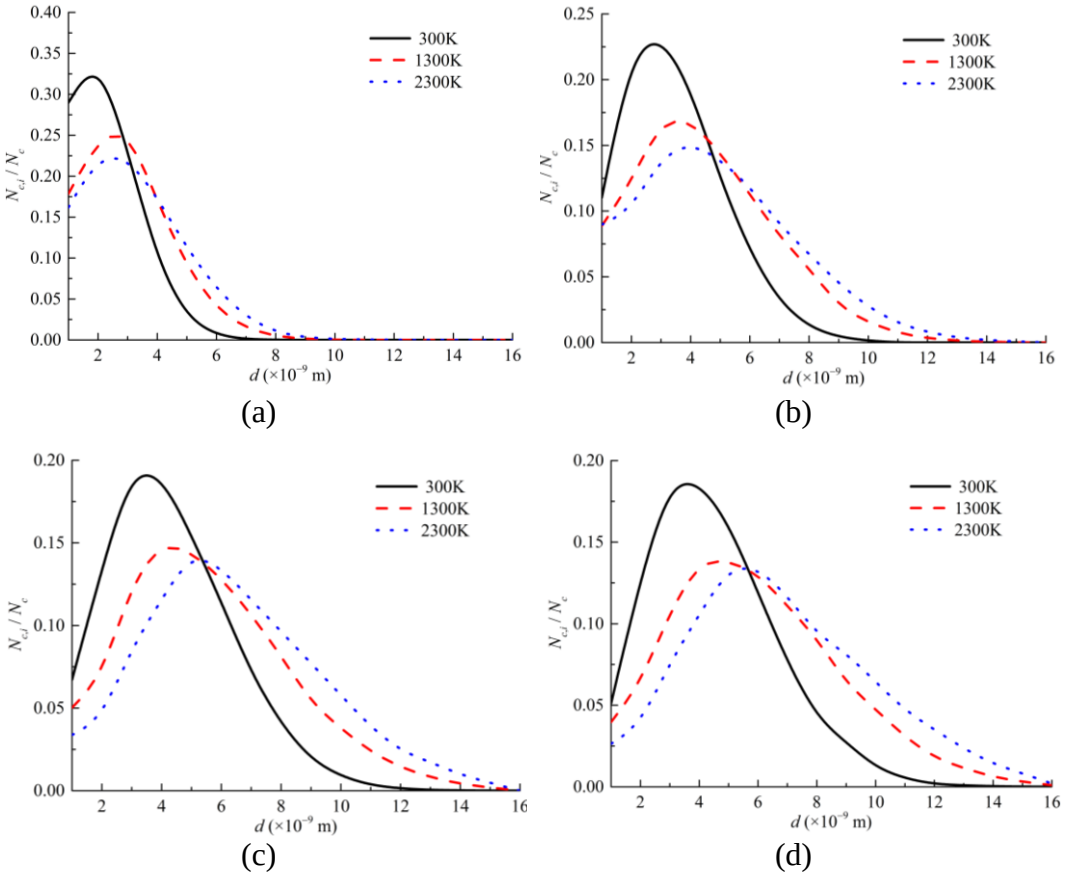

Figure 7.11 PSD profiles at positions of (a) x/D = 2, (b) x/D = 6, (c) x/D = 10 and (d) x/D = 11.5 at y/D = 0 and Re_D = 4000 for different jet temperatures, T_j.

7.4.2.3 The effect of jet Reynolds number on turbulent coagulation

The effect of jet Reynolds number, Re_D on aerosol coagulation process in the turbulent planar jet is then studied. Four corresponding Re_D = 2000, 4000, 6000, and 8000 are used for different jet temperature cases. The evolution of the time-averaged mean particle diameters, d_{ave} and the normalized particle number concentration, $N_c/N_{c,0}$ at the position of y/D = 0 for the studied cases are shown in Figures 7.12 to 7.14.

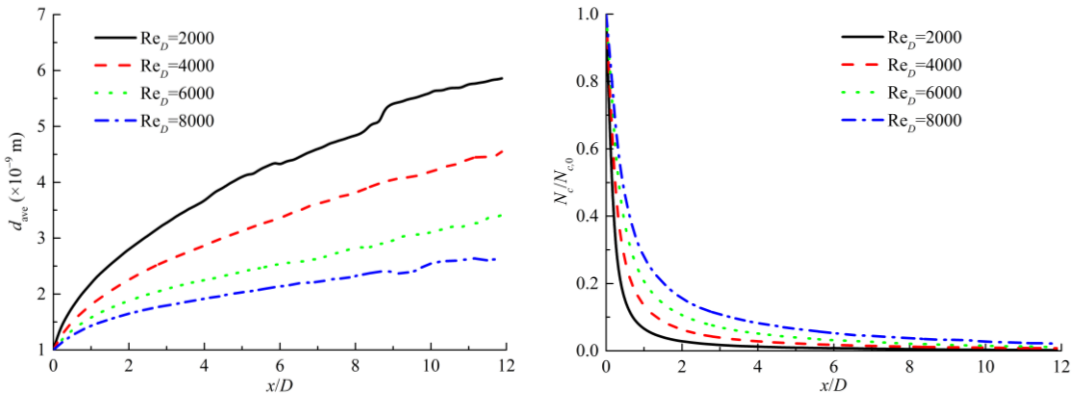

Figure 7.12 The spatial evolutions of the time-averaged (a) mean particle diameter, d_{ave} and (b) normalized particle number concentration, $N_c/N_{c,0}$ profiles at $y/D = 0$ and T_j=300K for different Re_D.

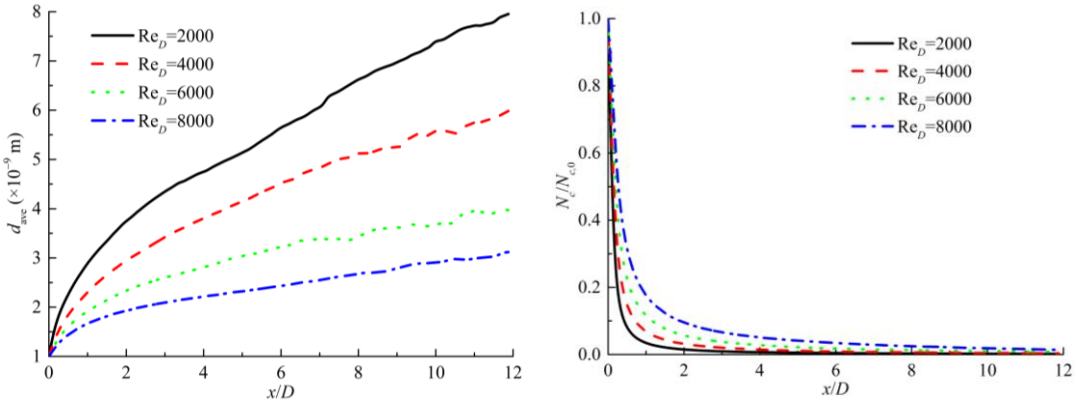

Figure 7.13 The spatial evolutions of the time-averaged (a) mean particle diameter, d_{ave} and (b) normalized particle number concentration, $N_c/N_{c,0}$ profiles at $y/D = 0$ and T_j=1300K for different Re_D.

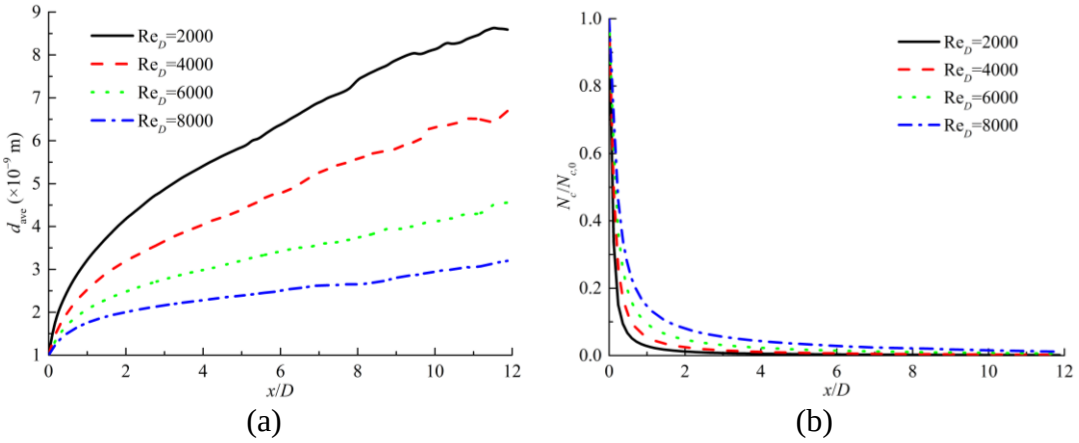

Figure 7.14 The spatial evolutions of the time-averaged (a) mean particle diameter, d_{ave} and (b) normalized particle number concentration, $N_c/N_{c,0}$ profiles at $y/D = 0$ and T_j=2300K for different Re_D.

In Figure 7.12, it can be observed that with the increase of Re_D, the mean particle diameter, d_{ave} decreases and the particle number concentration increases, which implies that the coagulation process is reduced with the increase of Re_D. It is because with the increase of the velocity of the fluid flow and particles, the residence time of the particles in the flow region decreases, which results in smaller time for the particles to coagulate to form larger particles.

Compared Figure 7.12 with Figures 7.13 and 7.14, it can be seen that when T_j = 300K, the d_{ave} at the jet outlet region increases from 2.5 to 5.5 nm when Re_D decreases from 8000 to 2000. When T_j = 2300K, the d_{ave} at the jet outlet region increases from 3 nm to 8.5 nm when Re_D decreases from 8000 to 2000. The change rate of particle diameter with the increase of Re_D increases with the increase of T_j, which shows both the effects of T_j and Re_D on the aerosol coagulation process.

The normalized particle size distributions (PSDs) of different Re_D and T_j cases are shown in Figures 7.15 to 7.17. It can be seen that, at both positions of x/h = 2 and x/h = 10, the PSD becomes higher and narrower with the increase of Re_D. When the Re_D reaches 8000, although the velocity of the particles is fast and coagulation happens at very low probabilities, the PSD still evolves observable change from x/D = 2 to x/D = 10. It can be seen that when T_j = 1300K and Re_D is 8000, the PSD at x/D = 2 is a drastically decreasing curve at almost the same rate in the whole particle size range; while the PSD at x/D = 10 has an interval (from d = 2.5 to 4.5 nm) where the curve decreases very slowly as shown in Figure 7.16.

It can also be observed that at the position of x/D = 10, when Re_D = 6000, there are two peaks of the PSD. For example, when T_j =1300K, the two peaks are at

d = 1 nm and around 4 nm, respectively; while when Re_D = 2000, 4000 and 8000, there is only one peak for the PSD. Furthermore, when $Re_D \leq 6000$ (i.e., Re_D = 2000 and 4000), the PSD at x/D = 10 firstly increases and then decreases, while when $Re_D \geq 6000$ (i.e., Re_D = 8000), the PSD at x/D = 10 monotonically decreases. Therefore, the shape and magnitude (i.e., height, width, and the number of peaks) of the PSD can be fully controlled by adjusting the parameters of T_j and Re_D for the studied cases where coagulation process occurs in the turbulent planar jet.

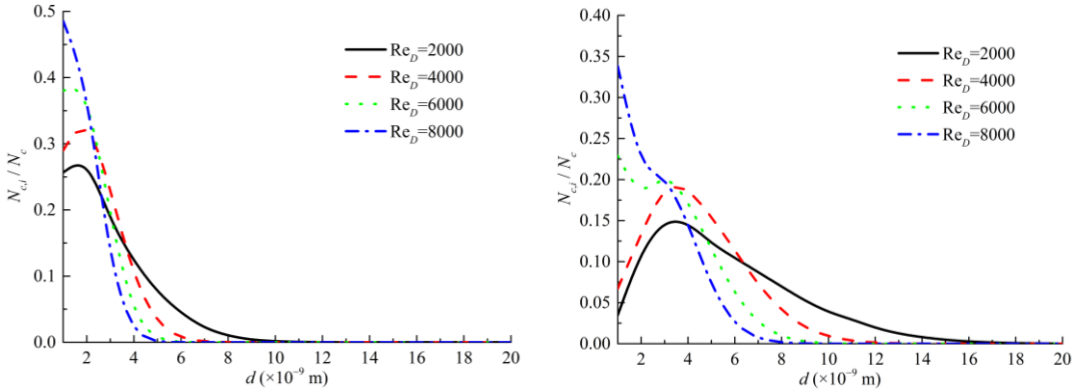

Figure 7.15 PSD profiles at axial positions of (a) x/D = 2 and (b) x/D = 10 at y/D = 0 and T_j = 300K for different Re_D.

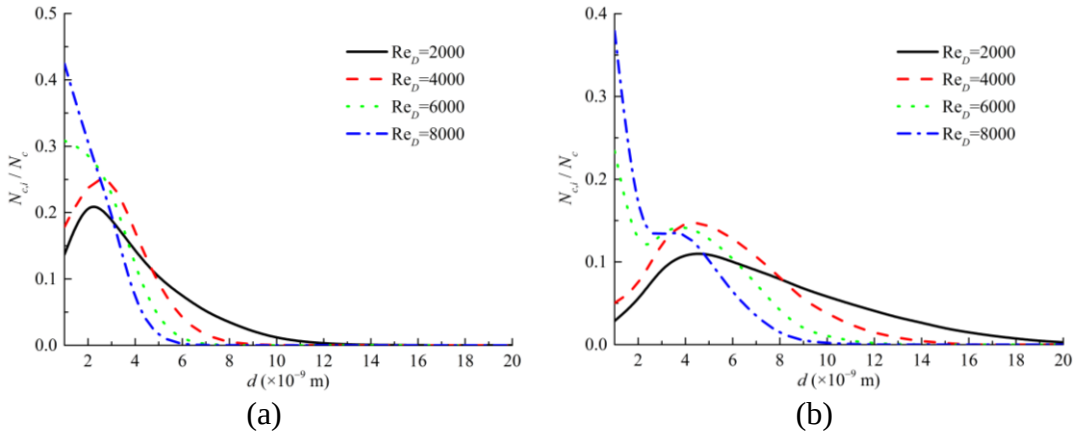

Figure 7.16 PSD profiles at axial positions of (a) x/D = 2 and (b) x/D = 10 at y/D = 0 and T_j = 1300K for different Re_D.

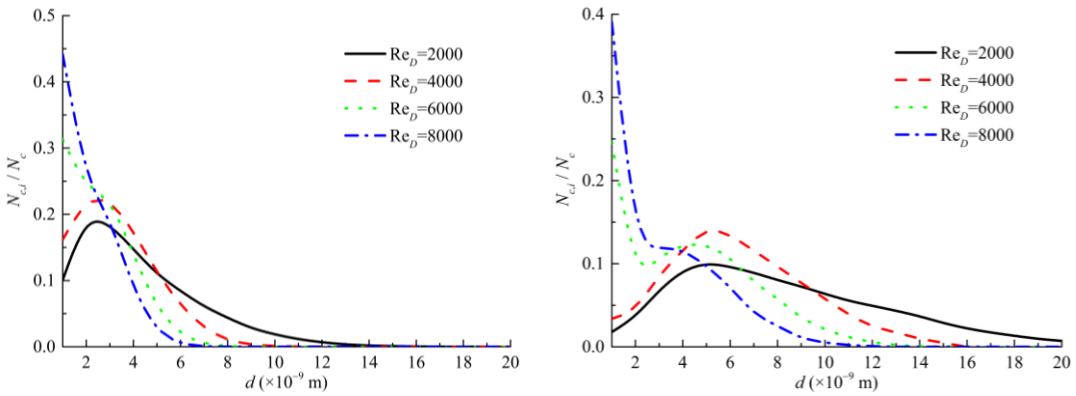

(a) (b)

Figure 7.17 PSD profiles at axial positions of (a) x/D = 2 and (b) x/D = 10 at y/D = 0 and T_j = 2300K for different Re_D.

7.4.3 Coagulation and surface growth in the turbulent planar jet

7.4.3.1 The effect of jet temperature on turbulent coagulation and surface growth

The effect of jet temperature, T_j on two simultaneous aerosol dynamic processes (i.e., coagulation and surface growth) is studied in the turbulent planar jet. The initial conditions and T_j studied are the same as previous cases mentioned in Section 7.4.2. The coagulation kernel in free molecule regime is also used, and the adopted surface growth rate is written as,

$$I(v) = \sigma v \tag{7-6}$$

where σ is 5×10^3/s.

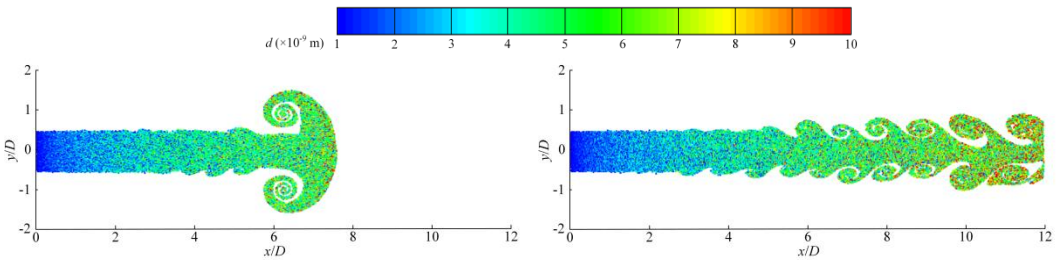

(a) T_j =300K, t^* = 9.5 (b) T_j =300K, t^* = 28.5

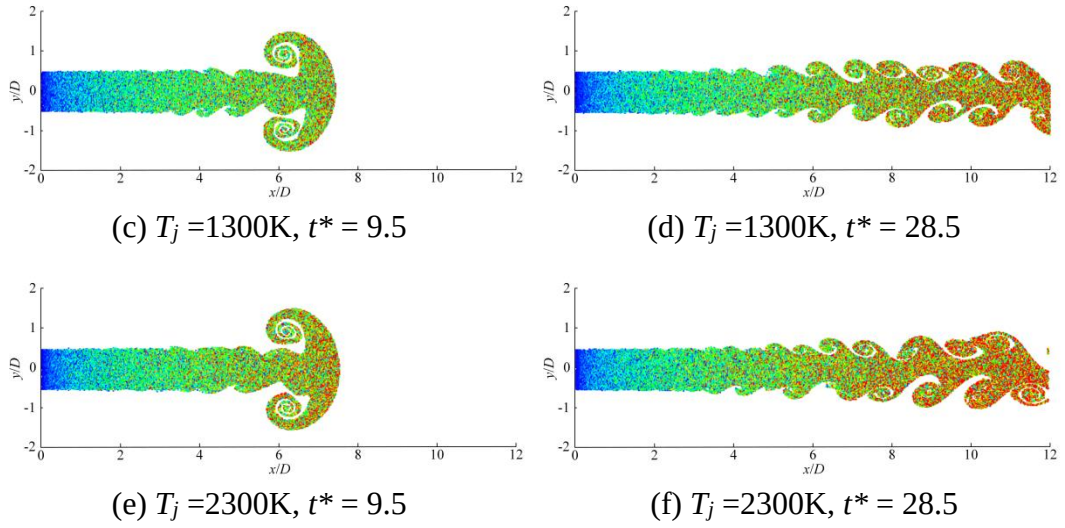

(c) T_j =1300K, t^* = 9.5 (d) T_j =1300K, t^* = 28.5

(e) T_j =2300K, t^* = 9.5 (f) T_j =2300K, t^* = 28.5

Figure 7.18 Transient particle field distribution of simultaneous coagulation and surface growth cases with Re_D = 4000 for different T_j and t^*.

The transient particle distributions of the three jet temperature cases (i.e., T_j = 300K, 1300K and 2300K) are shown in Figure 7.18. The dispersion pattern of the particles does not change while the diameter becomes larger remarkably than the cases shown in Figure 7.9 because the surface growth process is a particle growing process but does not change the particle number concentration distribution. Because the choice of the calculation time-step is small enough to ensure that the two-phase flows and particle dynamics are uncoupled, it can be seen that the particle dispersion pattern is mostly determined by the gas flow and the vortex structures in all cases.

The evolution of the time-averaged mean particle diameters, d_{ave} and the normalized particle number concentration, $N_c/N_{c,0}$ at y/D = 0 for different T_j are shown in Figure 7.19. Compared Figure 7.19 with Figure 7.10, it can be seen that when coagulation and surface growth simultaneously occur, for the same T_j cases, the growth of mean particle diameter is much faster than those cases where only coagulation occurs. The reduction rate of particle number concentration does not

significantly change because the occurrence of surface growth events does not change the particle number.

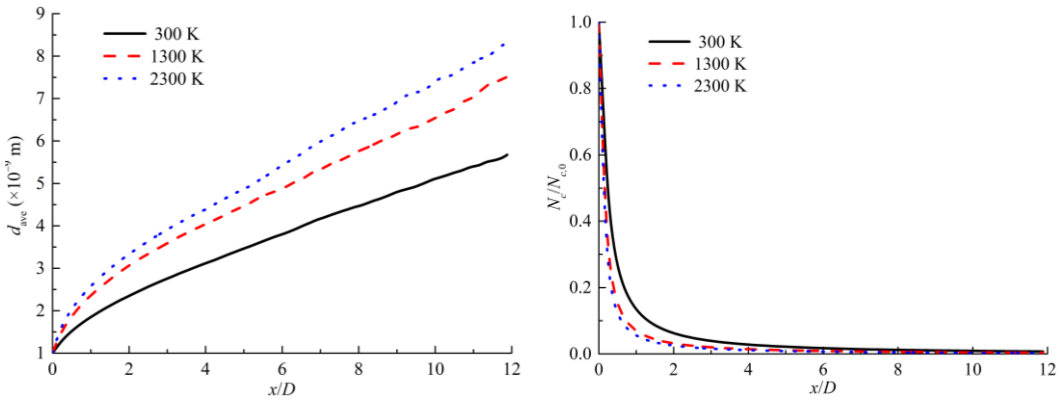

Figure 7.19 The spatial evolutions of (a) the mean particle diameter and (b) the normalized particle number concentration profiles of simultaneous coagulation and surface growth cases at y/D = 0 and Re_D =4000 for different x/D and T_j.

The normalized particle size distributions (PSDs) for different T_j are shown in Figure 7.20. Compare Figure 7.20 with Figure 7.11, the shape of the PSD curves and the evolution of PSD do not significantly change, while the PSD curve tends to be much wider and the peak value of the PSD curve moves towards the larger end of the particle size range at the same position of x/D of each case. This is because the surface growth events will result in larger size of particles and therefore influence the PSD. With the increase of T_j, the PSD at the same position of x/D becomes lower and wider, which is the same as the conclusion from the cases studied where only coagulation takes place.

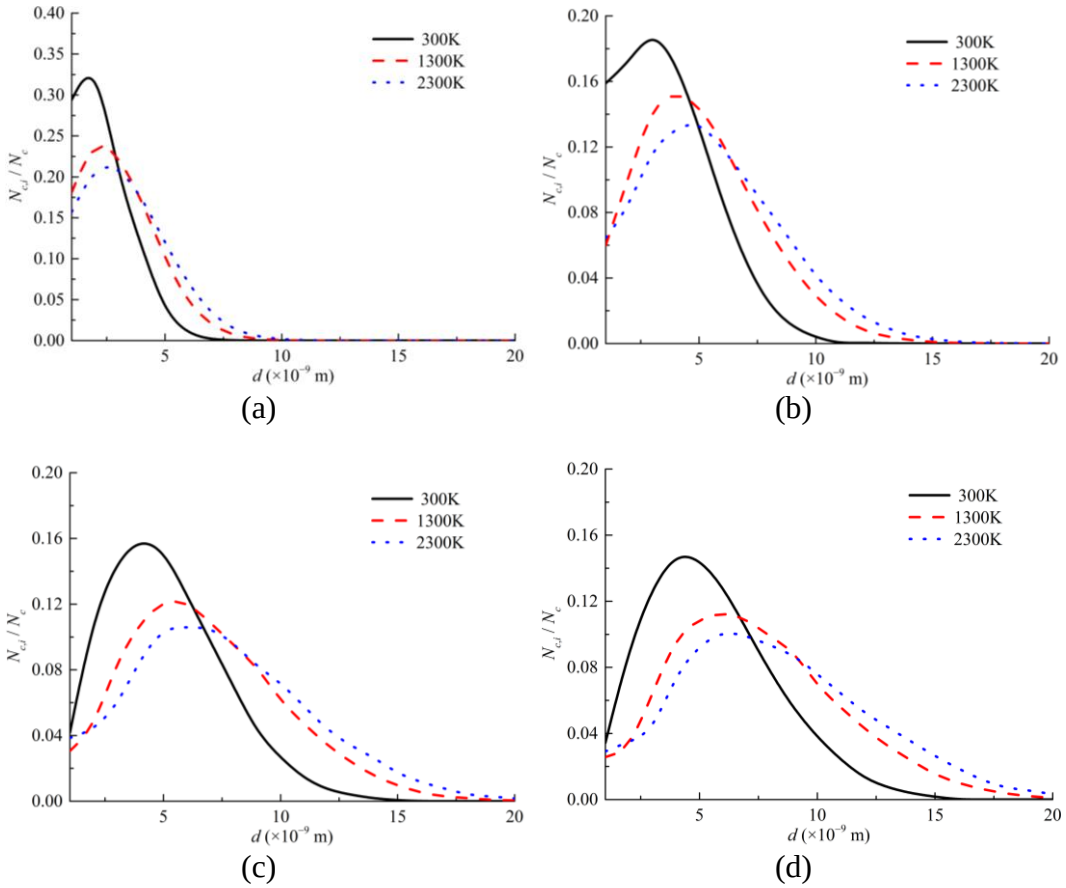

Figure 7.20 PSD profiles of simultaneous coagulation and surface growth cases at positions of (a) x/D = 2, (b) x/D = 6, (c) x/D = 10 and (d) x/D = 11.5 at y/D = 0 and Re_D = 4000 for different T_j.

7.4.3.2 The effect of jet Reynolds number on turbulent coagulation and surface growth

The effect of jet Reynolds number, Re_D on two simultaneous aerosol dynamic processes (i.e., coagulation and surface growth) is studied in the turbulent planar jet. The initial conditions, Re_D and T_j studied are the same as previous cases mentioned in Section 7.4.2.

Four corresponding Re_D = 2000, 4000, 6000 and 8000 are used for different T_j cases. The evolution of the time-averaged mean particle diameters, d_{ave} and the normalized particle number concentration, $N_c/N_{c,0}$ at y/D = 0 of the studied cases are shown in Figures 7.21 to 7.23.

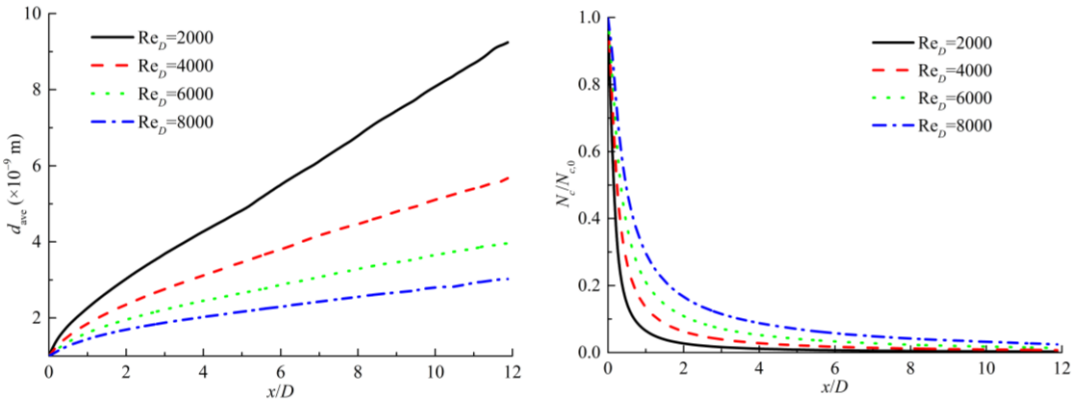

(a) (b)

Figure 7.21 The spatial evolutions of the time-averaged (a) mean particle diameter and (b) normalized particle number concentration profiles at y/D = 0 and T_j = 300K for different Re_D.

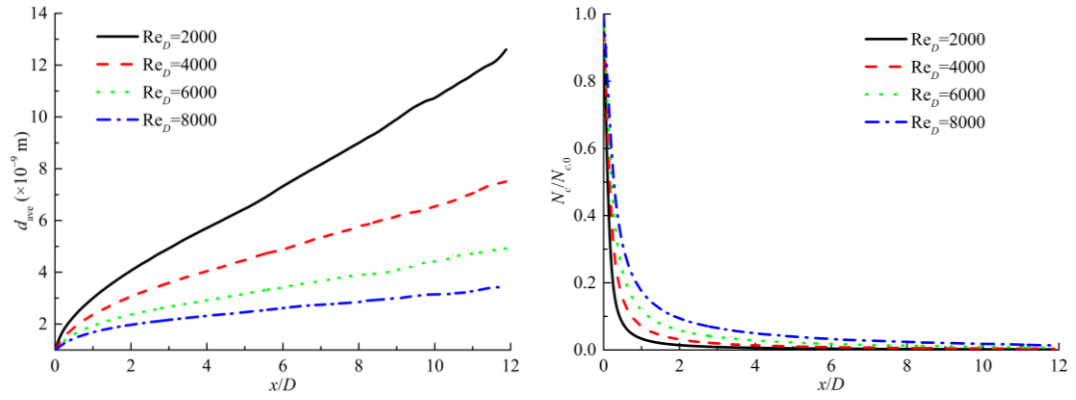

(a) (b)

Figure 7.22 The spatial evolutions of the time-averaged (a) mean particle diameter and (b) normalized particle number concentration profiles at y/D = 0 and T_j = 1300K for different Re_D.

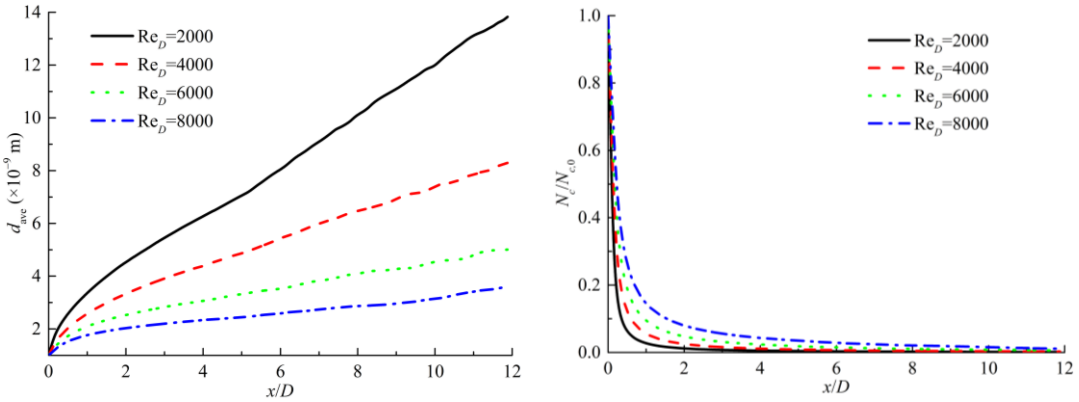

(a) (b)

Figure 7.23 The spatial evolutions of the time-averaged (a) mean particle diameter and (b) normalized particle number concentration profiles at y/D = 0 and T_j = 2300K for different Re_D.

In Figures 7.21 to 7.23, it can be seen that for cases where both coagulation and surface growth simultaneously occur at the same jet temperature cases, the mean particle diameter decreases and the particle number concentration increases with the increase of Re_D, which is similar to the cases studied where only coagulation occurs. Compared Figures 7.21 with 7.23, the effect of jet flow temperature on the evolution of d_{ave} and $N_c/N_{c,0}$ are also remarkable. The maximum particle diameter increases from around 9.5 to 14 nm when T_j increases from 300 K to 2300 K with Re_D = 2000. The particle number concentration also decreases significantly with the increase of T_j for all cases studied.

The normalized particle size distributions (PSDs) for different Re_D and T_j cases are shown in Figures 7.24 to 7.26.

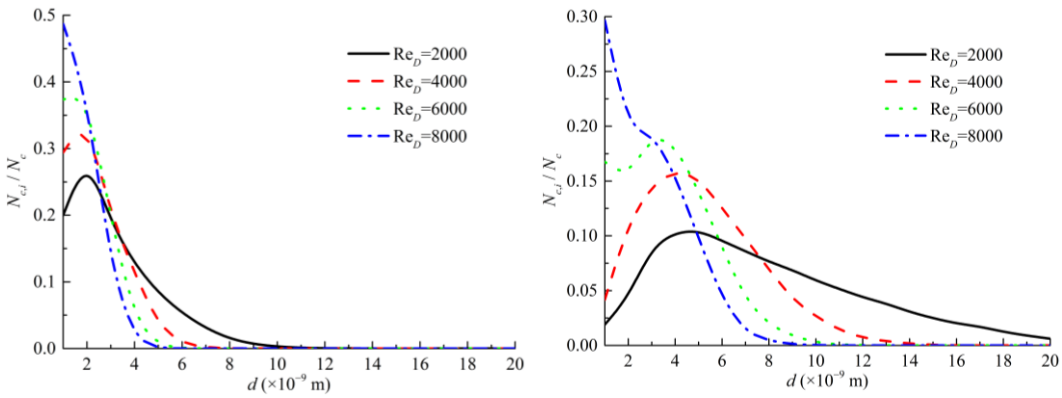

Figure 7.24 PSD profiles at positions of (a) x/D = 2, and (b) x/D = 10 at y/D = 0 and T_j = 300K for different Re_D.

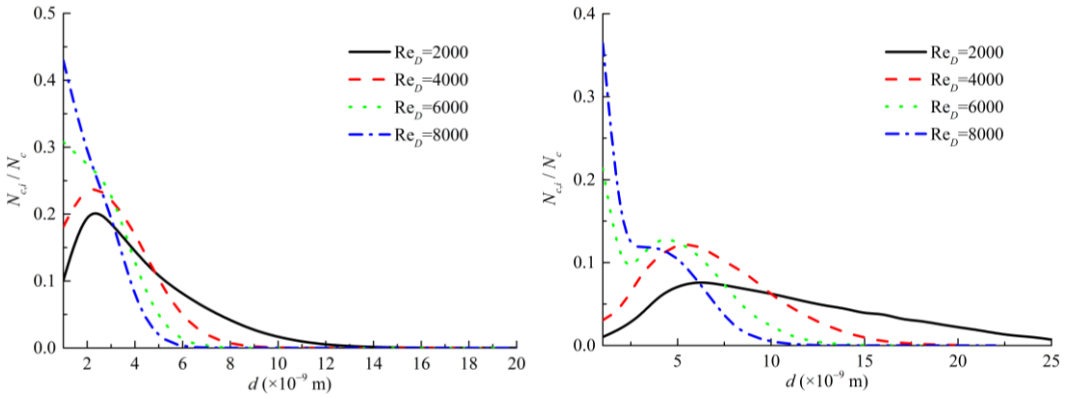

(a) (b)

Figure 7.25 PSD profiles at positions of (a) x/D = 2, and (b) x/D = 10 at y/D = 0 and T_j = 1300K for different Re_D.

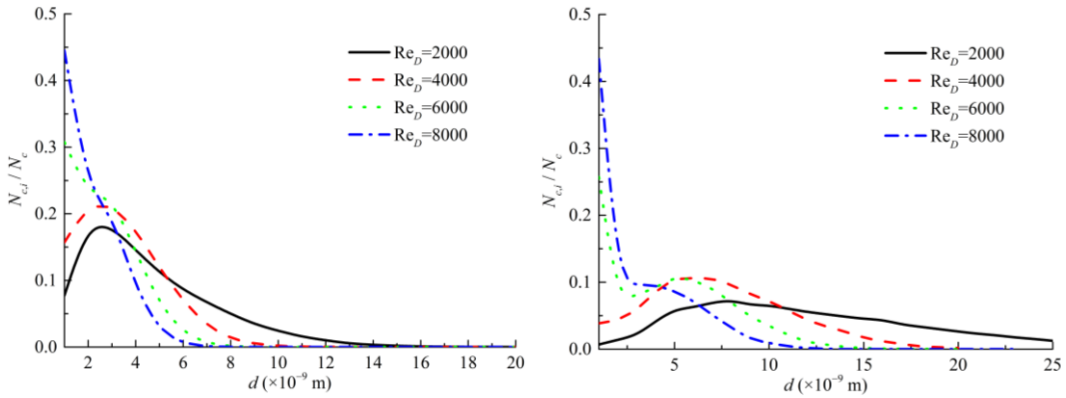

(a) (b)

Figure 7.26 PSD profiles at positions of (a) x/D = 2, and (b) x/D = 10 at y/D = 0 and T_j = 2300K for different Re_D.

Similar to the cases studied when only coagulation is considered, the PSD at the same position, x/D becomes higher and narrower with the increase of Re_D when both coagulation and surface growth are simultaneously considered. It can also be found that the shape of PSD does not change much and becomes lower and wider with the increase of T_j. The maximum particle diameter reaches larger than 25 nm and the PSD curve becomes relatively flat when T_j = 2300K with Re_D = 2000. When T_j =300K with Re_D = 8000, the maximum particle diameter is only 8 nm, and the

PSD curve decreases quite rapidly. Therefore, when coagulation and surface growth simultaneously occur, the PSD can also be fully controlled by adjusting T_j and Re_D.

From Figures 7.24(b), 7.25(b) and 7.26(b), with the increasing of Re_D, the evolution of PSD at the position of x/D = 10 is basically the same with the cases studied when only coagulation is considered. When Re_D = 6000, there are two peaks of the PSD observed. When Re_D = 2000, 4000 and 8000, there is only one peak for the PSD observed. The reason is, with the increase of Re_D, coagulation becomes weaker. When Re_D = 2000 and 4000, the coagulation effect is relatively strong, so the peak value of PSD at x/D = 10 has larger diameter; but when Re_D = 8000, the coagulation effect is relatively weak, so the peak value of PSD at x/D = 10 has a diameter of 1 nm; Re_D = 6000 is a transition value, so there are two peaks at both d = 1 nm and a larger value. It can also be seen that the particle diameter of the second peak moves towards the larger end of the particle size range and the PSD curve becomes wider with the increase of T_j. When Re_D = 8000, the PSD also monotonically decreases. Therefore, the newly proposed and developed LES-DWOSMC method proves capable of predicting the PSD when coagulation and surface growth simultaneously occur in a turbulent planar jet.

7.5 Summary

A LES-DWOSMC method is newly proposed and developed to study aerosol systems in turbulent flows. The large eddy simulation (LES) method is used to compute the continuous gas flow fields and the differentially weighted operator splitting Monte Carlo (DWOSMC) method is used to simulate the simultaneous aerosol dynamic processes (i.e., coagulation and surface growth processes). In this

developed LES-DWOSMC method, both the transient particle dispersion pattern and the time-averaged properties of particles can be obtained. The evolution of time-averaged mean particle diameter, normalized particle number concentration and the particle size distribution (PSD) are observed for the studied cases. The effects of jet temperature, T_j and Reynolds number, Re_D on the evolution of particle size distribution (PSD) are fully investigated.

The results show that the particle dispersion pattern is significantly affected by the vortex structure. It is also concluded that both coagulation and surface growth processes will result in larger particle diameter and wider PSD. The high temperature will greatly enhance the coagulation rate and change the PSD in all of the studied cases. The increase of Re_D decreases the residence time of particles and results in lower occurrence of simultaneous coagulation and surface growth processes, which will further affect the PSD of the particles. The Re_D does not only affect the height and width of the PSD, but also affect the number of peaks of the PSD. The Re_D and T_j prove to be two important parameters that can be used to control the evolution of PSD in aerosol reactors. The developed LES-DWOSMC method proves to be a computationally efficient method to deal with aerosol dynamics in turbulent flows that can be very useful in many natural and engineering applications and problems.

Chapter 8 Conclusions and Recommendations for Future Work

8.1 Review of the Present Research Study

The present study mainly focused on the numerical simulation of aerosol dynamics as well as the interaction between particles and turbulent flows with the newly proposed and developed computational fluid dynamics (CFD) based Monte Carlo method. The research work in this thesis can be divided into four major parts.

In the first part of the present research, a newly proposed and developed differentially weighted operator splitting Monte Carlo (DWOSMC) method is used for the simulation of one-component aerosol dynamics. Differentially weighted Monte Carlo method is coupled with deterministic integration method to formulate the DWOSMC method for the numerical simulation of aerosol systems undergoing the complex simultaneous aerosol dynamic processes. The studied cases cover all the typical aerosol dynamic processes including coagulation, nucleation, and condensation. This developed DWOSMC method is verified by both analytical solutions and a sectional method by comparing its numerical simulation results for different studied cases (i.e., simultaneous coagulation and condensation cases, simultaneous coagulation and nucleation cases, and simultaneous coagulation, nucleation and condensation cases). The results obtained from DWOSMC method show excellent agreement with both the analytical solution and the sectional method with high computational accuracy and efficiency.

The second part of the present research is the further extension of the developed DWOSMC method to simulate multi-component aerosol systems.

Two-component aerosol systems considering coagulation and condensation processes in different regimes are studied, and the particle number distribution, component-related particle volume density distributions and bivariate compositional distribution are obtained. This further developed DWOSMC method proves to be more computationally efficient than the sectional method for simulating two-component aerosol systems.

The third part of the present research is the further development of a CFD-Monte Carlo method for simulating turbulent gas-particle flow. The verified Lagrangian MC method in Chapters 4 and 5 is further coupled with CFD method for studying the behaviors of dispersed particles in continuous gas flows. The formulated CFD-Monte Carlo method allows investigating the interaction between particles and the carrier fluid. The effects of particle Stokes number, two-way coupling, turbulent dispersion model, and Reynolds number based on the obstacle on the particle dispersion pattern are fully studied in a spatially inhomogeneous particle-laden turbulent flow.

The fourth part of the present research is the application of the newly developed CFD-Lagrangian MC method for the aerosol dynamics in turbulent flows. Firstly, it is verified by a direct numerical simulation-sectional method (DNS-SM) method (Miller and Garrick, 2004) for coagulation occurring in a turbulent planar jet. Then the effects of jet temperature and Reynolds number on aerosol dynamics (i.e., coagulation and surface growth processes) and the evolution of the particle size distribution (PSD) are fully studied.

8.2 Main Conclusions of the Thesis

8.2.1 Conclusions of the Monte Carlo simulation of one-component aerosol dynamics

The simulation results of this newly proposed and developed differentially weighted operator splitting Monte Carlo (DWOSMC) method are fully verified with corresponding analytical solutions (Ramabhadran et al., 1976; Maisels et al., 2004) and the sectional method (Prakash et al., 2003) for various simultaneous aerosol dynamic processes (i.e., coagulation, condensation and nucleation) in different regimes.

The time evolution of the particle number concentration, the total particle volume concentration, the average particle diameter and the second moment of particles are observed, excellent agreements are obtained from this DWOSMC method with corresponding analytical solutions and the sectional method. It is concluded that for the same studied case, the maximum relative error decreases when the number of simulated particles increases. For different studied cases, the more complicated the case is, the higher the maximum relative error is. In the present study, when the number of simulated particles reaches 2000, the maximum relative error for the most complex case is within 2%. This developed DWOSMC method has been proven to have a high potential for solving complex one-component aerosol dynamic problems.

8.2.2 Conclusions of the Monte Carlo simulation of two-component aerosol dynamics

The newly developed DWOSMC method is further extended to simulate two-component aerosol systems and the results are verified by a sectional method (Prakash et al., 2003). Different initial size distribution functions and initial compositional distributions of aerosol particles are studied under various regimes of simultaneous aerosol coagulation and condensation processes. For all of these cases studied, dimensionless particle number density, total particle volume, particle number distribution and component related particle volume density distributions are obtained. The results obtained from the DWOSMC method agree well with those derived from the SM.

It is concluded that when DWOSMC method is applied to simulate the one-component aerosol system, it is much more computationally accurate and efficient than the traditional non-weighted MC method, which proves the advantage of the developed DWOSMC method than traditional MC methods. Furthermore, the SM is more computationally efficient than the DWOSMC method when it is applied to simulate one-component aerosol systems while the DWOSMC tends to be more computationally efficient when it is applied to simulate two-component aerosol systems because the DWOSMC method takes shorter time in the numerical calculation.

With such high levels of computational efficiency and accuracy based on the specific data and evidence obtained, the newly developed multi-component DWOSMC method can predict not only particle size distributions, but can also

determine component-related particle volume density and bivariate compositional distributions.

8.2.3 Conclusions of simulation of a spatially inhomogeneous particle-laden turbulent flow

Particles released from the line source slot into the near-wake flow behind a square rod obstacle are simulated by the coupled CFD-Lagrangian Monte Carlo (MC) method. The transient particle distribution and the preferential particle concentration distribution are obtained, and the effect of particle Stokes number, two-way coupling, turbulent dispersion model, and Reynolds number based on the obstacle on the particle dispersion pattern are fully studied with the particle volume fraction, $\mathcal{O}(\times 10^{-4})$.

The CFD-Lagrangian MC method is first validated by the experimental results of Vincont et al. (2000), and it is found that two-way coupling method is essentially required rather than one-way coupling method because the influence of dispersed particles on the flow field is significant which cannot be neglected.

The results also reveal a significant impact of particle Stokes number, St on the transient particle distribution as well as the preferential particle concentration distribution. When St is lower than 1, the effects of turbulent dispersion model and two-way coupling are both important. When increasing St, the effect of two-way coupling and turbulent dispersion model are less significant and even negligible when St reaches 100. Furthermore, with the increase of Reynolds number (Re_h based on the square rod obstacle, h) from 1500 to 13600, the peak value of the particle number concentration firstly increases and then decreases slightly.

8.2.4 Conclusions of LES-DWOSMC method for simulating aerosol dynamics in turbulent flows

The newly developed differentially weighted operator splitting Monte Carlo (DWOSMC) method is further coupled with large eddy simulation (LES) to simulate the evolution of particle size distribution (PSD) accounting for aerosol coagulation and surface growth processes in turbulent flows.

The newly proposed and developed LES-DWOSMC method is first verified by a DNS-SM method for coagulation occurring in a turbulent planar jet (Miller and Garrick, 2004). The flow velocity field and the time-averaged particle diameter distributions obtained from the coupled LES-DWOSMC show good agreement with those obtained from DNS-SM. Then the effects of jet temperature, T_j and jet Reynolds number, Re_D on aerosol dynamics are fully investigated for coagulation and surface growth occurring in the turbulent planar jet. The coherent vortex structures of fluid gas have significant impact on the aerosol particle dispersion patterns.

It is found that high temperature will greatly enhance the coagulation effect and change the PSD in all of the studied cases. The increase of Re_D from 2000 to 8000 decreases the residence time of particles and result in lower occurrence of coagulation and surface growth processes, which will further affect the PSD of the particles. With the increase of T_j from 300 to 2300 K, the shape of PSD curve becomes lower and wider while with the increase of Re_D, the shape of PSD curve becomes higher and narrower. Furthermore, Re_D does not only affect the height and width of the PSD curve, but also affects the number of peaks of the PSD.

The effects of T_j and Re_D on single aerosol process (i.e., coagulation) and simultaneous coagulation and surface growth processes are proved to be quite similar. And the newly developed LES-DWOSMC method proves to be a computationally efficient method to deal with aerosol dynamics in turbulent flows which can be very useful in many natural and engineering applications and problems.

8.3 Recommendations for Future Work

The thesis presents the numerical simulation of typical and complex aerosol dynamic processes in both one-component and two-component aerosol systems. The interaction of turbulent flows and particles, and aerosol dynamics in turbulent gas-particle flows are also studied by the developed computational fluid dynamics-Monte Carlo (CFD-MC) method. Based on the differentially weighted Monte Carlo (DWMC) method and the operator splitting (OS) technique, the aim of the thesis is achieved for developing a robust and highly efficient CFD-Monte Carlo method for solving complex simultaneous aerosol dynamics in turbulent flows.

However, further research work is still recommended to overcome the limitations of these developed numerical methods and optimizations are also needed to make the methods more robust and powerful.

8.3.1 Limitations of the present research study

The limitations of this newly proposed and developed DWOSMC and CFD-Monte Caro methods are as follows:

1. In the present study, the developed CFD-Monte Carlo method is used to investigate particle-fluid systems in typical two-dimensional systems for numerical verifications and validations purpose. However, in practical applications, three-dimensional aerosol reactors are also widely encountered. Therefore, the application of the developed CFD-MC method can be extended to aerosols related particle-fluid systems in three-dimensional simulation if such experimental conditions and datasets are available in the literature for numerical validation purpose.

2. In many aerosols related applications, such as combustion nanoparticle synthesis and soot formation, the aerosol systems can be encountered with complex chemical reactions. Thus, a comprehensive modeling of detailed chemistry should also be included in the study of turbulent reactive flows. While in the present study, the combustion mechanism and chemical reactions are not considered yet.

3. Due to the fact that very few analytical solutions and experimental data are available for complex aerosol dynamics in literature, especially for aerosol dynamic processes in turbulent flows, the validation of the developed DWOSMC and CFD-MC methods is only limited to comparing with analytical solutions in simple simultaneous aerosol processes cases and comparing with other numerical methods in relatively complex simultaneous aerosol processes cases or aerosol systems in turbulent flows.

8.3.2 Recommendations for future work

Considering the above-mentioned limitations on the present study, recommendations are made as follows:

1. Three-dimensional simulation. The codes of the developed CFD-MC method can be further extended to three-dimensional simulations of complex aerosol dynamics in aerosol reactors or other particle-fluid systems with arbitrary configurations for numerical validation.

2. Application in turbulent reactive flows. In order to further evaluate the capability of the developed CFD-MC method in simulating complex aerosol systems, a comprehensive modeling of detailed chemistry can be included in the study of turbulent reactive flows. A more specific application in soot formation or nanoparticle synthesis cases can be investigated.

3. Experimental validation. Experimental validation is needed if the developed CFD-MC method is to be used in real scientific and engineering applications. Therefore, experiments designed individually will be conducted to acquire first-hand reliable experimental datasets and conditions to further validate this CFD-MC numerical method which is highly desired.

References

Aardahl, C.L., Davis, E.J., 1996. Gas aerosol chemical reactions in the NaOH-SO_2-H_2O system. *Applied Spectroscopy* 50, 71–77.

Akbarzadeh, V., Hrymak, A.N., 2016. Coupled CFD-DEM of particle-laden flows in a turning flow with a moving wall. *Computers and Chemical Engineering* 86, 184–191.

Akroyd, J., Smith, A.J., Shirley, R., McGlashan, L.R., Kraft, M., 2011. A coupled CFD-population balance approach for nanoparticle synthesis in turbulent reacting flows. *Chemical Engineering Science* 66, 3792–3805.

Almohammed, N., 2018. Modeling and simulation of particle agglomeration, droplet coalescence and particle-wall adhesion in turbulent multiphase flows. University of the German Federal Armed Forces Hamburg.

ANSYS, I., 2013. ANSYS Fluent theory guide:Multiphase flow analysis using population balance modeling.

Armenio, V., Fiorotto, V., 2013. The importance of the forces acting on particles in turbulent flows. *Physics of Fluids* 13, 2437–2440.

Aubagnac-Karkar, D., El Bakali, A., Desgroux, P., 2018. Soot particles inception and PAH condensation modelling applied in a soot model utilizing a sectional method. *Combustion and Flame* 189, 1339–1351.

Ayeni, O.O., Wu, C.L., Nandakumar, K., Joshi, J.B., 2016. Development and validation of a new drag law using mechanical energy balance approach for DEM-CFD simulation of gas-solid fluidized bed. *Chemical Engineering Journal* 302, 395–405.

Balachandar, S., Eaton, J.K., 2010. Turbulent dispersed multiphase flow. *Annual Review of Fluid Mechanics* 42, 111–133.

Battista, F., Gualtieri, P., Mollicone, J.P., Casciola, C.M., 2018. Application of the Exact Regularized Point Particle method (ERPP) to particle laden turbulent shear flows in the two-way coupling regime. *International Journal of Multiphase Flow* 101, 113–124.

Bayraktar, E., 2014. Numerical aspects of population balance equations coupled to computational fluid dynamics.

Bird, G.A., 1994. Molecular gas dynamics and the direct simulation of gas flows. Clarendon Press, New York.

Bird, G.A., 1976. Molecular gas dynamics, in: NASA STI/Recon Technical Report A 76. Clarendon Press, Oxford.

Bird, G.A., 1963. Approach to translational equilibrium in a rigid sphere gas. *Physics of Fluids* 6, 1518–1519.

Bocksell, T.L., Loth, E., 2006. Stochastic modeling of particle diffusion in a turbulent boundary layer. *International Journal of Multiphase Flow* 32, 1234–1253.

Bocksell, T.L., Loth, E., 2001. Random walk models for particle diffusion in free-shear flows. *AIAA Journal* 39, 1086–1096.

Boucher, O., 2015. Atmospheric Aerosols:properties and climate impacts, Journal of Chemical Information and Modeling. Springer Netherlands, Dordrecht.

Boyd, I.D., 1996. Conservative Species Weighting Scheme for the Direct Simulation Monte Carlo Method. *Journal of Thermophysics and Heat Transfer* 10, 579–585.

Brennen, C.E., 2005. Fundamentals of multiphase flows. Cambridge University Press, Pasadena, California.

Bressi, M., Cavalli, F., Belis, C.A., Putaud, J.-P., Fröhlich, R., Martins dos Santos, S., Petralia, E., Prévôt, A.S.H., Berico, M., Malaguti, A., Canonaco, F., 2016. Variations in the chemical composition of the submicron aerosol and in the sources of the organic fraction at a regional background site of the Po Valley (Italy). *Atmospheric Chemistry and Physics Discussions* 16, 12875–12896.

Brown, D.P., Kauppinen, E.I., Jokiniemi, J.K., Rubin, S.G., Biswas, P., 2006. A method of moments based CFD model for polydisperse aerosol flows with strong interphase mass and heat transfer. *Computers and Fluids* 35, 762–780.

Bzdek, B.R., Pennington, M.R., Johnston, M. V., 2012. Single particle chemical analysis of ambient ultrafine aerosol: A review. Journal of Aerosol Science 52, 109–120.

Carichino, L., Guidoboni, G., Szopos, M., 2018. Energy-based operator splitting approach for the time discretization of coupled systems of partial and ordinary differential equations for fluid flows: The Stokes case. *Journal of Computational Physics* 364, 235–256.

Carrayrou, J., Mosé, R., Behra, P., 2004. Operator-splitting procedures for reactive transport and comparison of mass balance errors. *Journal of Contaminant Hydrology* 68, 239–268.

Celnik, M., Patterson, R., Kraft, M., Wagner, W., 2007. Coupling a stochastic soot population balance to gas-phase chemistry using operator splitting. *Combustion and Flame* 148, 158–176.

Chan, T.L., Liu, S.Y., Liu, H.J., 2018a. A numerical study on particle formation and evolution of a vehicular exhaust plume using the bimodal TEMOM. *Particuology*, accepted for publication.

Chan, T.L., Liu, S.Y., Yue, Y., 2018b. Nanoparticle formation and growth in turbulent flows using the bimodal TEMOM. *Powder Technology* 323, 507–517.

Chan, T.L., Liu, Y.H., Chan, C.K., 2010. Direct quadrature method of moments for the exhaust particle formation and evolution in the wake of the studied ground vehicle. *Journal of Aerosol Science* 41, 553–568.

Chan, T.L., Luo, D.D., Cheung, C.S., Chan, C.K., 2008. Large eddy simulation of flow structures and pollutant dispersion in the near-wake region of the studied ground vehicle for different driving conditions. *Atmospheric Environment* 42, 5317–5339.

Chen, Z., Lin, J., Yu, M., 2014. Direct expansion method of moments for nanoparticle Brownian coagulation in the entire size regime. *Journal of Aerosol Science* 67, 28–37.

Chiesa, M., Mathiesen, V., Melheim, J.A., Halvorsen, B., 2005. Numerical simulation of particulate flow by the Eulerian-Lagrangian and the Eulerian-Eulerian approach with application to a fluidized bed. *Computers and Chemical Engineering* 29, 291–304.

Clarke, D.A., Sederman, A.J., Gladden, L.F., Holland, D.J., 2018. Investigation of void fraction schemes for use with CFD-DEM simulations of fluidized beds. *Industrial and Engineering Chemistry Research* 57, 3002–3013.

Crowe, C.T., Chung, J.N., Troutt, T.R., 1988. Particle mixing in free shear flow. *Progress in Energy and Combustion Science* 14, 171–194.

Crowe, C.T., Sharma, M.P., Stock, D.E., 1977. The Particle-Source-ln Cell (PSI-CELL) model for gas-droplet flows. *Journal of Fluids Engineering* 99, 325–332.

Davari, S.A., Mukherjee, D., 2018. Kinetic Monte Carlo simulation for homogeneous nucleation of metal nanoparticles during vapor phase synthesis. *AIChE Journal* 64, 18-28.

Debry, E., Sportisse, B., Jourdain, B., 2003. A stochastic approach for the numerical simulation of the general dynamics equation for aerosols. *Journal of Computational Physics* 184, 649–669.

Dentener, F.J., Crutzen, P.J., 1993. Reaction of N_2O_5 on tropospheric aerosols: Impact on the global distributions of NOx,O_3,and OH. *Journal of Geophysical Research* 98, 7149.

Dergaoui, H., Sartelet, K.N., Debry, E., Seigneur, C., 2013. Modeling coagulation of externally mixed particles: Sectional approach for both size and chemical composition. *Journal of Aerosol Science* 58, 17–32.

Deville, R.E.L., Riemer, N., West, M., 2011. Weighted Flow Algorithms (WFA) for stochastic particle coagulation. *Journal of Computational Physics* 230, 8427–8451.

Dizaji, F.F., Marshall, J.S., 2017. On the significance of two-way coupling in simulation of turbulent particle agglomeration. *Powder Technology* 318, 83–94.

Dou, Z., Bragg, A.D., Hammond, A.L., Liang, Z., Collins, L.R., Meng, H., 2018. Effects of Reynolds number and Stokes number on particle-pair relative velocity in isotropic turbulence: a systematic experimental study. *Journal of Fluid Mechanics* 839, 271–292.

Dou, Z., Pecenak, Z.K., Cao, L., Woodward, S.H., Liang, Z., Meng, H., 2016. PIV measurement of high-Reynolds-number homogeneous and isotropic turbulence in an enclosed flow apparatus with fan agitation. *Measurement Science and Technology* 27, 1–17.

Efendiev, Y., 2004. Modeling and simulation of multi-component aerosol dynamics. *Computational and Applied Mathematics* 23, 401–423.

Elghobashi, S., 1994. On predicting particle-laden turbulent flows. *Applied Scientific Research* 52, 309–329.

Falola, A., Borissova, A., Wang, X.Z., 2013. Extended method of moment for general population balance models including size dependent growth rate , aggregation and breakage kernels. *Computers and Chemical Engineering* 56, 1–11.

Fan, J., Zhang, X., Chen, L., Cen, K., 1997. New stochastic particle dispersion modeling of a turbulent particle-laden round jet. *Chemical Engineering Journal* 66, 207–215.

Fang, J., Wang, Y., Kangasluoma, J., Attoui, M., Junninen, H., Kulmala, M., Petäjä, T., Biswas, P., 2018. The initial stages of multicomponent particle formation during the gas phase combustion synthesis of mixed SiO2/TiO2. *Aerosol Science and Technology* 52, 277–286.

Fede, P., Simonin, O., Villedieu, P., 2015. Monte-Carlo simulation of colliding particles or coalescing droplets transported by a turbulent flow in the framework of a joint fluid-particle pdf approach. *International Journal of Multiphase Flow* 74, 165–183.

Filbet, F., Laurençot, P., 2004. Numerical simulation of the Smoluchowski coagulation equation. *SIAM Journal on Scientific Computing* 25, 2004–2028.

Fino, D., Bensaid, S., Piumetti, M., Russo, N., 2016. A review on the catalytic combustion of soot in diesel particulate filters for automotive applications: From powder catalysts to structured reactors. *Applied Catalysis A: General* 509, 75–96.

Fitzgerald, J.W., Marti, J.J., Hoppel, W.A., Frick, G.M., Gelbard, F., 1998. A one-dimensional sectional model to simulate multicomponent aerosol dynamics in the marine boundary layer. 2. *Model application. J. Geophys. Res.* 103, 16103–16117.

Flagan, R.C., Seinfeld, J.H., 1988. Fundamentals of air pollution engineering. Prentice hall, Englewood Cliffs, New Jersey.

Fox, R.O., 2015. Computational Models for Turbulent Reacting Flows, Cambridge University Press 2003. Cambridge University press, Cambridge.

Frederix, E.M.A., Kuczaj, A.K., Nordlund, M., Veldman, A.E.P., Geurts, B.J., 2017. Application of the characteristics-based sectional method to spatially varying aerosol formation and transport. *Journal of Aerosol Science* 104, 123–140.

Friedlander, S.K., 2000. Smoke, dust and haze: fundamentals of aerosol. Oxford University Press, New York.

Fu, K., Liang, D., Wang, W., Cui, M., 2015. The time second-order characteristic FEM for nonlinear multicomponent aerosol dynamic equations in environment. *International Journal of Numerical Analysis and Modeling* 12, 211–229.

Ganesan, S., Tobiska, L., 2012. An operator-splitting finite element method for the efficient parallel solution of multidimensional population balance systems. *Chemical Engineering Science* 69, 59–68.

Gao, Z., Li, D., Buffo, A., Podgórska, W., Marchisio, D.L., 2016. Simulation of droplet breakage in turbulent liquid-liquid dispersions with CFD-PBM: Comparison of breakage kernels. *Chemical Engineering Science* 142, 277–288.

Garmory, A., Mastorakos, E., 2008. Aerosol nucleation and growth in a turbulent jet using the Stochastic Fields method. *Chemical Engineering Science* 63, 4078–4089.

Gelbard, F., 1990. Modeling multicomponent aerosol particle growth by vapor condensation. *Aerosol Science and Technology* 12, 399–412.

Gelbard, F., 1979. The General Dynamic Equation for Aerosols. California Institute of Technology.

Gelbard, F., Fitzgerald, J.W., Hoppel, W.A., 1998. A one-dimensional sectional model to simulate multicomponent aerosol dynamics in the marine boundary layer 3. Numerical methods and comparisons with exact solutions. *Journal of Geophysical Research-Atmospheres* 103, 16085–16102.

Gelbard, F., Seinfeld, J.H., 1980. Simulation of multicomponent aerosol dynamics. *Journal of Colloid and Interface Science* 78, 485–501.

Gelbard, F., Seinfeld, J.H., 1978. Coagulation and growth of a multicomponent aerosol. *Journal of Colloid And Interface Science* 63, 472–479.

Gelbard, F., Tambour, Y., Seinfeld, J.H., 1980. Sectional representations for simulating aerosol dynamics. *Journal of Colloid and Interface Science* 76, 541–556.

Ghahramani, E., Abouali, O., Emdad, H., 2014. Numerical analysis of stochastic dispersion of micro-particles in turbulent flows in a realistic model of human nasal/upper airway. *Journal of Aerosol Science* 67, 188–206.

Grant, S.B., Kim, J.H., Poor, C., 2001. Kinetic theories for the coagulation and sedimentation of particles. *Journal of Colloid and Interface Science* 238, 238–250.

Haibo, Z., Chuguang, Z., Minghou, X., 2005. Multi-Monte Carlo approach for general dynamic equation considering simultaneous particle coagulation and breakage. *Powder Technology* 154, 164–178.

Hao, X., Zhao, H., Xu, Z., Zheng, C., 2013. Population balance-Monte Carlo simulation for gas-to-particle synthesis of nanoparticles. *Aerosol Science and Technology* 47, 1125–1133.

He, Y., Zhao, H., 2016. Conservative particle weighting scheme for particle collision in gas-solid flows. *International Journal of Multiphase Flow* 83, 12–26.

He, Y., Zhao, H., Wang, H., Zheng, C., 2015. Differentially weighted direct simulation Monte Carlo method for particle collision in gas–solid flows. *Particuology* 21, 135–145.

Hess, A., Tarik, M., Foppiano, D., Edinger, P., Ludwig, C., 2016. Online Size and Element Analysis of Aerosol Particles Released from Thermal Treatment of Wood Samples Impregnated with Different Salts. *Energy and Fuels* 30, 4072–4084.

Hogan, R.C., Cuzzi, J.N., 2001. Stokes and Reynolds number dependence of preferential particle concentration in simulated three-dimensional turbulence. *Physics of Fluids* 13, 2938–2945.

Horwitz, J.A.K., Mani, A., 2016. Accurate calculation of Stokes drag for point-particle tracking in two-way coupled flows. *Journal of Computational Physics* 318, 85–109.

Housiadas, C., Drossinos, Y., 2005. "Aerosol Flows",*Mechanical Engineering Series*. CRC Press.

Hu, G., Celik, I., 2008. Eulerian-Lagrangian based large-eddy simulation of a partially aerated flat bubble column. *Chemical Engineering Science* 63, 253–271.

Hu, H.H., Patankar, N. a., Zhu, M.Y., 2001. Direct numerical simulations of fluid–solid systems using the arbitrary Lagrangian–Eulerian technique. *Journal of Computational Physics* 169, 427–462.

Huang, J.F., Chan, T.L., 2012. Vehicle queue effect on the characteristics of air flow, and exhaust scalar dispersion and distribution fields in the vehicle wake. *International Journal of Heat and Mass Transfer* 55, 7981–7990.

Huang, J.F., Chan, T.L., Zhou, Y., 2009. Three-dimensional flow structure measurements behind a queue of studied model vehicles. *International Journal of Heat and Fluid Flow* 30, 647–657.

Huang, L., Gong, S.L., Gordon, M., Liggio, J., Staebler, R., Stroud, C.A., Lu, G., Mihele, C., Brook, J.R., Jia, C.Q., 2014. Aerosol-computational fluid dynamics modeling of ultrafine and black carbon particle emission, dilution, and growth near roadways. *Atmospheric Chemistry and Physics* 14, 12631–12648.

Iliopoulos, I., Hanratty, T.J., 1999. Turbulent dispersion in a non-homogeneous field. *Journal of Fluid Mechanics* 392, 45–71.

Ireland, P.J., Bragg, A.D., Collins, L.R., 2016a. The effect of Reynolds number on inertial particle dynamics in isotropic turbulence. Part 1. Simulations without gravitational effects. *Journal of Fluid Mechanics* 796, 617–658.

Ireland, P.J., Bragg, A.D., Collins, L.R., 2016b. The effect of Reynolds number on inertial particle dynamics in isotropic turbulence. Part 2. Simulations with gravitational effects. *Journal of Fluid Mechanics* 796, 659–711.

Ireland, P.J., Desjardins, O., 2017. Improving particle drag predictions in Euler-Lagrange simulations with two-way coupling. *Journal of Computational Physics* 338, 405–430.

Jiang, J., Chen, D.-R., Biswas1, P., 2007. Synthesis of nanoparticles in a flame aerosol reactor with independent and strict control of their size , crystal phase and morphology. *Nanotechnology* 18, 1–8.

Kalani, A., Christofides, P.D., 2002. Simulation, estimation and control of size distribution in aerosol processes with simultaneous reaction, nucleation, condensation and coagulation. *Computers & Chemical Engineering* 26, 1153–1169.

Kardan, F., Baverel, O., Port, F., 2018. Assessment of RANS turbulence models in urban environments : CFD simulation of air fl ow around idealized high-rise morphologies, *Humanizing Digital Reality*. pp. 259–269.

Karlsen, K.H., Risebro, N.H., 1997. An operator splitting method for nonlinear convection-diffusion equations. *Numerische Mathematik* 77, 365–382.

Katoshevski, D., Seinfeld, J.H., 1997a. Analytical solution of the multicomponent aerosol general dynamic equation — without Coagulation. *Aerosol Science and Technology* 27, 541–549.

Katoshevski, D., Seinfeld, J.H., 1997b. Analytical–numerical solution of the multicomponent aerosol general dynamic equation—with coagulation. *Aerosol Science and Technology* 27, 550–556.

Katz, I.M., Davis, B.M., Martonen, T.B., 1999. A numerical study of particle motion within the human larynx and trachea. *Journal of Aerosol Science* 30, 173–183.

Kaur, G., Kumar, J., Heinrich, S., 2017. A weighted finite volume scheme for multivariate aggregation population balance equation. *Computers and Chemical Engineering* 101, 1–10.

Kazemi, S., Adib, M., Amani, E., 2018. Numerical study of advanced dispersion models in particle-laden swirling flows. *International Journal of Multiphase Flow* 101, 167–185.

Kim, Y.P., Seinfeld, J.H., 1992. Simulation of multicomponent aerosol dynamics. *Journal of Colloid and Interface Science* 149, 425–449.

Kim, Y.P., Seinfeld, J.H., 1990. Simulation of multicomponent aerosol condensation by the moving sectional method. *Journal of Colloid and Interface Science* 135, 185–199.

Klinkenberg, J., Sardina, G., Lange, H.C.D., Brandt, L., 2013. Numerical study of laminar-turbulent transition in particle-laden channel flow. *Physical review* E87, 1–11.

Kochenburger, T.M., Fernández, F.J., Prieto, M.M., 2017. Study and modification of a size-discrete semi-implicit simulation model for polydisperse aerosol coagulation. *Journal of Aerosol Science* 114, 180–194.

Kolb, C.E., Worsnop, D.R., 2012. Chemistry and composition of atmospheric aerosol particles. *Annual Review of Physical Chemistry* 63, 471–491.

Kommalapati, R.R., Valsaraj, K.T., 2009. Atmospheric aerosols and their importance. *ACS Symposium Series* 1005, 1–10.

Korhonen, H., Lehtinen, K.E.J., Kulmala, M., 2004. Multicomponent aerosol dynamics model UHMA: model development and validation. *Atmospheric Chemistry and Physics* 4, 757–771.

Kotalczyk, G., Kruis, F.E., 2018. Fractional Monte Carlo time steps for the simulation of coagulation for parallelized flowsheet simulations. *Chemical Engineering Research and Design*. In press.

Kruis, F.E., Wei, J., van der Zwaag, T., Haep, S., 2012. Computational fluid dynamics based stochastic aerosol modeling: Combination of a cell-based weighted random walk method and a constant-number Monte-Carlo method for aerosol dynamics. *Chemical Engineering Science* 70, 109–120.

Kuerten, J.G.M., 2006. Subgrid modeling in particle-laden channel flow. *Physics of Fluids* 18, 1–13.

Kumar, J., Peglow, M., Warnecke, G., Heinrich, S., Mörl, L., 2006. Improved accuracy and convergence of discretized population balance for aggregation : *The cell average technique* 61, 3327–3342.

Kumar, J., Warnecke, G., Peglow, M., Heinrich, S., 2009. Comparison of numerical methods for solving population balance equations incorporating aggregation and breakage. *Powder Technology* 189, 218–229.

Lai, A.C.K., Chen, J., 2015. Numerical study of cooking particle coagulation by using an Eulerian model. *Building and Environment* 89, 38–47.

Laskin, A., Laskin, J., Nizkorodov, S.A., 2015. Chemistry of atmospheric brown carbon. *Chemical Reviews* 115, 4335–4382.

Lau, T.C.W., Nathan, G.J., 2014. Influence of Stokes number on the velocity and concentration distributions in particle-laden jets. *Journal of Fluid Mechanics* 757, 432–457.

Lee, J., Lee, C., 2015. Modification of particle-laden near-wall turbulence: Effect of Stokes number. *Physics of Fluids* 27, 1–27.

Lee, K., Kim, T., Rajniak, P., Matsoukas, T., 2008. Compositional distributions in multicomponent aggregation. *Chemical Engineering Science* 63, 1293–1303.

Lehtinen, K.E.J., Zachariah, M.R., 2001. Self-preserving theory for the volume distribution of particles undergoing Brownian coagulation. *Journal of Colloid and Interface Science* 242, 314–318.

Li, D., Luo, K., Fan, J., 2018. Translational and rotational motions of small solid particles in a spatially developing turbulent boundary layer with heat transfer. *International Journal of Heat and Mass Transfer* 124, 715–725.

Li, D., Luo, K., Fan, J., 2017. Particle statistics in a two-way coupled turbulent boundary layer flow over a flat plate. *Powder Technology* 305, 250–259.

Li, Z., Wei, J., Yu, B., 2018. A pseudo point source model based on velocity coupled method for dilute particle-laden flow with dissipation scale particles. *International Journal of Multiphase Flow* 103, 106–123.

Liffman, K., 1992. A direct simulation Monte-Carlo method for cluster coagulation. *Journal of Computational Physics* 100, 116–127.

Lin, J., Pan, X., Yin, Z., Ku, X., 2016. Solution of general dynamic equation for nanoparticles in turbulent flow considering fluctuating coagulation. *Applied Mathematics and Mechanics (English Edition)* 37, 1275–1288.

Lin, J.Z., Yin, Z.Q., Lin, P.F., Yu, M.Z., Ku, X.K., 2015. Distribution and penetration efficiency of nanoparticles between 8-550 nm in pipe bends under laminar and turbulent flow conditions. *International Journal of Heat and Mass Transfer* 85, 61–70.

Lin, Y., Lee, K., Matsoukas, T., 2002. Solution of the population balance equation using constant-number Monte Carlo. *Chemical Engineering Science* 57, 2241–2252.

Liu, H.M., Chan, T.L., 2018a. Differentially weighted operator splitting Monte Carlo method for simulating complex aerosol dynamic processes. *Particuology* 36, 114–126.

Liu, H.M., Chan, T.L., 2018b. Two-component aerosol dynamic simulation using differentially weighted operator splitting Monte Carlo method. *Applied Mathematical Modelling* 62, 237–253.

Liu, H.M., Chan, T.L., 2016. A new differentially weighted operator splitting Monte Carlo method for aerosol dynamics., in: Proceedings of the 24th International Conference on Modelling, Monitoring and Management of Air Pollution (Air Pollution 2016), June 20-22, 2016, Crete, Greece. pp. 237–248.

Liu, S.Y., Chan, T.L., 2017a. A stochastically weighted operator splitting Monte Carlo (SWOSMC) method for the numerical simulation of complex aerosol dynamic processes. *International Journal of Numerical Methods for Heat and Fluid Flow* 27, 263–278.

Liu, S.Y., Chan, T.L., 2017b. A coupled CFD-Monte Carlo method for simulating complex aerosol dynamics in turbulent flows. *Aerosol Science and Technology* 51, 269–281.

Liu, X., Luo, K., Fan, J., 2016. Turbulence modulation in a particle-laden flow over a hemisphere-roughened wall. *International Journal of Multiphase Flow* 87, 250–262.

Liu, Y.H., He, Z., Chan, T.L., 2011. Three-dimensional simulation of exhaust particle dispersion and concentration fields in the near-wake region of the studied ground vehicle. *Aerosol Science and Technology* 45, 1019–1030.

Lu, J., 2005. Improving the representation of multicomponent aerosols in numerical models. Vanderbilt University.

Lucchesi, M., Abdelgadir, A., Attili, A., Bisetti, F., 2017. Simulation and analysis of the soot particle size distribution in a turbulent nonpremixed flame. *Combustion and Flame* 178, 35–45.

Luo, X.Y., Hinton, J.S., Liew, T.T., Tan, K.K., 2004. LES modelling of flow in a simple airway model. *Medical Engineering and Physics* 26, 403–413.

Lyu, X.P., Guo, H., Cheng, H.R., Wang, D.W., 2018. New particle formation and growth at a suburban site and a background site in Hong Kong. *Chemosphere* 193, 664–674.

MacInnes, J.M., Bracco, F. V., 1992. Stochastic particle dispersion modeling and the tracer-particle limit. *Physics of Fluids A* 4, 2809–2824.

Maisels, A., Einar Kruis, F., Fissan, H., 2004. Direct simulation Monte Carlo for simultaneous nucleation, coagulation, and surface growth in dispersed systems. *Chemical Engineering Science* 59, 2231–2239.

Mandø, M., Rosendahl, L., 2010. On the motion of non-spherical particles at high Reynolds number. *Powder Technology* 202, 1–13.

Marchisio, D.L., Fox, R.O., 2005. Solution of population balance equations using the direct quadrature method of moments. *Journal of Aerosol Science* 36, 43–73.

Marchisio, D.L., Vigil, R.D., Fox, R.O., 2003. Implementation of the quadrature method of moments in CFD codes for aggregation - breakage problems. *Chemical Engineering Science* 58, 3337–3351.

Matsoukas, T., Kim, T., Lee, K., 2009. Bicomponent aggregation with composition-dependent rates and the approach to well-mixed state. *Chemical Engineering Science* 64, 787–799.

Matsoukas, T., Lee, K., Kim, T., 2006. Mixing of components in two-component aggregation. *AIChE Journal* 52, 3088–3099.

McGraw, R., 1997. Description of aerosol dynamics by the quadrature method of moments. *Aerosol Science and Technology* 27, 255–265.

McLachlan, R., Quispel, G., 2002. Splitting methods. Acta Numerica 341–344.

Mendoza-Coto, A., Díaz-Méndez, R., Pupillo, G., 2016. Event-driven Monte Carlo: Exact dynamics at all time scales for discrete-variable models. *EPL (Europhysics Letters)* 114, 50003.

Menz, W.J., Akroyd, J., Kraft, M., 2014. Stochastic solution of population balance equations for reactor networks. *Journal of Computational Physics* 256, 615–629.

Metropolis, N., Ulam, S., 1949. The Monte Carlo Method. *Journal of the American Statistical Association* 44, 335–341.

Miller, S.E., Garrick, S.C., 2004. Nanoparticle coagulation in a planar jet. *Aerosol Science and Technology* 38, 79–89.

Mitrakos, D., Hinis, E., Housiadas, C., 2007. Sectional modeling of aerosol dynamics in multi-dimensional flows. *Aerosol Science and Technology* 41, 1076–1088.

Nah, T., Guo, H., Sullivan, A.P., Yunle, C., Tanner, D.J., Nenes, A., Russell, A., Ng, N.L., Huey, L.G., Weber, R.J., 2018. Characterization of aerosol composition, aerosol acidity and organic acid partitioning at an agriculture-intensive rural Southeastern U.S. site. *Atmospheric Chemistry and Physics Discussions*.In press.

Nere, N.K., Ramkrishna, D., 2006. Solution of population balance equation with pure aggregation in a fully developed turbulent pipe flow. *Chemical Engineering Science* 61, 96–103.

Njobuenwu, D.O., Fairweather, M., Yao, J., 2013. Coupled RANS-LPT modelling of dilute, particle-laden flow in a duct with a 90° bend. *International Journal of Multiphase Flow* 50, 71–88.

O'Rourke, P.J., 1981. Collective drop effects on vaporizing liquid sprays. Los Alamos National Lab., NM (USA) (No. LA-9069-T).

Olin, M., Rönkkö, T., Dal Maso, M., 2015. CFD modeling of a vehicle exhaust laboratory sampling system: Sulfur-driven nucleation and growth in diluting diesel exhaust. *Atmospheric Chemistry and Physics* 15, 5305–5323.

Ouchene, R., Khalij, M., Tanière, A., Arcen, B., 2015. Drag , lift and torque coefficients for ellipsoidal particles : From low to moderate particle Reynolds numbers. *Computers and Fluids* 113, 53–64.

Palaniswaamy, G., 2007. DSMC multicomponent aerosol dynamics: sampling algorithms and aerosol processes. University of Missouri-Columbia.

Palaniswaamy, G., Loyalka, S.K., 2008. Direct simulation, Monte Carlo, aerosol dynamics: Coagulation and condensation. *Annals of Nuclear Energy* 35, 485–494.

Passalacqua, A., Laurent, F., Madadi-Kandjani, E., Heylmun, J.C., Fox, R.O., 2018. An open-source quadrature-based population balance solver for OpenFOAM. *Chemical Engineering Science* 176, 306–318.

Patel, R.G., Desjardins, O., Kong, B., Capecelatro, J., Fox, R.O., 2017. Verification of Eulerian- Eulerian and Eulerian- Lagrangian simulations for turbulent fluid-particle flows. *AIChE Journal* 63, 5396–5412.

Patterson, R.I.A., Singh, J., Balthasar, M., Kraft, M., Norris, J.R., 2006. The linear process deferment algorithm: a new technique for solving population balance equations. *SIAM Journal on Scientific Computing* 28, 303–320.

Patterson, R.I.A., Wagner, W., Kraft, M., 2011. Stochastic weighted particle methods for population balance equations. *Journal of Computational Physics* 230, 7456–7472.

Pesmazoglou, I., Kempf, A.M., 2017. Large eddy simulation of particle aggregation in turbulent jets. *Journal of Aerosol Science* 111, 1–17.

Pesmazoglou, I., Kempf, A.M., Navarro-martinez, S., 2016. Stochastic modelling of particle aggregation. *International Journal of Multiphase Flow* 80, 118–130.

Pöschl, U., 2005. Atmospheric aerosols: Composition, transformation, climate and health effects. *Atmospheric Chemistry* 44, 7520–7540.

Prakash, A., Bapat, A.P., Zachariah, M.R., 2003. A simple numerical algorithm and software for solution of nucleation, surface growth, and coagulation problems. *Aerosol Science and Technology* 37, 892–898.

Pratsinis, S.E., Spicer, P.T., 1998. Competition between gas phase and surface oxidation of TiCl4 during synthesis of TiO2 particles. *Chemical Engineering Science* 53, 1861–1868.

Pyykönen, J., Jokiniemi, J., 2000. Computational fluid dynamics based sectional aerosol modelling schemes. *Journal of Aerosol Science* 31, 531–550.

Raes, F., Kodas Toivo, T., Friedlander Sheldon, K., 1990. Aerosol formation by a reversible chemical reaction: Laser-induced NH4NO3 aerosol formation in a tubular reactor. *Aerosol Science and Technology* 12, 856–868.

Ramabhadran, T.E., Peterson, T.W., Seinfeld, J.H., 1976. Dynamics of aerosol coagulation and condensation. *AIChE Journal* 22, 840–851.

Raman, V., Fox, R.O., 2016. Modeling of fine-particle formation in turbulent flames. *Annual Review of Fluid Mechanics* 48, 159–190.

Rigopoulos, S., 2007. PDF method for population balance in turbulent reactive flow. *Chemical Engineering Science* 62, 6865–6878.

Rjasanow, S., Wagner, W., 1996. A stochastic weighted particle method for the Boltzmann equation. *Journal of Computational Physics* 124, 243–253.

Rodrigues, P., Franzelli, B., Vicquelin, R., Gicquel, O., Darabiha, N., 2018. Coupling an LES approach and a soot sectional model for the study of sooting turbulent non-premixed flames. *Combustion and Flame* 190, 477–499.

Rossi, R., Iaccarino, G., 2009. Numerical simulation of scalar dispersion downstream of a square obstacle using gradient-transport type models. *Atmospheric Environment* 43, 2518–2531.

Rybalko, M., Loth, E., Lankford, D., 2012. A Lagrangian particle random walk model for hybrid RANS/LES turbulent flows. *Powder Technology* 221, 105–113.

Samuel, A., Premnath, K.N., Abraham, J., 2016. Lattice Boltzmann method simulations of Stokes number effects on particle trajectories in a wall-bounded flow. *Computers and Fluids* 124, 208–219.

Sandu, A., 2006. Piecewise polynomial solutions of aerosol dynamic equation. *Aerosol Science and Technology* 40, 261–273.

Schiller, U.D., 2014. A unified operator splitting approach for multi-scale fluid - particle coupling in the lattice Boltzmann method. *Computer Physics Communications* 185, 2586–2597.

Seigneur, C., Hudischewskyj, a. B., Seinfeld, J.H., Whitby, K.T., Whitby, E.R., Brock, J.R., Barnes, H.M., 1986. Simulation of aerosol dynamics: a comparative review of mathematical models. *Aerosol Science and Technology* 5, 205–222.

Seinfeld J.H., P.S.N., 1998. Atmospheric Chemistry and Physics. Wiley-Interscience, New York, NY.

Shigeta, M., Watanabe, T., 2010. Growth model of binary alloy nanopowders for thermal plasma synthesis. *Journal of Applied Physics* 108, 15.

Singh, M., Kaur, G., De Beer, T., Nopens, I., 2018. Solution of bivariate aggregation population balance equation: a comparative study. Reaction Kinetics, *Mechanisms and Catalysis* 123, 385–401.

Smagorinsky, J., 1963. General circulation experiments with the primitive equations. *Monthly Weather Review* 91, 99–164.

Smith, M., Matsoukas, T., 1998. Constant-number Monte Carlo simulation of population balances. *Chemical Engineering Science* 53, 1777–1786.

Sommerfeld, M., 2001. Validation of a stochastic Lagrangian modelling approach for inter-particle collisions in homogeneous isotropic turbulence. *International Journal of Multiphase Flow* 27, 1829–1858.

Strömgren, T., Brethouwer, G., Amberg, G., Johansson, A. V, 2012. Modelling of turbulent gas-particle flows with focus on two-way coupling effects on turbophoresis. *Powder Technology* 224, 36–45.

Sun, Z., Axelbaum, R., Huertas, J., 2004. Monte Carlo simulation of multicomponent aerosols undergoing simultaneous coagulation and condensation. *Aerosol Science and Technology* 38, 963–971.

Sun, Z., Axelbaum, R.L., Chao, B.H., 2002. A multicomponent sectional model applied to flame synthesis of nanoparticles. *Proceedings of the Combustion Institute* 29, 1063–1069.

Sunol, A.M., Charan, S.M., Seinfeld, J.H., 2018. Computational simulation of the dynamics of secondary organic aerosol formation in an environmental chamber. *Aerosol Science and Technology* 6826, 1–13.

Sweet, J., Richter, D.H., Thain, D., 2017. GPU acceleration of Eulerian-Lagrangian particle-laden turbulent flow simulations. *International Journal of Multiphase Flow* 99, 437–445.

Taghipour, F., Ellis, N., Wong, C., 2005. Experimental and computational study of gas-solid fluidized bed hydrodynamics. *Chemical Engineering Science* 60, 6857–6867.

Tsantilis, S., Kammler, H.K., Pratsinis, S.E., 2002. Population balance modeling of flame synthesis of titania nanoparticles. *Chemical Engineering Science* 57, 2139–2156.

Valsaraj, K.T., Kommalapati, R.R., 2009. Atmospheric aerosols: characterization, chemistry, modeling,and dlimate. American Chemical Society Symposium Series. Oxford University Press, USA.

Veroli, G., Rigopoulos, S., 2010. Modeling of Turbulent Precipitation : A Transported Population Balance-PDF Method *AIChE Journal* 56, 878-892.

Vié, A., Pouransari, H., Zamansky, R., Mani, A., 2016. Particle-laden flows forced by the disperse phase: Comparison between Lagrangian and Eulerian simulations. *International Journal of Multiphase Flow* 79, 144–158.

Vincont, J.Y., Simoens, S., Ayrault, M., Wallace, J.M., 2000. Passive scalar dispersion in a turbulent boundary layer from a line source at the wall and downstream of an obstacle. *Journal of Fluid Mechanics* 424, 127–167.

Vlieghe, M., Coufort-Saudejaud, C., Liné, A., Frances, C., 2016. QMOM-based population balance model involving a fractal dimension for the flocculation of latex particles. *Chemical Engineering Science* 155, 65–82.

Wang, L., Zheng, X., Stevanovic, S., Wu, X., Xiang, Z., Yu, M., Liu, J., 2018. Characterization particulate matter from several Chinese cooking dishes and implications in health effects. *Journal of Environmental Sciences* In press.

Wang, X., Zheng, X., Wang, P., 2017. Direct numerical simulation of particle-laden plane turbulent wall jet and the influence of Stokes number. *International Journal of Multiphase Flow* 92, 82–92.

Wei, J., 2016. A Monte Carlo simulation for particle aggregation containing a sol-gel phase transition. *Journal of Sol-Gel Science and Technology* 78, 270–278.

Wei, J., 2013. A fast monte carlo method based on an acceptance-rejection scheme for particle coagulation. *Aerosol and Air Quality Research* 13, 1273–1281.

Wei, J., Kruis, F.E., 2013. A GPU-based parallelized Monte-Carlo method for particle coagulation using an acceptance-rejection strategy. *Chemical Engineering Science* 104, 451–459.

Wexler, A.S., W Lurmann, F., H Seinfeld, J., 1994. Modelling urban and regional aerosols-I. model development. *Atmospheric Environment* 28, 531–546.

Winkler, C.M., Rani, S.L., Vanka, S.P., 2004. Preferential concentration of particles in a fully developed turbulent square duct flow. *International Journal of Multiphase Flow* 30, 27–50.

Xie, M., Yu, M., 2018. Thermodynamic analysis of Brownian coagulation based on moment method. *International Journal of Heat and Mass Transfer* 122, 922–928.

Xu, B.H., Yu, A.B., Chew, S.J., Zulli, P., 2000. Numerical simulation of the gas-solid flow in a bed with lateral gas blasting. *Powder Technology* 109, 13–26.

Xu, H., Khalid, M., Pollard, A., 2003. Large Eddy Simulation of Turbulent Flow in a Confined Square Coaxial Jet. *International Journal of Computational Fluid Dynamics* 17, 339–356.

Xu, Z., Zhao, H., Zheng, C., 2014. Fast Monte Carlo simulation for particle coagulation in population balance. *Journal of Aerosol Science* 74, 11–25.

Yamakov, V.I., 2016. Parallel grand canonical Monte Carlo (ParaGrandMC) simulation code.

Yang, T.S., Shy, S.S., 2005. Two-way interaction between solid particles and homogeneous air turbulence: Particle settling rate and turbulence modification measurements. *Journal of Fluid Mechanics* 526, 171–216.

Yu, M., Lin, J., 2017. Hybrid method of moments with interpolation closure-Taylor-series expansion method of moments scheme for solving the Smoluchowski coagulation equation. *Applied Mathematical Modelling* 52, 94–106.

Yu, M., Lin, J., Chan, T., 2008a. A new moment method for solving the coagulation equation for particles in Brownian motion. *Aerosol Science and Technology* 42, 705–713.

Yu, M., Lin, J., Chan, T., 2008b. Numerical simulation of nanoparticle synthesis in diffusion flame reactor. *Powder Technology* 181, 9–20.

Zhang, W., You, C., 2015. Numerical approach to predict particle breakage in dense flows by coupling multiphase particle-in-cell and Monte Carlo methods. *Powder Technology* 283, 128–136.

Zhang, Z., Chen, Q.Ã ., 2007. Comparison of the Eulerian and Lagrangian methods for predicting particle transport in enclosed spaces. *Atmospheric Environment* 41, 5236–5248.

Zhao, F., Yang, W., Yu, W., Li, H., Sim, Y.Y., Liu, T., Tay, K.L., 2018. Numerical study of soot particles from low temperature combustion of engine fueled with diesel fuel and unsaturation biodiesel fuels. *Applied Energy* 211, 187–193.

Zhao, H., Kruis, F.E., 2014. Dependence of steady-state compositional mixing degree on feeding conditions in two-component aggregation. *Industrial & Engineering Chemistry Research* 53, 6047–6055.

Zhao, H., Kruis, F.E., Zheng, C., 2011. Monte carlo simulation for aggregative mixing of nanoparticles in two-component systems. *Industrial and Engineering Chemistry Research* 50, 10652–10664.

Zhao, H., Kruis, F.E., Zheng, C., 2010. A differentially weighted Monte Carlo method for two-component coagulation. *Journal of Computational Physics* 229, 6931–6945.

Zhao, H., Kruis, F.E., Zheng, C., 2009. Reducing statistical noise and extending the size spectrum by applying weighted simulation particles in Monte Carlo simulation of coagulation. *Aerosol Science and Technology* 43, 781–793.

Zhao, H., Xu, Z., Zhao, H., 2016. Predictions on dynamic evolution of compositional mixing degree in two-component aggregation. *Journal of Aerosol Science* 101, 10–21.

Zhao, H., Zheng, C., 2013. A population balance-Monte Carlo method for particle coagulation in spatially inhomogeneous systems. *Computers & Fluids* 71, 196–207.

Zhao, H., Zheng, C., 2011. Two-component brownian coagulation: Monte carlo simulation and process characterization. *Particuology* 9, 414–423.

Zhao, H., Zheng, C., 2009. A new event-driven constant-volume method for solution of the time evolution of particle size distribution. *Journal of Computational Physics* 228, 1412–1428.

Zhao, H., Zheng, C., Xu, M., 2005a. Multi-Monte Carlo approach for general dynamic equation considering simultaneous particle coagulation and breakage. *Powder Technology* 154, 164–178.

Zhao, H., Zheng, C., Xu, M., 2005b. Multi-Monte Carlo method for coagulation and condensation/evaporation in dispersed systems. *Journal of Colloid and Interface Science* 286, 195–208.

Zhao, H., Zheng, C., Xu, M., 2005c. Multi-Monte Carlo method for particle coagulation: Description and validation. *Applied Mathematics and Computation* 167, 1383–1399.

Zhao, W., Jama, M.A., Buffo, A., Alopaeus, V., 2018. Population balance model and experimental validation for reactive dissolution of particle agglomerates. *Computers and Chemical Engineering* 108, 240–249.

Zhao, Y., Wang, Y., Yao, J., Fairweather, M., 2018. Reynolds number dependence of particle resuspension in turbulent duct flows. *Chemical Engineering Science* 187, 33–51.

Zheng, J., Wang, L., Hong, W., Xu, S., Baolong, S., 2018. Investigation of aggregation kernel and simulation of ultrafine particle aggregation under turbulence and Brownian motion. *Journal of Chemical Engineering of Japan* 51, 62–70.

Zhong, J., Nikolova, I., Cai, X., MacKenzie, A.R., Harrison, R.M., 2018. Modelling traffic-induced multicomponent ultrafine particles in urban street canyon compartments: Factors that inhibit mixing. *Environmental Pollution* 238, 186–195.

Zhou, H., Yang, Y., Wang, L., 2015. Numerical investigation of gas-particle flow in the primary air pipe of a low NOx swirl burner-The DEM-CFD method. *Particuology* 19, 133–140.

Zhou, K., Attili, A., Alshaarawi, A., Bisetti, F., 2014a. Simulation of aerosol nucleation and growth in a turbulent mixing layer. *Physics of Fluids* 26, 1–25.

Zhou, K., Chan, T.L., 2016. Aerosols-Science and Case Studies. Chapter 1: Operator splitting Monte Carlo method for aerosol dynamics.

Zhou, K., He, Z., Xiao, M., Zhang, Z., 2014b. Parallel Monte Carlo simulation of aerosol dynamics. *Advances in Mechanical Engineering* 6, 1–11.

Zhou, K., Jiang, X., Sun, K., He, Z., 2016. Eulerian-Lagranigan simulation of aerosol evolution in turbulent mixing layer. *Applied Mathematics and Mechanics (English Edition)* 37, 1305–1314.

Zhu, H.P., Zhou, Z.Y., Yang, R.Y., Yu, A.B., 2007. Discrete particle simulation of particulate systems: Theoretical developments. *Chemical Engineering Science* 62, 3378–3396.

Ziemann, P.J., Atkinson, R., 2012. Kinetics, products, and mechanisms of secondary organic aerosol formation. *Chemical Society Reviews* 41, 6582–605.

Zou, Y., Kavousanakis, M.E., Kevrekidis, I.G., Fox, R.O., 2010. Coarse-grained computation for particle coagulation and sintering processes by linking Quadrature Method of Moments with Monte-Carlo. *Journal of Computational Physics* 229, 5299–5314.

Zucca, A., Marchisio, D.L., Barresi, A.A., Fox, R.O., 2006. Implementation of the population balance equation in CFD codes for modelling soot formation in turbulent flames. *Chemical Engineering Science* 61, 87–95.